On the dynamics of ball bearings

J.A. Wensing

This research project was supported by and carried out at the SKF Engineering & Research Centre BV in Nieuwegein, the Netherlands. The support is gratefully acknowledged.

CIP-GEGEVENS KONINKLIJKE BIBLIOTHEEK, DEN HAAG

Wensing, Jeroen Anton

On the dynamics of ball bearings
PhD thesis, University of Twente, Enschede, The Netherlands
December 1998

ISBN: 90-36512298
Subject headings: ball bearings, dynamics, finite elements

Cover with permission of SKF
Printed by FEBO druk BV, Enschede, The Netherlands

ON THE DYNAMICS OF BALL BEARINGS

PROEFSCHRIFT

ter verkrijging van
de graad van doctor aan de Universiteit Twente,
op gezag van de rector magnificus,
prof.dr. F.A. van Vught,
volgens besluit van het College voor Promoties
in het openbaar te verdedigen
op donderdag 17 december 1998 te 16.45 uur.

door

Jeroen Anton Wensing

geboren op 19 september 1971
te Doetinchem

Dit proefschrift is goedgekeurd door de promotor

prof. dr. ir. H. Tijdeman

en de assistent-promotor

dr. ir. P.J.M. van der Hoogt

Summary

This investigation on the dynamic behaviour of ball bearings was motivated by the demand for silent bearings in noise-sensitive applications, especially in the household appliance and automotive industry. The present investigations are intended to provide a clear understanding of the role of the bearing in the application with respect to its design, its quality and the way in which it is mounted in the housings.

Ball bearings can be important generators of noise and vibrations in applications. Due to the rotation of the lubricated contacts, the stiffness in the bearing is time dependent and generates parametric excitations. Furthermore, vibrations are generated by geometrical imperfections on the individual bearing components. The imperfections are caused by irregularities during the manufacturing process, and although their amplitudes are on the nanometer scale, they can still produce significant vibrations in the application. An important type of imperfection for noise related problems is waviness. Waviness is to be understood as global sinusoidally shaped imperfections on the outer surface of components. In the present approach, the waviness is treated using a statistical approach.

In the approach followed the bearing is considered as an integral part of the application. The time dependent behaviour of the application was studied by means of predictive modelling. The shaft, the housings and the outer ring of the bearing were modelled using the finite element method. To solve the equations of motion of the application by means of time integration, the large finite element models were reduced by component mode synthesis. To account for the flexibility of the outer ring in combination with the rotation of the rolling element set, a new method was developed. By means of a verification study it was shown that this new method is fast and accurate. The stiffness and damping of the elastohydrodynamically lubricated contacts between the balls and the guiding rings were modelled as simplified

spring-damper models. Their constitutive behaviour was predicted beforehand with the help of transient contact calculations.

The three-dimensional ball bearing model developed here was validated successfully with measurements on a standard vibration test spindle. The predicted resonances of the bearing and the vibrations generated by parametric excitations and geometrical imperfections agreed well with the measured ones up to 10 kHz. It was found that in the audible range, most of the vibrations generated by the bearing can be attributed to waviness imperfections on the balls. The damping of the individual bearing resonances was investigated both numerically and experimentally for different lubricants. For both cases, the effect of the lubricant viscosity showed the same trend. To demonstrate its strength, the new numerical tool was applied to a rotor dynamics application consisting of a flexible shaft and two deep groove ball bearings mounted in plummer block housings. In particular, the effect of parametric excitation was examined.

Samenvatting

Dit onderzoek naar het dynamisch gedrag van kogellagers wordt gedragen door de vraag naar 'stille' lagers in toepassingen, die gevoelig zijn voor geluid, met name in de industrie voor huishoudelijke apparaten en in de auto-industrie. Het onderzoek, dat wordt beschreven in dit proefschrift, heeft tot doel een beter begrip te verkrijgen over de rol van het lager bij de productie van geluid. Hierbij wordt gekeken naar het lager als onderdeel van de toepassing, waarbij aandacht wordt besteed aan het lagerontwerp, de lagerkwaliteit en de manier waarop het lager is gemonteerd in het lagerhuis.

Kogellagers worden gezien als belangrijke veroorzakers van trillingen en geluid in bepaalde apparaten. Door de rotatie van de gesmeerde contacten is de stijfheid van het lager tijdsafhankelijk en genereert het een parametrische aanstoting. Daarnaast worden trillingen gegenereerd door geometrische oneffenheden van de verschillende componenten van het lager. Deze oneffenheden worden veroorzaakt door afwijkingen in het productieproces. Hoewel de grootte van deze oneffenheden meestal in de orde van nanometers is, kunnen ze toch aanzienlijke trillingen veroorzaken in de toepassing. Een belangrijk type oneffenheid voor geluidsproblemen is 'waviness'. Dit zijn globale, sinusvormige afwijkingen aan de buitenkant van een component. In de huidige aanpak wordt rekening gehouden met het statistisch karakter van waviness.

In de gevolgde aanpak wordt het tijdsafhankelijke gedrag van de desbetreffende toepassing bestudeerd met behulp van computermodellen. De as, de huizen en de buitenring van het lager worden gemodelleerd met de eindige-elementenmethode. Om de bewegingsvergelijkingen te kunnen oplossen door middel van tijdsintegratie, worden de grote eindige-elementenmodellen gereduceerd door middel van een techniek, genaamd 'component mode synthesis'. Bij deze techniek wordt de constructie onderverdeeld in componenten, die eerst afzonderlijk worden gemodelleerd met behulp van zogenaamde su-

perelementen. Om ook de buitenring van een kogellager met deze techniek te kunnen beschrijven, is een nieuwe methode ontwikkeld. Uit een validiteitsonderzoek blijkt dat deze methode goed werkt.
De stijfheid en demping in de elasto-hydrodynamisch gesmeerde contacten tussen de kogels en de geleidende ringen worden gemodelleerd door middel van vereenvoudigde veer-dempermodellen. Hun constitutieve gedrag wordt voorspeld met behulp van tijdsafhankelijke contactberekeningen.

Het driedimensionale kogellagermodel is met succes gevalideerd met behulp van metingen op een spindel, die wordt gebruikt voor testdoeleinden. De voorspelde resonanties van het lager, de parametrisch opgewekte trillingen en de trillingen veroorzaakt door geometrische oneffenheden, komen goed overeen met de gemeten waarden tot 10 kHz. Er is vastgesteld, dat voor frequenties in het hoorbare gebied de meeste trillingen worden veroorzaakt door waviness op de kogels. De demping van de verschillende resonanties is onderzocht voor verschillende smeermiddelen. Zowel numeriek als experimenteel is eenzelfde trend gevonden tussen de demping van de resonanties in het lager en de viscositeit van het smeermiddel. Om de kracht van het ontwikkelde numerieke gereedschap te demonstreren, is het toegepast op een rotordynamisch systeem, bestaande uit een as en twee kogellagers, die gemonteerd zijn in standaard lagerhuizen. Er is in deze toepassing met name gekeken naar het effect van parametrische aanstoting.

Contents

Chapter 1

Introduction

1.1 Background

Manufacturers of equipment in, for example, the household appliance and automotive industries are increasingly urged to reduce the noise produced by their products; this development is supported both by the market and by governmental regulations. Examples of noise-sensitive household appliances are washing machines and air-conditioners. An important source of vibrations in these appliances is the electric motor (see Figure 1.1). Electric motors are often equipped with small and medium sized deep groove ball bearings. Nowadays, the lifetime and load capacity of these bearings is fairly well controlled thanks to the availability of new materials and improved production processes. As a result of these developments, noise is increasingly becoming the decisive parameter that determines the bearing quality.

Ball bearings are required to overcome the speed difference between a rotating shaft and its surrounding structure. A common ball bearing consists of a number of rolling elements and two rings, the inner and the outer ring (see Figure 1.2). Both rings have grooves or raceways to guide the rolling elements. The rolling elements are separated from each other by a cage. To reduce the friction and wear in the rolling contacts, bearings are lubricated with oil. The part of the surrounding structure that is connected to the bearing is usually referred to as the housing. The bearings and the housings have to provide sufficient static support for the shaft.

In the application, the housings and the shaft can be important noise radiators. The radiated noise is largely determined by the dynamic behaviour

of the application in the audible range. Frequencies that can be observed by the human ear range approximately from 20 Hz to 20 kHz. The ear is most sensitive to frequencies between 1kHz and 4kHz. It is especially in this frequency range that ball bearings are able to generate vibrations due to inevitable form deviations of the components. These imperfections are the result of irregularities in the manufacturing process, and although their amplitude is on the nanometer scale, they still produce significant vibration levels in the application, due to the high stiffness of the contact. A reduction of form deviations is also important for the running accuracy in, for instance, machine tool spindles.

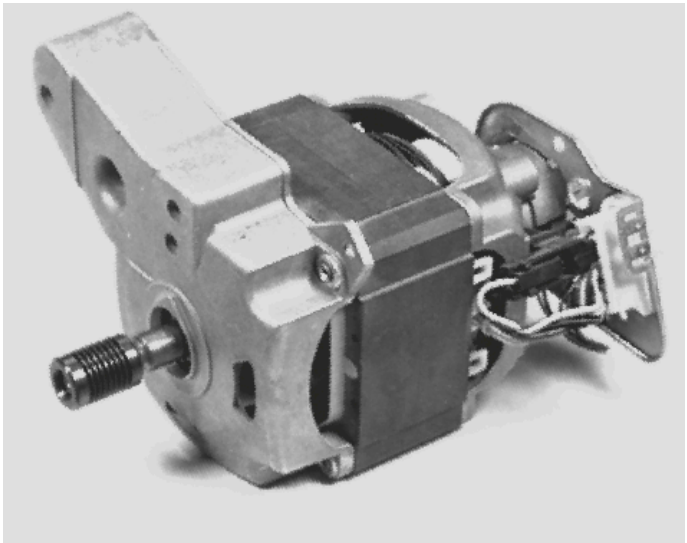

Figure 1.1: *Example of an electric motor for household appliances.*

Another important feature of the bearings, with respect to the dynamic behaviour of the application, is their inevitable presence in the transmission path of vibrations from the shaft to the housings. The transfer of vibrations through ball bearings largely depends on the stiffness and damping in the lubricated rolling contacts between the balls and the guiding rings. In general, the stiffness of these contacts depends on the load distribution and deformations in the whole application. This implies that the bearing has to be considered as an integral part of the application. Typical applications, in which the transmission characteristics of the bearings become important,

are gearboxes. In gearboxes, the contact between two gears forms the main source of vibrations.

The relative importance of the ball bearings with respect to the dynamic behaviour of the application has challenged bearing manufacturers to think of new and improved "silent" bearing designs by optimising the bearing in the specific application. Due to the increasing capacity of modern computers and the development of advanced numerical tools this is supported more and more by means of numerical simulations.

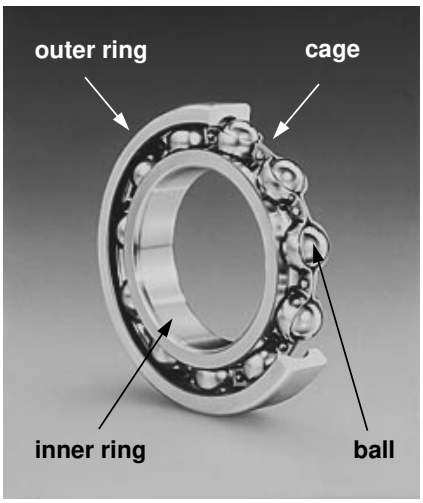

Figure 1.2: *Example of a deep groove ball bearing.*

A solely experimental approach is generally avoided because experiments are costly, time consuming and less universal than computer models. Moreover, in the case of ball bearings, an experimental approach often leads to a complex analysis because the individual vibration sources cannot be isolated and the measurement sensor is always positioned outside the bearing. An additional complicating aspect in ball bearings is the rotation of the different components. To illustrate this, an example of a vibration spectrum of a typical response measured on the outer ring of a ball bearing is shown in Figure 1.3.

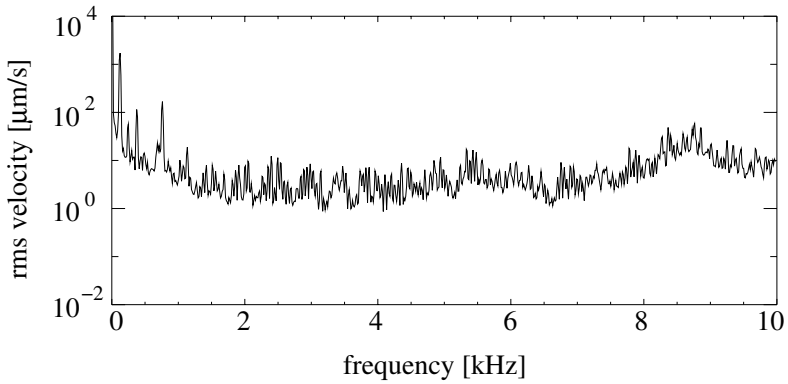

Figure 1.3: *Typical velocity spectrum of the measured response on the outer ring of a ball bearing.*

1.2 Aim of the investigations

The objective of this study is to provide the noise and vibration engineer with tools that enable him to efficiently predict the influence of ball bearings on the dynamic behaviour of the application. With the help of these tools the engineer can find answers to several design and manufacturing related questions such as:

- How is the perception of noise and vibrations at the periphery of the application caused by *vibrations generated inside* the bearing due to geometrical imperfections?
- What is the effect of the *bearing design* on the dynamic behaviour of the application?
- How does the *bearing mounting* affect the vibrational behaviour of the application?
- What is the value of the standard *vibration test* in relation to the vibrational behaviour in the application?

The answers to the above questions may help the engineer to improve the design of the application.

Generation of vibrations

The vibrations generated in ball bearings can be ascribed to different mechanisms. Most of these mechanisms are related to imperfections in the bearing, such as waviness, roughness, damage, fatigue spalls and dirt. However, at all times even perfect ball bearings generate vibrations due to the rotation of the *loaded* rolling elements. These vibrations can be attributed to the variable compliance in the bearing, which leads to *parametric excitations.*

Bearing design

The dynamic behaviour of the application can be influenced by the design of the bearings. The design can be altered by changing the geometrical and material properties of the bearing and the properties of the lubricant.

Important parameters for the internal design of the ball bearing are the number of rolling elements, the *osculation* and the radial *clearance*. The osculation is the ratio between the curvatures of the contacting bodies. With the osculation and the clearance, the stiffness in the contacts can be controlled.

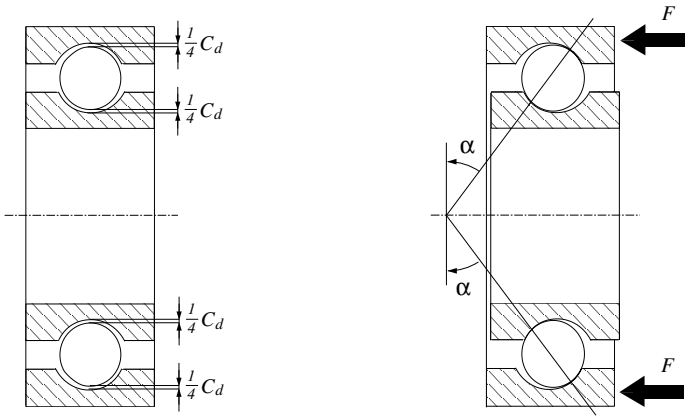

Figure 1.4: *Under an externally applied axial load, the radial clearance disappears and the bearing is loaded at contact angles* α.

The radial clearance C_d is defined as the free radial space in an unloaded bearing (see Figure 1.4). When the inner ring is fixed and the outer ring is axially loaded the internal clearance disappears. The optimum clearance is

dependent on the application. Under an axial load, a bearing with a large clearance has larger contact angles and is thus better suited to carry axial loads.
The lubricated contacts in the bearing are expected to be one of the major damping sources in the application. The damping is ascribed to viscous losses in the lubricant film. The quantification of contact damping is one of the main issues in the analysis of ball bearing applications.

Bearing mounting

The way in which the bearing is mounted has a considerable influence on the dynamic behaviour of the application. Usually, ball bearings are mounted with an externally applied axial load, to ensure a proper loading of the rolling elements. The applied load has a significant effect on the contact stiffnesses in the bearing. To be able to apply an axial load or to account for temperature expansions of the shaft, one of the bearing outer rings is usually mounted "loosely" in the bore of the housing.
The mounting of ball bearings is a meticulous job. Mounting errors are easily introduced. A frequently occurring mounting error is misalignment, where the central axes of the inner and outer rings of the bearing are not parallel. Even a misalignment angle of only a few minutes of arc can significantly increase the vibration level in the application.

Bearing vibration test

After a ball bearing is assembled, its quality is tested on a vibration test spindle. In general, one would like to see that bearings which perform well on the test spindle also perform well in the specific application of the customer. Unfortunately, this is not automatically true, since the vibrational behaviour of the bearing is largely determined by the application. With the numerical model presented in this thesis, both the vibration test and any customer application can be investigated so that the vibrational performance of the bearing on the test rig can be "translated" to the performance in the application without the need to conduct expensive experiments.

1.3 General approach and outline

The dynamic behaviour of a ball bearing application is studied by means of predictive modelling. An overview of theoretical models that have been

published in the literature is presented in Table 1.1. The table indicates which of the following features are included in the models:

A) The model is three-dimensional.

B) Geometrical imperfections are included.

C) The effect of lubrication is included.

D) The cage is modelled.

E) The flexibility of the application is accounted for.

F) The flexibility of the outer ring is accounted for.

G) The model is validated with experiments.

Literature reference	A	B	C	D	E	F	G
Sunnersjö , 1978	○	○	○	○	○	○	●
Gupta, 1979	●	○	●	●	○	○	○
Meyer, Ahlgren and Weichbrodt, 1980	○	●	○	○	○	●	○
Aini, Rahnejat and Gohar, 1990	●	○	○	○	○	○	●
Lim and Singh, 1990	●	○	○	○	●	○	●
Yhland, 1992	●	●	○	○	○	○	○
Su, Lin and Lee, 1993	○	●	○	○	○	●	●
Meeks and Tran, 1996	●	○	●	●	○	○	●
Hendrikx, van Nijen and Dietl, 1998	●	●	○	○	●	○	●
This thesis	●	●	●	○	●	●	●

Table 1.1: *Selection of literature related to the modelling of the dynamic behaviour of ball bearings.*

Table 1.1 is by no means complete but in the author's opinion it covers most of the important publications in this specific research area. Inspired by the increasing computer capacity the number of publications in the field has grown significantly over the last years. A lot of research has been conducted on three-dimensional modelling, the effect of geometrical imperfections and experimental validations. Much less effort has been devoted to the modelling of the cage, the modelling of lubrication effects and the application of ball bearings in flexible structures. The inclusion of a flexible outer ring has only been established in two-dimensional models. It is intended that the

present work contribute significantly to this particular research area.

The present study focuses especially on the generation of vibrations in the bearing and the transmission of these vibrations through the application. An important class of vibrations is generated by the form deviations of the contacting surfaces. Each individual bearing of course has unique surfaces. However, due to the fact that the bearings are produced by the same machining processes, it can be expected that all surfaces have certain features in common. These features can be described by so-called *surface topography parameters*. In the presented model, the form deviations of the rolling elements and the rings are described by Fourier series. The amplitudes of the harmonics are described by a small number of surface topography parameters with stochastic properties. The magnitude of the parameters is estimated from surface measurements **(Chapter 2)**.

The dynamics of the lubricated contacts between the rolling elements and the inner and outer rings are governed by the equations of motion of both the structural elements and the lubricant film. The nature of the problem requires the elastic deformations in the structural elements be accounted for. The calculation of the time dependent solution for a single contact in a ball bearing is very time consuming, even on modern computers. Hence, in the present approach the stiffness and damping of the lubricated contacts in the bearing are described by simplified spring-damper models. Their constitutive behaviour is described by curve-fit relations based on numerical solutions of time dependent contact calculations **(Chapter 3)**.

The shaft, the housings and the outer ring of the bearing are modelled using the finite element method. The large system matrices are reduced by writing the displacements of each component as a series of suitable shape functions. The adopted method is referred to as component mode synthesis. To account for the elasticity of the outer ring in combination with the rotation of the rolling element set, a new method has been developed **(Chapter 4)**.

The equations of motion of the application are derived with the help of Lagrange's equations. The equations of motion are solved by means of the Newmark time integration method **(Chapter 5)**.

The new ball bearing model is experimentally validated on a vibration test spindle. The predicted resonances and vibrations generated by the bearing are compared with measured ones for three different frequency bands.

Moreover, a method is presented to estimate the damping generated by the lubricated contacts in the bearing **(Chapter 6)**.

To demonstrate its capabilities, the numerical tool developed is applied in a radially loaded rotor dynamic application. The example focuses on parametric excitation. Two ways are presented to reduce the vibrations generated by parametric excitation **(Chapter 7)**.

In the final chapter of this thesis conclusions are presented **(Chapter 8)**.

Chapter 2

Vibration generation in ball bearings

2.1 Vibration sources

Even if the geometry of a ball bearing is perfect, it will still produce vibrations. The vibrations are caused by the rotation of a finite number of loaded rolling contacts between the balls and the guiding rings. Because these contacts are elastic, the bearing stiffness becomes explicitly dependent on time. In general, a time varying stiffness causes vibrations, even in the absence of external loads. Since the stiffness can be regarded as a system parameter, the variable stiffness leads to a so-called *parametric excitation*. It is one of the major sources of vibration in ball bearings. The first systematic research on this subject was conducted by Perret (1950) and Meldau (1951).

Due to the irregularities in the grinding and honing process, the contacting surfaces of the balls and the guiding rings always deviate from their perfect shape. A typical imperfection caused by these production processes is *waviness*. Waviness consists of global sinusoidally shaped imperfections on the outer surface of the components. Nowadays, the amplitudes of waviness in small deep groove ball bearings is of the order of nanometers. In spite of that, waviness still produces significant vibrations in the entire audible range. One of the first investigations in this field was made by Tallian and Gustafsson (1965). Besides waviness, other imperfections that are addressed in the present work are *ball diameter variations* and *cage run-out*.

2.2 Parametric excitation

The flexibility of the rolling contacts in a ball bearing can be represented by nonlinear springs (Hertz, 1881). When the mass of the rolling elements is neglected one spring can be used for both the inner and the outer contacts (see Figure 2.1).

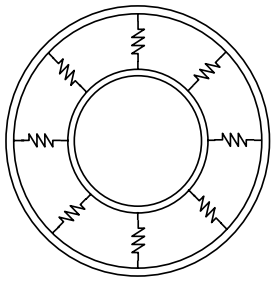

Figure 2.1: *The flexibility of the rolling contacts in a ball bearing is represented by nonlinear springs.*

Often, ball bearings are subjected to an externally applied axial load to preload the Hertzian contacts. In a two-dimensional model, the effect of an axial load can be modelled by introducing a negative radial clearance (see Figure 1.4). In the case of a negative clearance and a perfect geometry, the outer ring of a ball bearing with eight rolling elements is loaded with eight uniformly distributed contact loads. The resulting displacement field of the outer ring consists of both flexural and extensional deformations (see Figure 2.2). The analytical solution of this two-dimensional problem is given in Appendix A.

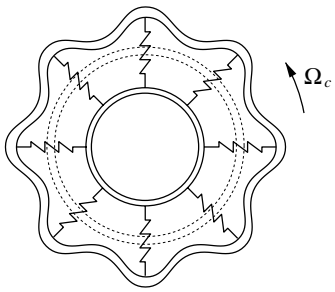

Figure 2.2: *Deformations of the outer ring due to eight uniformly distributed contact loads.*

When the rolling element set and the cage rotate with a constant angular velocity Ω_c, a parametrically excited vibration is generated that is transmitted through the outer ring. The characteristic frequency of this vibration equals $Z\Omega_c/2\pi$ and is called the *ball pass frequency*. This is the frequency at which the rolling elements pass an observation point fixed on the outer ring. The parameter Z denotes the total number of rolling elements in the bearing. In general, the generated vibration is not harmonic, but it does include harmonics of the ball pass frequency. In the case of an axially symmetric outer ring and ditto loading conditions, this vibration will not result in rigid body motion of the rings because the net forces in the vertical and horizontal direction equal zero.

The outer ring of the bearing is usually supported by a flexible housing. Most housings have asymmetric stiffness properties. This effect can be described by two linear springs with different stiffnesses in the horizontal and vertical directions (see Figure 2.3).

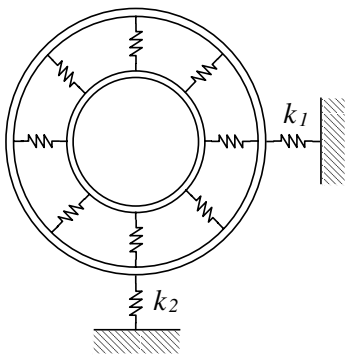

Figure 2.3: *The ball bearing is mounted in a housing with asymmetric stiffness properties.*

In the case of rotation, again, vibrations are generated at the ball pass frequency and its harmonics. The vibrations are mostly a combination of flexural vibrations of the outer ring and the housing and rigid body vibrations of the shaft. Since the contact behaviour is nonlinear, the effect of an asymmetric stiffness distribution in the application is enhanced by the introduction of a radial or misaligned external load. In the most extreme case the rolling elements lose contact with the raceway and the system becomes strongly nonlinear. The area, within which the rolling elements are still in contact with the raceway is generally referred to as the loaded zone (see Figure 2.4).

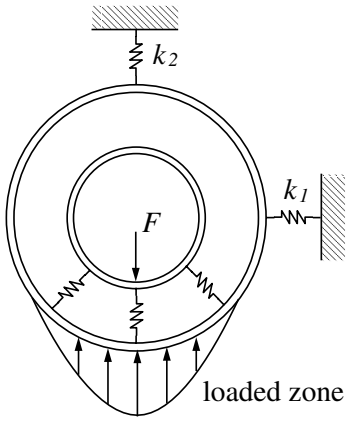

Figure 2.4: *In the presence of a radial load the rolling elements can lose contact with the raceway leading to severe parametric excitations.*

A phenomenon closely related to parametric excitations is parametric resonance. These are unstable or large amplitude solutions that are not directly related to the natural frequencies of the system (Nayfeh and Mook, 1979). In a nonlinear system, such as a ball bearing application, parametric resonance can change the system response dramatically. Under extreme loading conditions, it might even lead to chaos-like behaviour (Mevel and Guyader, 1993).

2.3 Geometrical imperfections

2.3.1 Description of waviness

An important source of vibration in ball bearings is waviness. These are global sinusoidally shaped imperfections on the outer surface of the bearing components (see Figure 2.5). The characteristic wavelengths of the imperfections are much larger than the dimensions of the Hertzian contact areas between the balls and the guiding rings. The number of waves per circumference is denoted by the wavenumber.

Waviness imperfections cause variations in the contact loads when the bearing is running. The magnitude of the variation depends on the amplitude of the imperfection and the stiffness in the contact. Due to the variations in the contact loads, vibrations are generated in the bearing. The resulting

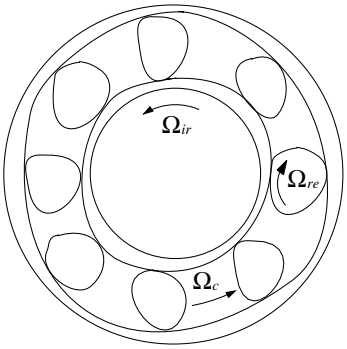

Figure 2.5: *Waviness excitation in a ball bearing.*

vibration modes of the rings can be either extensional, flexural or rigid body modes, dependent on the number of rolling elements and the wavenumber of the imperfection (see Figures 2.6 and 2.7). The extensional mode is usually accompanied by a rigid body mode in the axial direction. Imperfections with a different wavenumber cause vibrations at distinct frequencies, each with a characteristic vibration mode.

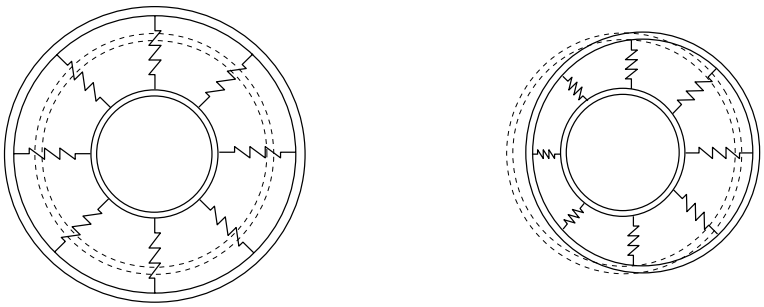

Figure 2.6: *Radial vibration modes of the inner and outer rings of a ball bearing caused by waviness: extensional mode (a) and rigid body mode (b).*

Surface measurements

A reliable prediction of the vibrations generated by ball bearings requires an accurate description of the waviness profiles up to approximately one

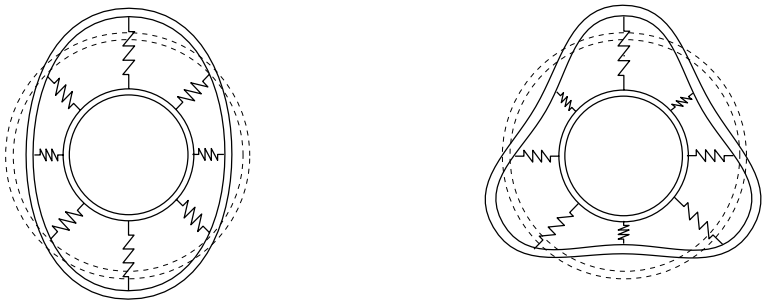

(c) *(d)*

Figure 2.7: *Radial vibration modes of the inner and outer rings of a ball bearing caused by waviness: oval mode (c) and triangle mode (d).*

thousand waves per circumference. One way to obtain the profiles is to measure the surfaces with a displacements sensor. An example of a measured waviness profile on a small deep groove ball bearing is depicted in Figure 2.8.

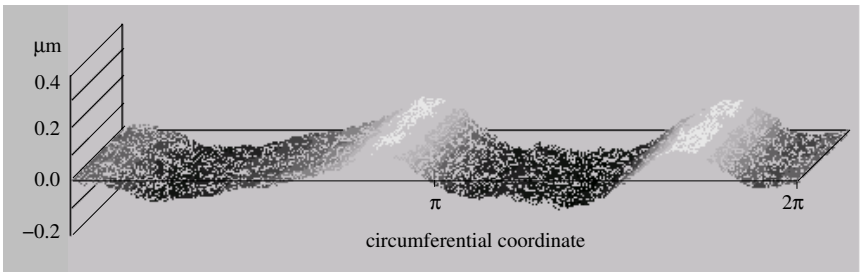

Figure 2.8: *Multi-track waviness measurement on the inner raceway of a small deep groove ball bearing.*

Each individual track of Figure 2.8 can be developed into a Fourier series. As an example, Figure 2.9 shows the power spectral density for a single track. In the measured data two regions can be identified, each with a characteristic behaviour. Usually, due to run-out of the measurement equipment, the first harmonic is omitted. The run-out equals the maximum radial displacement of the positioning spindle at the frequency of rotation. In the

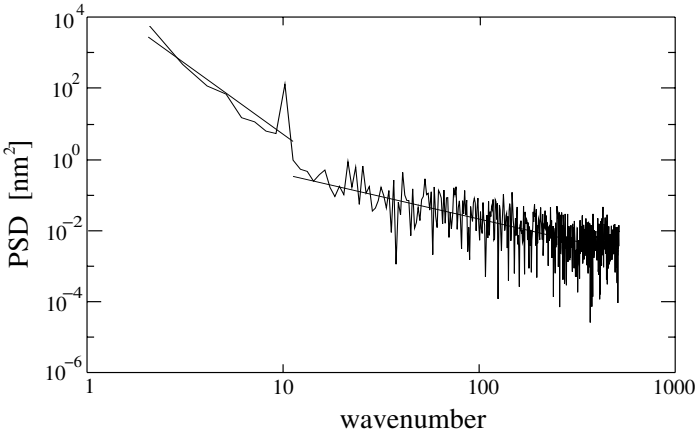

Figure 2.9: *Power spectral density (PSD) of a measured waviness profile on the inner ring of a small deep groove ball bearing.*

first region, for wavenumbers up to approximately ten waves per circumference, the amplitude decreases quadratically. With a double-logarithmic scaling of the power spectral density, this corresponds to a straight line with a slope of minus four. The gradients in Figure 2.9 are determined using the least-squares method. For wavenumbers higher than ten waves per circumference, the amplitude decreases linearly. In Figure 2.9, this corresponds to a straight line with a slope of minus two.

For low rotational speeds, the response of the bearing can be considered as being quasi-static. Measurements at SKF have shown that for wavenumbers below 10 waves per circumference, the measured waviness profiles correlate very well with low speed vibration measurements. For wavenumbers higher than 10 waves per circumference, the correlation becomes poor. The reason for the poor correlation is attributed to inaccuracies of the measurement equipment and uncontrolled effects caused by the lubricant film in the contacts. It is noted that for the wavenumbers mentioned, the thickness of the lubricant film is of the same order of magnitude as the height of the imperfections. Moreover, it is noted that the conditions in the contact between the measurement probe and the raceway are of course different from the conditions in the actual contact between a rolling element and the raceway.

Surface description

It is clear that in each individual ball bearing, the finished surfaces are different. But, because they are generally produced by the same machining processes, it can be expected that the surfaces have certain features in common. In the present approach these features are described by a small number of *surface topography parameters* that can easily be obtained from surface measurements. During the manufacturing of bearing components, statistical errors are introduced. For that reason some surface topography parameters have stochastic properties.

A single circumferential waviness track of the contacting surface is developed into a Fourier series. For a single track, the deviation W from the perfect geometry can be written as:

$$W(\theta) = \sum_{n=1}^{\infty} \frac{A}{n^s} \cos(n\theta + \varphi_n) \tag{2.1}$$

The parameter A equals the magnitude of the first harmonic. The exponent s describes the amplitude decay for subsequent wavenumbers. The phase φ_n is uniformly distributed over the interval $[0, 2\pi]$.

The magnitude A is subject to statistical variations. A likely probability distribution for the stochastic variable A is the Rayleigh distribution, since A is restricted only to positive values. In general, the Rayleigh distribution of a stochastic variable x is defined by the probability density function p and reads:

$$p(x, \alpha) = \left\{ \begin{array}{ll} 2\alpha x e^{-\alpha x^2} & x > 0, \quad \alpha > 0 \\ 0 & x < 0 \end{array} \right\} \tag{2.2}$$

Rayleigh distributions (see also Figure 2.10) can be derived from normal distributions. When the stochastic variables X and Y are normally distributed and R is defined by $R^2 = X^2 + Y^2$, then R has a Rayleigh distribution with $\sigma_x^2 = \sigma_y^2 = (2\alpha)^{-1}$. For $\alpha = 0.5$, equation 2.2 reduces to the standard Rayleigh distribution (Rothschild and Logothetis, 1986). For each wavenumber n, a new value for A is generated. The parameter α is determined from series of surface measurements.

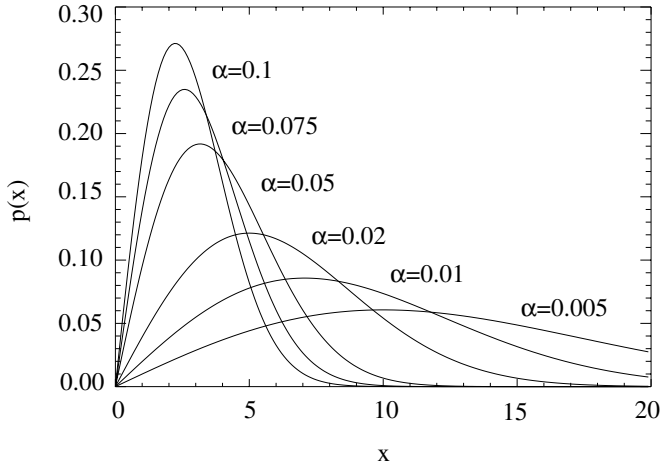

Figure 2.10: *Rayleigh distributions of the stochastic variable x for different values of α.*

2.3.2 Excitation frequencies

The rotational speeds of the inner ring, of the cage and of the rolling elements are different. As a result, inner ring, outer ring and ball waviness generate vibrations at distinct frequencies. The excitation frequencies are proportional to the rotational speed of the shaft. The ratio between the excitation frequency and the shaft frequency is generally referred to as the excitation order. Most order numbers of excitations generated by the bearing are rational numbers so that they can easily be detected in the vibration spectrum. A comprehensive overview of the vibrations generated in ball bearings was given by Wardle (1988) and Yhland (1992).

In the present work, Ω_{ir}, Ω_c and Ω_{re} denote the angular speeds of, respectively, the inner ring, the cage and the rolling elements (see also Figure 2.5). An integer $q \geq 0$ is introduced to indicate the harmonics of the ball pass frequency. The parameter Z refers to the total number of rolling elements. Finally, an integer $k \geq 0$ is introduced that is associated with the vibration mode of the inner and outer rings of the bearing:

- $k = 0$: extensional vibration and axial rigid body vibration, see Figure 2.6(a).

- $k = \pm 1$: rigid body vibrations moving forward $(+1)$, in the same direction as the rotating shaft, and backward (-1), see Figure 2.6(b).
- $k = \pm 2, 3...$: flexural vibrations with wavenumber k travelling forward $(+k)$ and backward $(-k)$, see Figures 2.7(c) and (d).

Inner ring waviness

For an observer at a fixed location on the outer ring or the housing, the vibrations generated by inner ring waviness are modulated at the ball pass frequency, resulting in combination harmonics. For wavenumbers

$$n = qZ \pm k, \tag{2.3}$$

the angular excitation frequencies are given by

$$\omega = qZ(\Omega_{ir} - \Omega_c) \pm k\Omega_{ir} \tag{2.4}$$

Outer ring waviness

Outer ring waviness is usually of the same order of magnitude as inner ring waviness. For an observer fixed on the outer ring or the housing, the vibrations generated by outer ring waviness are not modulated. As a consequence, the individual wavenumbers do not generate vibrations with unique frequencies, which makes the detection of outer ring waviness with vibration measurements much harder than the detection of inner ring waviness. With outer ring waviness, the effect of several wavenumbers can be observed at the ball pass frequency and its harmonics. For wavenumbers

$$n = qZ \pm k, \tag{2.5}$$

the angular excitation frequencies are given by

$$\omega = qZ\Omega_c \tag{2.6}$$

In terms of the response, outer ring waviness behaves quite similarly to parametric excitations. However, the underlying excitation mechanism is completely different.

Ball waviness

The waviness on the rolling elements is usually several times less than the waviness on the inner and outer ring. For low rotational speeds only imperfections with even wavenumbers generate vibrations. For uneven wavenumbers the resulting contact force in the inner contact is cancelled by the contact force in the outer contact because the contacts have a phase difference of π radians (see Figure 2.11). In case the centrifugal forces of the rolling elements become of the same order of magnitude as the contact forces, this is no longer true.

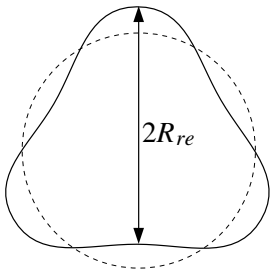

Figure 2.11: *For low rotational speeds, uneven ball waviness does not cause a disturbance in the EHL contacts.*

The vibrations generated by ball waviness are always the cumulative effect of all the rolling elements. The vibrations are modulated with the cage frequency. Hence, for each wavenumber of the rolling element, vibrations are generated at multiple frequencies. For wavenumbers n=2q, the angular excitation frequencies due to ball waviness read

$$\omega = 2q\Omega_{re} \pm k\Omega_c, \quad k \neq qZ \pm 1 \tag{2.7}$$

Ball diameter variations

Ball diameter variations can be regarded as a special case of ball waviness by taking q=0 in equation 2.7. Hence, the angular frequencies of the vibration generated by ball diameter variations are given by

$$\omega = k\Omega_c \quad k \neq qZ \pm 1 \tag{2.8}$$

Due to the different ball diameters, the ring is deformed into a complex shape that turns with the rotational speed of the cage. The shape is composed

of all flexural modes, with the exception of modes that have wavenumbers equal to qZ ± 1. For these wavenumbers the outer ring can restore the force balance by rigid body motion.

Cage run-out

Due to run-out of the cage, the rolling elements no longer stay equally spaced, as is illustrated in Figure 2.12. The resulting variations of the cir-

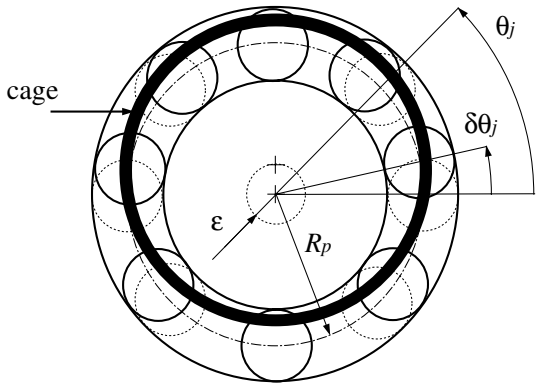

Figure 2.12: *Non-uniform ball spacing due to cage run-out.*

cumferential angles for a small run-out ε read

$$\delta\theta_j = \frac{\varepsilon}{R_p}\cos(\theta_j) \tag{2.9}$$

R_p denotes the pitch radius (see Figure 2.12). Due to the non-uniform spacing, the ball pass frequency is modulated with the cage frequency. The angular excitation frequencies due to the cage run-out are given by

$$\omega = qZ\Omega_c \pm k\Omega_c \tag{2.10}$$

Although the generated vibrations look very similar to the vibrations generated by ball diameter variations, there are some clear differences. With cage run-out, vibrations are also generated at $\Omega = qZ\Omega_c \pm \Omega_c$ and, although both mechanisms excite the bearing at coinciding frequencies, the resulting vibration modes are different.

2.4 Summary of excitation frequencies

For the convenience of the reader, the main excitation mechanisms in a ball bearing together with the corresponding angular frequencies are summarised in Table 2.1. Also, the corresponding vibration modes of the inner and outer rings are listed.

vibration source	wavenumber	ω (rad/s)
parametric excitation	$N.A.$	$qZ\Omega_c$
inner ring waviness	$n = qZ \pm k$	$qZ(\Omega_{ir} - \Omega_c) \pm k\Omega_{ir}$
outer ring waviness	$n = qZ \pm k$	$qZ\Omega_c$
ball waviness	$n = 2q$	$2q\Omega_{re} \pm k\Omega_c, \quad k \neq qZ \pm 1$
ball diameter variations	$N.A.$	$k\Omega_c, \quad k \neq qZ \pm 1$
cage run-out	$N.A.$	$qZ\Omega_c \pm k\Omega_c$

Table 2.1: *The excitation frequencies of different vibration sources in a ball bearing (N.A.: not applicable).*

The integer q refers to harmonics of the ball pass frequency, Z denotes the number of rolling elements and Ω_c, Ω_{ir} and Ω_{re} denote, respectively, the angular frequency of the cage, of the inner ring and of the rolling elements.

- $k = 0$: extensional vibration and axial rigid body vibration, see Figure 2.6(a).
- $k = \pm 1$: rigid body vibrations moving forward $(+1)$ and backward (-1), see Figure 2.6(b).
- $k = \pm 2, 3...$: flexural vibrations with wavenumber k travelling forward $(+k)$ and backward $(-k)$, see Figures 2.7(c) and (d).

Chapter 3

Stiffness and damping in EHL contacts

3.1 Modelling of the EHL contacts

Ball bearings are lubricated to reduce friction and wear in the rolling contacts between the raceway and the rolling elements. Due to the high pressure in the lubricated contacts, a strong interaction exists between the fluid film formation of the lubricant and the deformations of the contacting surfaces. This tribological phenomenon is called elastohydrodynamic lubrication, abbreviated as EHL. The transfer of vibrations through a ball bearing is largely affected by the stiffness and damping behaviour of EHL contacts. Also, the magnitude of vibrations generated by the geometrical imperfections is determined by the stiffness of the lubricated contacts. The stiffness of EHL contacts is provided both by the lubricant and by the resistance of the contacting surfaces to deformations. Damping is attributed mainly to viscous losses in the lubricant. Material damping due to hysteresis in the contacting surfaces is generally low.

The number of rolling elements in common deep groove ball bearings usually varies between 7 and 10. Consequently, the potential number of lubricated contacts varies between 14 and 20, hereby excluding the possible contacts between the rolling elements and the cage. Hence, for an efficient transient analysis, the number of DOF to model these contacts must remain small to save computing time. The lubricated contact between the raceway and each rolling element can be modelled by a single DOF model. It is assumed that the lubricated contact satisfies the so-called Hertzian assumptions:

- The material deformations are elastically.
- The loading is directed normal to the contacting surfaces, so that surface shear stresses can be neglected.
- The dimensions of the contact area are small compared to the radii of curvature of the contacting bodies.
- The deformations in the contact area are small compared to the dimensions of the contact area.

The mutual approach, denoted by δ, is defined as the change in distance between the centres of curvature of the contacting bodies. The radius of curvature of both bodies is denoted by R_1 and R_2. In the case of an unloaded contact $\delta = 0$, and the corresponding initial distance between the two centres of curvature is given by R_1+R_2. This situation is depicted on the left hand side in Figure 3.1. The right hand side shows the contact under load. The mutual approach δ accounts for elastic deformations in both bodies.

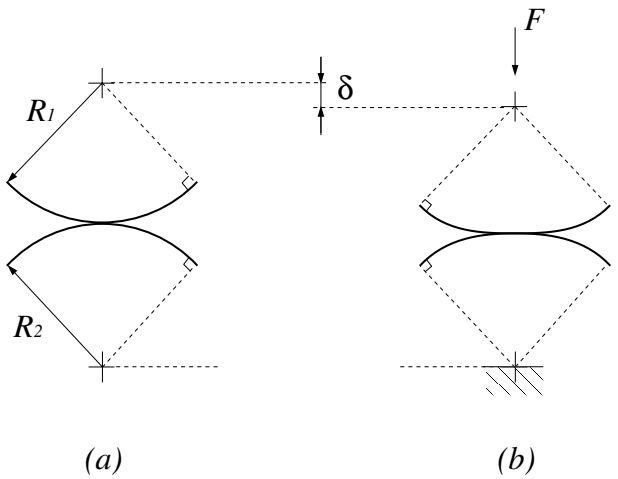

Figure 3.1: *Definition of the mutual approach δ by means of an unloaded contact (a) and a contact loaded with an external force F (b).*

The objective is to find a constitutive equation that describes the stiffness and damping in a lubricated contact or, in other words, a relation between the contact force F, the mutual approach δ and its time derivative $\dot{\delta}$. In general terms, the required relation can be written as:

$$F = f(\delta, \dot{\delta}) \tag{3.1}$$

In a specific application, relation 3.1 depends on the geometry and the velocities in the contact, the material properties of the elastic bodies and the properties of the lubricant. In the present investigation, the elastic restoring forces F_e are separated from the dissipative forces F_d so that:

$$F = F_e + F_d \tag{3.2}$$

The elastic restoring forces are assumed to be frequency independent. This means that F_e is independent of $\dot{\delta}$:

$$F_e = f(\delta) \tag{3.3}$$

For dry contact situations, a nonlinear expression can be obtained for $f(\delta)$ by using the solution of Hertz for an elliptic point contact. The Hertzian theory is summarised in Section 3.2. In EHL contact problems, it is often more convenient to derive the inverse of equation 3.3 i.e.:

$$\delta = g(F_e) \tag{3.4}$$

To solve F_e, an iterative process is required.

The lubricant is assumed to behave in a Newtonian way. Hence, a viscous damping model is adopted in which the dissipative forces are proportional to the time derivative of the mutual approach. The resulting equation yields:

$$F_d = c(\delta)\dot{\delta} \tag{3.5}$$

where $c(\delta)$ is also a function of the contact geometry, the material properties of the elastic bodies, the properties of the lubricant and the surface velocities in the contact.

To obtain a constitutive equation that describes the stiffness and damping in a lubricated contact, the steady state and time dependent behaviour of a single EHL contact must be studied (Wijnant, 1998). The determination of stiffness and damping in EHL contacts requires the solution of the equations of motion for both the lubricant film and the contacting structural elements. This solution can only be obtained numerically. Nowadays, with the help of advanced multi-grid techniques (Lubrecht, 1987; Venner, 1991), the time dependent solution can also be obtained within a reasonable time. To minimise the number of calculations and maintain the accuracy, all physical parameters are replaced by dimensionless ones.

The steady state numerical solutions of the EHL point contact are used to construct a relation for the dimensionless mutual approach in an EHL contact. The actual mutual approach in the EHL contacts is scaled on the equivalent Hertzian approach. The relation is derived by means of a curve-fit procedure. With the obtained relation an expression is derived for $g(F_e)$ in equation 3.4. The final expression can be represented by a nonlinear spring. From the analysis by Wijnant, it follows that a small increase is to be expected from the lubricant film on the stiffness in the contact, particularly for low loads and high speeds.

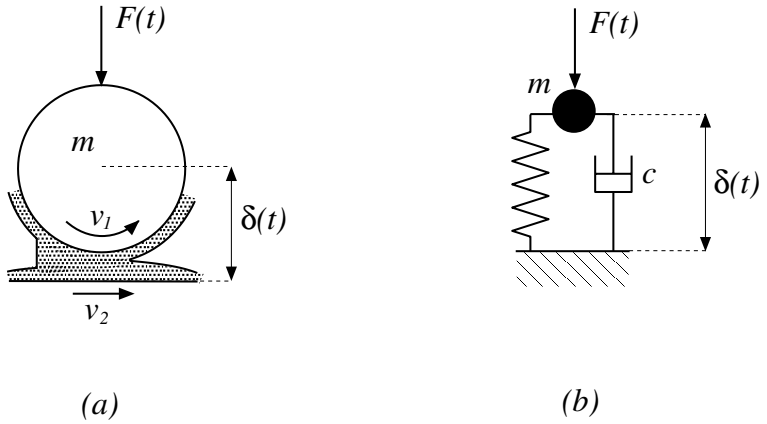

Figure 3.2: *The time dependent EHL contact problem (a) and an equivalent spring damper model (b).*

It is assumed that the damping generated in the EHL contact can be modelled by a linear viscous damper. To find an expression for the viscous damping coefficient c, a time dependent EHL calculation is performed to determine the response of a rolling element subjected to an impact excitation at t=0. The obtained numerical solution is fitted with the response of the single DOF system depicted in Figure 3.2. The steady state behaviour of this model is described with the previously obtained relation for the dimensionless mutual approach. Subsequently, the viscous damping coefficient c is determined by minimising the error between the response of the numerical simulation and the response of the single DOF system with the least square method. This procedure is repeated for different values of the dimensionless parameters. From the obtained dimensionless curve-fit relation an expression is found for the physical damping coefficient c in equation 3.5.

3.2 Hertzian theory

When the unloaded contact between two elastic bodies is limited to a single point, the contact is called a point contact. The geometry of a point contact is described by four radii of curvature (see Figure 3.3). By definition, convex surfaces have positive radii and concave surfaces have negative radii. The contacting surfaces sketched in Figure 3.3 both have convex surfaces.

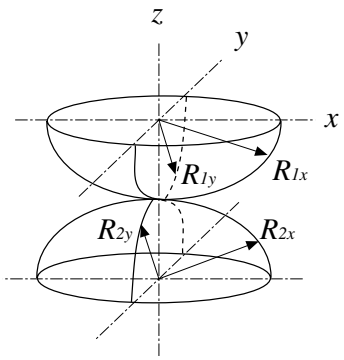

Figure 3.3: *The radii of curvature of the two contacting bodies.*

In a ball bearing the rolling elements make contact with the inner and outer raceway. In the remainder of this thesis these contacts are designated as inner and outer contacts. The surface of a rolling element is convex whereas the surface of the outer raceway is concave. The surface of the inner raceway is convex in the direction of motion and concave in the transverse direction. A number of important geometrical properties of a ball bearing are depicted in Figure 3.4.

When R_{re} denotes the ball radius, then the radii of curvature for the inner contacts read:

$$R_{1x} = R_{re} \tag{3.6}$$

$$R_{1y} = R_{re} \tag{3.7}$$

$$R_{2x} = \frac{R_p}{\cos(\alpha)} - R_{re} \tag{3.8}$$

$$R_{2y} = -R_i \tag{3.9}$$

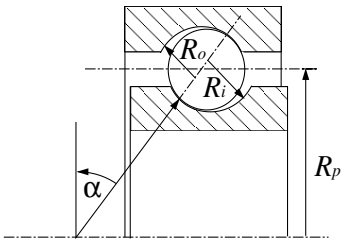

Figure 3.4: *A number of geometrical properties of a ball bearing.*

In the same way, the radii of curvature for the outer contacts read:

$$R_{1x} = R_{re} \tag{3.10}$$
$$R_{1y} = R_{re} \tag{3.11}$$
$$R_{2x} = -\left(\frac{R_p}{\cos(\alpha)} + R_{re}\right) \tag{3.12}$$
$$R_{2y} = -R_o \tag{3.13}$$

The radii of curvature of the raceway depend on the contact angle α. However, for the calculation of the reduced radii, only a small error is made by assuming a contact angle of zero degrees. The ratio between the ball radius and the radius of curvature of the raceway in the transverse direction is generally called the *osculation*. Hence, for the inner and outer osculations it follows:

$$f_i = \frac{R_i}{R_{re}} \qquad f_o = \frac{R_o}{R_{re}} \tag{3.14}$$

Usually, the contact problem in Figure 3.3 is reduced to the problem of a paraboloid shaped surface approaching a flat one. For the reduced radius of curvature R of the paraboloid, the following relation applies:

$$\frac{1}{R} = \frac{1}{R_x} + \frac{1}{R_y} \tag{3.15}$$

where:

$$\frac{1}{R_x} = \frac{1}{R_{1x}} + \frac{1}{R_{2x}} \qquad \frac{1}{R_y} = \frac{1}{R_{1y}} + \frac{1}{R_{2y}} \tag{3.16}$$

The ratio between both reduced radii of curvature is denoted by λ:

$$\lambda = \frac{R_x}{R_y} \tag{3.17}$$

For the reduced modulus of elasticity, the following relation is valid:

$$\frac{2}{E'} = \frac{1-\nu_1^2}{E_1} + \frac{1-\nu_2^2}{E_2} \tag{3.18}$$

where E_1, E_2, ν_1 and ν_2 are the moduli of elasticity and Poisson's ratios of the materials of both contacting bodies.

In the case of a dry point contact, $f(\delta)$ in equation 3.3 is obtained from the Hertzian solution. For $\delta > 0$, the solution is given by:

$$F_e = \kappa\delta^{3/2} \qquad \kappa = \frac{\pi\epsilon E'}{3\mathcal{K}}\sqrt{\frac{2\mathcal{E}R}{\mathcal{K}}} \tag{3.19}$$

where $\mathcal{K}$ and $\mathcal{E}$ denote the elliptic integrals of the first and second kind, which read:

$$\mathcal{K} = \int_0^{\frac{\pi}{2}} \left[1 - \left(1 - \frac{1}{\epsilon^2}\right)\sin^2\phi\right]^{-\frac{1}{2}} d\phi \tag{3.20}$$

$$\mathcal{E} = \int_0^{\frac{\pi}{2}} \left[1 - \left(1 - \frac{1}{\epsilon^2}\right)\sin^2\phi\right]^{\frac{1}{2}} d\phi \tag{3.21}$$

The ellipticity parameter ϵ is defined by:

$$\epsilon = \frac{b}{a} \qquad a = \left(\frac{6\mathcal{E}RF_e}{\pi\epsilon E'}\right)^{1/3} \qquad b = \left(\frac{6\epsilon^2\mathcal{E}RF_e}{\pi E'}\right)^{1/3} \tag{3.22}$$

where a is half the contact length in the direction of motion, and b half the contact width in the transverse direction. For the relation between the ellipticity ratio ϵ and the ratio of the reduced radii of curvature λ, defined in 3.17, it can be derived:

$$\lambda = \epsilon^2\left(\frac{\mathcal{K} - \mathcal{E}}{\mathcal{E} - \epsilon^2\mathcal{K}}\right) \tag{3.23}$$

For the calculation of the elliptic integrals and the ellipticity parameter, approximations are used (Reusner, 1977) to avoid numerical integration. In the case of circular contacts $\lambda = 1$, $\epsilon = 1$ and $\mathcal{K} = \mathcal{E} = \frac{\pi}{2}$.

As mentioned earlier, the relationship between the contact force and the mutual approach of the contacting bodies is nonlinear. Often the gradient of the Hertzian solution is also required as for instance in an iterative process. For the stiffness in a dry Hertzian contact it follows that:

$$\frac{\partial F_e}{\partial\delta} = \frac{3}{2}\kappa\sqrt{\delta} \tag{3.24}$$

with κ given in equation 3.19.

3.3 EHL theory

The time dependent, isothermal EHL contact problem is governed by three equations. At first, there is the Reynolds equation, which relates the fluid film pressures to the geometry of the deformed gap and the velocities of the contacting surfaces. Secondly, the film thickness equation, describing the deformation of the contacting surfaces due to the pressures in the film and, as a third, the dynamic force balance of the rolling element. The pressure distribution and the corresponding film thickness in a typical EHL point contact is shown in Figure 3.5.

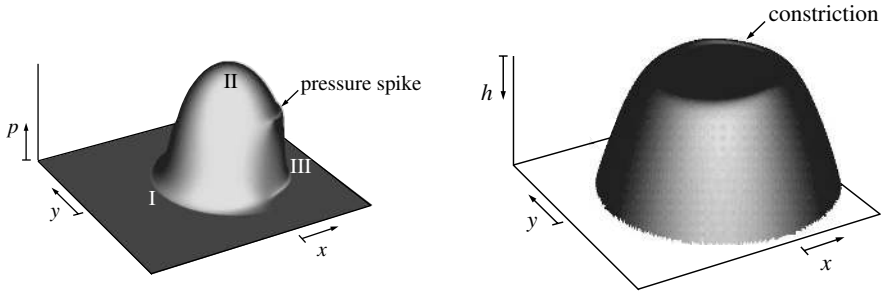

Figure 3.5: *The pressure and film thickness distribution in an EHL contact.*

Near the contact area three regions can be distinguished, the entrance region (I), the central region (II) and the exit region (III). In the entrance region, the lubricant is forced into the contact. Usually it is assumed in the models that there is enough oil in the entrance region to establish a full lubricant film. This condition is referred to as *fully flooded*. However, in reality the amount of oil in the contact is mostly insufficient to establish a full lubricant film and the contact is called *starved*. Starvation largely affects the behaviour of the lubricant film. In general, the film thickness decreases significantly in the central region of the contact.

Due to the high pressure in the central region of the contact the viscosity of the oil increases and the lubricant film almost solidifies. The resulting deformations of the contacting surfaces become of the same order of magnitude as the film thickness. For high loads, the pressure distribution in the central region is similar to the Hertzian pressure distribution. The pressure variation is hardly affected by the lubricant film. Hence in the central region of the contact the film thickness is almost constant, except for a constriction near the exit region. Here, the pressure distribution shows a characteristic

spike. Seen from above, the constriction has the shape of a horseshoe. In the exit region the lubricant film cavitates.

In high speed applications the pressure distribution and film thickness in the contact is significantly influenced by temperature effects as a result of frictional heating. To fully account for friction effects in the lubricated contacts, an additional equation would be required, i.e. the energy equation. However, in the present approach the effect of friction is accounted for by means of two approximate relations, one describing the temperature rise as a function of the sum speed and one describing the viscosity as a function of the temperature rise.

3.3.1 The Reynolds equation

The Reynolds equation prescribes the conservation of mass for the lubricant. It can be derived from the Navier-Stokes equations by assuming narrow gap conditions and a Newtonian fluid. Narrow gap conditions imply that the derivatives with respect to the $x-$ and $y-$ direction are much smaller than the derivatives with respect to the $z-$ direction. As a result of these narrow gap conditions, it follows automatically that the pressure is independent of z. For a point contact the Reynolds equation reads

$$\frac{\partial}{\partial x}\left(\frac{\rho h^3}{\eta}\frac{\partial p}{\partial x}\right)+\frac{\partial}{\partial y}\left(\frac{\rho h^3}{\eta}\frac{\partial p}{\partial y}\right)=6v_s\frac{\partial(\rho h)}{\partial x}+12\frac{\partial(\rho h)}{\partial t} \tag{3.25}$$

where: η = viscosity
p = hydrostatic pressure
ρ = density
h = gap width
v_s = sum speed

The surface velocities in the EHL contacts of a ball bearing are shown in Figure 3.6. If there is no slip, the sum speeds in the inner and outer contacts are equal and proportional to the angular shaft speed Ω. For the sum speed v_s we derive:

$$v_s = v_{or}+v_{re}=\Omega_c\left(R_p+R_{re}\cos(\alpha)\right)+\Omega_{re}R_{re} \tag{3.26}$$

where Ω_c denotes the angular speed of the rolling element set or cage, which is given by (Harris, 1993):

$$\Omega_c=\frac{\Omega}{2}\left(1-\frac{R_{re}\cos(\alpha)}{R_p}\right) \tag{3.27}$$

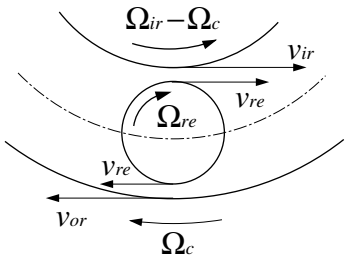

Figure 3.6: *The surface velocities and angular speeds in a ball bearing.*

and Ω_{re} the angular speed of the rolling element:

$$\Omega_{re} = \frac{\Omega R_p}{2R_{re}} \left(1 - \left(\frac{R_{re}\cos(\alpha)}{R_p} \right)^2 \right) \tag{3.28}$$

Note that the rolling elements rotate in a direction opposite to that of the inner ring and of the cage.

The two terms on the right hand side in equation 3.25 represent the two different pressure generation mechanisms in an EHL contact. The first term represents the wedge effect and the second one the squeeze film effect. At the edges of the domain, the pressure equals the ambient pressure level. Hence the pressure in the Reynolds equation has to be understood as the rise from ambient pressure level. In the outlet region of the contact, where the gap is widening, the Reynolds equation in general predicts negative pressures leading to cavitation. In the cavitation area, the pressure is assumed constant.

The viscosity of the lubricant increases exponentially with pressure. This effect is referred to as *piezo-viscosity* and can e.g. be described using the following relation (Barus, 1973):

$$\eta(p) = \eta_0 e^{\alpha_p p} \tag{3.29}$$

where η_0 denotes the dynamic viscosity at ambient pressure in Pas and α_p denotes the pressure-viscosity coefficient in Pa^{-1}. Due to the extremely high pressure in the central region of an EHL contact the viscosity increases enormously and the lubricant film becomes almost solid. This implies that

in the central region of an EHL contact the lubricant film becomes very stiff. Unfortunately, equation 3.29 is only accurate for relatively low pressures up to 0.1 GPa. In a general EHL contact, the pressure can become much higher. In that case the viscosity of the lubricant is overestimated by equation 3.29. However, this hardly influences the stiffness and damping behaviour in the contact. Even for a moderate pressure the lubricant film is already very stiff and, hence, the stiffness is completely dominated by the Hertzian stiffness of the structural elements. The damping is mainly determined by the behaviour of the lubricant in the low pressure zones in the entrance and in the exit region. Here, the flow velocities in the direction normal to the raceway are highest.

The density of the lubricant is also dependent on the pressure (Hamrock and Dowson, 1977). However, the effect of *compressibility* on the stiffness and damping in the contact is small because the density is only influenced at very high pressures. As mentioned before, at these high pressures the stiffness is mainly determined by the Hertzian stiffness of the structural elements, while the damping mainly depends on the lubricant behaviour in the low pressure zones in the entrance and in the exit region.

An important condition that influences the stiffness and damping of EHL contacts concerns the amount of oil available in the contact. Under so-called fully flooded conditions there is enough oil available in the contact to develop a full lubricant film. However, in standard greased bearings, fully flooded conditions hardly occur. In these bearings the amount of oil in the contact is limited and we have the situation of starved contacts. At SKF it has been found that starvation can decrease the damping in EHL contacts easily by a factor 2 or more. In the present investigation, all contact models are based on fully flooded conditions.

3.3.2 Film thickness equation

In the film thickness equation, the structural dynamics model and the EHL contact model are coupled. When the contact area dimensions are small compared to the reduced radii of curvature involved, then, locally, the *undeformed* surfaces may be approximated by paraboloids. Hence, the following relation applies for the film thickness or gap width h:

$$h(x,y,t) = -\delta(t) + \frac{x^2}{2R_x} + \frac{y^2}{2R_y} + d(x,y,t) \tag{3.30}$$

The different terms in equation 3.30 are illustrated in Figure 3.7. The circular arc is approximated by a Taylor series around $x = 0$ and is described by $z \approx x^2/2R_x$. The parameter δ denotes the mean mutual approach between

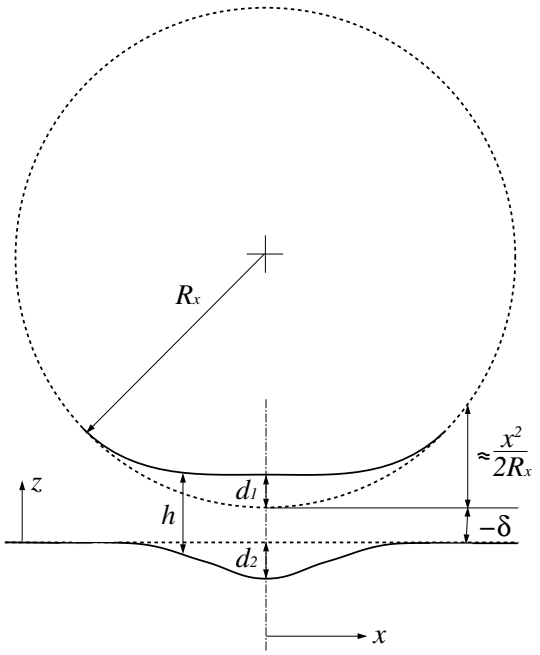

Figure 3.7: *Geometry of the gap in an EHL point contact for y=0.*

the contacting bodies, defined in Figure 3.1, and $d(x, y, t)$ denotes the time dependent elastic deformation of both structural elements:

$$d(x, y, t) = d_1(x, y, t) + d_2(x, y, t) \tag{3.31}$$

On the basis of the solution for a concentrated point load P acting on an elastic half-space, the deformation caused by a distributed load can be determined. The basic solution, which is presented in various publications (Timoshenko, 1993), was found by Boussinesq and reads:

$$w(x, y) = \frac{(1 - \nu^2)P}{\pi E} \frac{1}{\sqrt{x^2 + y^2}} \tag{3.32}$$

The total deformation $d(x, y, t)$=$d_1(x, y, t)$+$d_2(x, y, t)$, caused by a distributed load $p(x, y, t)$, follows after integration of equation 3.32 for both contacting

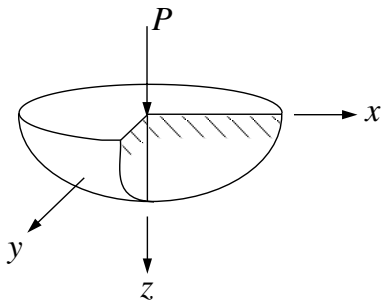

Figure 3.8: *Problem of a point load acting on an elastic half-space.*

bodies:

$$d(x,y,t) = \frac{2}{\pi E'} \int_{-\infty}^{\infty} \int_{-\infty}^{\infty} \frac{p(x',y',t)}{\sqrt{(x-x')^2 + (y-y')^2}} dx'dy' \tag{3.33}$$

3.3.3 The force balance equation

The dynamic behaviour of a rolling element is described by a single DOF system. The force balance results in the following equation:

$$m\ddot{\delta} + \int_{-\infty}^{\infty} p(x,y,t)dxdy = F(t) \tag{3.34}$$

where m denotes the rolling element mass and $F(t)$ a time dependent externally applied force.

3.3.4 Temperature effects

An important mechanism that must be considered for the investigation of stiffness and damping at high speeds is the effect of heat generation in the contact due to friction. The effect of heat generation in EHL contacts can be incorporated by extension of the steady state model with the energy equation. This has been investigated by Bos (1995) for fully flooded line contacts. From the investigation, it was concluded that for *pure rolling*, the temperature rise in the contact is well described by the following relation (Greenwood and Kauzlarich, 1973):

$$T - T_0 = \frac{3}{4} \frac{\eta_0 v_s^2}{k_f} \tag{3.35}$$

where k_f is the thermal conductivity of the lubricant in $\mathrm{Wm^{-1}K^{-1}}$. In equation 3.35, the temperature rise is independent of the load because it is assumed that all heat is generated in the low pressure entrance region.

Due to the temperature rise, the viscosity of the lubricant decreases considerably. The effect is often described by an exponential relation. In combination with the Barus equation (3.29) the following relation is obtained for the viscosity of the lubricant:

$$\eta(T) = \eta_0 e^{\alpha_p p - \gamma(T-T_0)} \tag{3.36}$$

where γ is the temperature viscosity coefficient of the lubricant, α_p the pressure-viscosity coefficient and η_0 the viscosity at room temperature and ambient pressure. Equation 3.36 is convenient for its simplicity but it is limited to small temperature variations.

In Figure 3.9, equations 3.35 and 3.36 are combined and for several lubricants and the viscosity η is plotted as a function of the sum speed v_s. The thermal conductivity $k_f = 0.14$ $\mathrm{Wm^{-1}K^{-1}}$ and the temperature-viscosity coefficient $\gamma = 0.028$ $\mathrm{K^{-1}}$ are chosen equal for all lubricants. It can be observed that the viscosity at ambient pressure drops considerably for high sum speeds. It

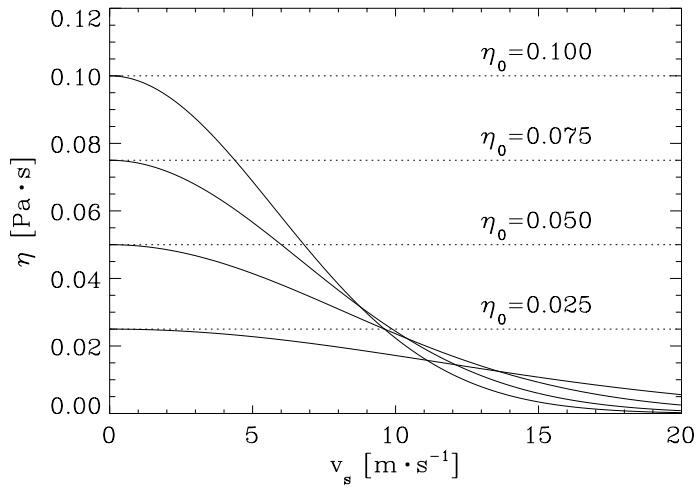

Figure 3.9: *Effect of friction on the viscosity for different values of the nominal viscosity* η_0.

can also be concluded that a higher nominal viscosity does not automatically lead to a higher viscosity under rotating conditions because one must be aware that for the same rotational speed the temperature in each lubricant is different.

3.4 Determination of EHL stiffness

The stiffness in an EHL contact can be determined from the constitutive equation that relates the contact force F_e to the mutual approach δ. The value of δ follows from the film thickness equation. The film thickness can be approximated by a formula based on a curve-fit of numerical solutions. In the present investigation, a curve-fit relation is used, as introduced by Wijnant (1998). The relation is derived from steady state numerical solutions for the fully flooded EHL point contact.

Rewriting the film thickness equation 3.33 for $x = 0$ and $y = 0$ yields the following expression for the mutual approach:

$$\delta = w_0 - h_0 \tag{3.37}$$

where w_0 and h_0 denote the elastic deformation and the film thickness at $x = 0$ and $y = 0$. The mutual approach δ and the film thickness h_0 are scaled with the Hertzian deformation resulting in the dimensionless quantities Δ and H_0, respectively. With equation 3.19, we obtain:

$$\Delta = \delta \left(\frac{\kappa_h}{F_e} \right)^{2/3} \qquad H_0 = h_0 \left(\frac{\kappa_h}{F_e} \right)^{2/3} \tag{3.38}$$

When the surface deformation w_0 is approximated by the Hertzian deformation, the dimensionless film thickness can be approximated by:

$$\Delta = 1 - H_0 \tag{3.39}$$

It was shown (Moes, 1992), that the EHL point contact problem for a circular contact area and an incompressible lubricant is governed by two dimensionless parameters M and L:

$$M = \frac{F_e}{E' R_x^2} \left(\frac{E' R_x}{\eta_0 v_s} \right)^{\frac{3}{4}} \qquad L = \alpha_p E' \left(\frac{\eta_0 v_s}{E' R_x} \right)^{\frac{1}{4}} \tag{3.40}$$

The quantity M is usually referred to as the dimensionless load because it is proportional to F_e. For the quantity L the direct physical interpretation

is less clear. In the case of elliptic contacts, the parameter λ is introduced to account for the different radii of curvature of the contacting bodies in the direction of motion x and transverse to the direction of motion y. The effect of the ellipticity is approximated (Wijnant, 1998) with the introduction of a new dimensionless parameter N, defined by:

$$N = \lambda^{\frac{1}{2}} M \qquad \lambda = \frac{R_x}{R_y} \tag{3.41}$$

The definition of N is based on the rigid isoviscous asymptotic solution of the EHL point contact. However, Wijnant has experienced that for the estimation of stiffness and damping this approach also gives satisfying results in general EHL contacts. An advantage of introducing N is that the contact needs to be solved only for one value of λ. For the dimensionless film thickness, it follows that:

$$\Delta(N, L) \approx 1 - H_0(N, L) \tag{3.42}$$

For different values of N and L, numerical solutions are generated for the mutual approach Δ. As a next step, the computed values are approximated by the following curve-fit formula:

$$\Delta(N, L) = 1 - p(L) N^{q(L)} \tag{3.43}$$

where

$$p(L) = \left((4 - 0.2L)^7 + (3.5 + 0.1L)^7\right)^{\frac{1}{7}} \tag{3.44}$$

$$q(L) = \left(-(0.6 + 0.6(L + 3)^{-\frac{1}{2}}\right)^{\frac{1}{7}} \tag{3.45}$$

The relation between Δ and the force F_e is implicit. Once the dimensionless mutual approach Δ is determined, for given values of the speed the reduced radii of curvature, the reduced elasticity modulus, the viscosity and the pressure-viscosity coefficient, the contact force F_e can be solved by means of an iterative process. Because in general the relation between Δ and F_e is smooth, F_e can be solved with a Newton-Raphson process.

In Figure 3.10, Δ is plotted for a range of values of N and L. For $\Delta = 1$ the mutual approach equals the Hertzian deformation. For high values of N, Δ approaches unity or, in other words, for these values the stiffness in the EHL contact resembles the Hertzian stiffness of the structural elements. In this region the fluid film is extremely stiff due to the relation between viscosity

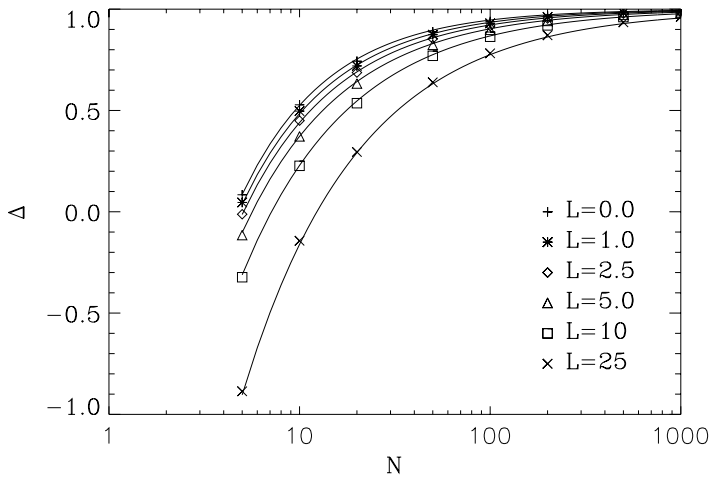

Figure 3.10: *Results of the numerical simulations and the curve-fit relations for the dimensionless mutual approach Δ, (source: Wijnant, 1998).*

and pressure (see equation 3.29). For lower values of N and higher values of L, Δ decreases and the effect of the fluid film becomes more important. For negative values of Δ, the stiffness in the contact is fully governed by the lubricant film. The situation resembles rigid isoviscous conditions. It can be observed that the dimensionless load only asymptotically approaches zero for infinite negative values of Δ. Due to the assumption of fully flooded conditions the film thickness can become infinitely large. Hence, in contrast to the Hertzian model, the EHL model does not predict loss of contact.

In noise-sensitive applications with grease lubricated deep groove ball bearings, N usually varies between 5 and 100 and L between 5 and 15. This implies that the lubricant film can have a noticeable effect on the stiffness in the contact, especially in high speed applications. Due to the presence of a lubricant film the clearance in the bearing decreases and the contacts are pre-loaded by the film leading to a higher contact stiffness. As a result the excitation forces caused by geometrical imperfections increase. A further implication of the EHL stiffness model is that the resonance frequencies of the ball bearing become dependent on the rotational speed. This effect, which is absent when only the Hertzian stiffness is accounted for, is confirmed by experiments (Dietl, 1997).

3.5 Determination of EHL damping

In the EHL contacts of rolling bearings energy is dissipated via viscous losses in the lubricant. Energy dissipation caused by hysteresis in the contacts can be neglected. Due to the piezo-viscous effect in the high pressure region, the fluid film is extremely stiff and the variation in film thickness remains small. As a result hardly any energy is dissipated in the central region of the contact in spite of the large viscosity. Instead, most of the energy is dissipated in the entrance region. Although the viscosity is already rising in this region, the piezo-viscous effect is still sufficiently small to provide enough flexibility of the lubricant to allow reasonable film thickness variations. A small amount of energy is dissipated also near the constriction in the exit region of the contact.

It is assumed that energy dissipation in the lubricant can be modelled with a viscous damper. The required viscous damping coefficient c has been determined with the help of numerical solutions of the time dependent EHL contact problem (Wijnant, 1998). Wijnant considered the damping under isothermal and fully flooded conditions and derived an empirical relation for the dimensionless viscous damping C, which is related to the physical damping parameter c (in Ns/m) by:

$$C = c\frac{av_s}{4F_eR}\frac{\mathcal{K}}{\mathcal{E}} \tag{3.46}$$

where a denotes half the Hertzian contact length in the direction of rolling, v_s the sum speed, R the reduced radius of curvature (see equation 3.15) and F_e the elastic restoring part of the contact force. The parameters $\mathcal{K}$ and $\mathcal{E}$ are the elliptic integrals of the first and second kind (see equations 3.20 and 3.21). Besides the dimensionless parameters N and L, the time dependent EHL problem is also governed by a third parameter, i.e. the dimensionless frequency, denoted by Λ. The dimensionless frequency is defined as the product of the system natural frequency and the time required for a particle to pass through half of the contact. The speed of a particle passing through the contact equals half the sum speed v_s. Hence, for the dimensionless frequency Λ, it follows:

$$\Lambda = \frac{a\omega_n}{\pi v_s} \tag{3.47}$$

where the quantity ω_n denotes the natural frequency of the system in radians per second. For the present study, results were available for Λ=1.0 and

different values of N and L. The relation, obtained after curve-fitting, reads:

$$C(N, L) = r(L)N^{s(L)} \tag{3.48}$$

where:

$$r(L) = 0.98 - 0.017L \tag{3.49}$$
$$s(L) = -0.83 - 0.008L \tag{3.50}$$

In Figure 3.11, the dimensionless damping C is plotted for a wide range of N and L. It is observed that the dimensionless damping $C(N, L)$ decreases significantly with both N and L.

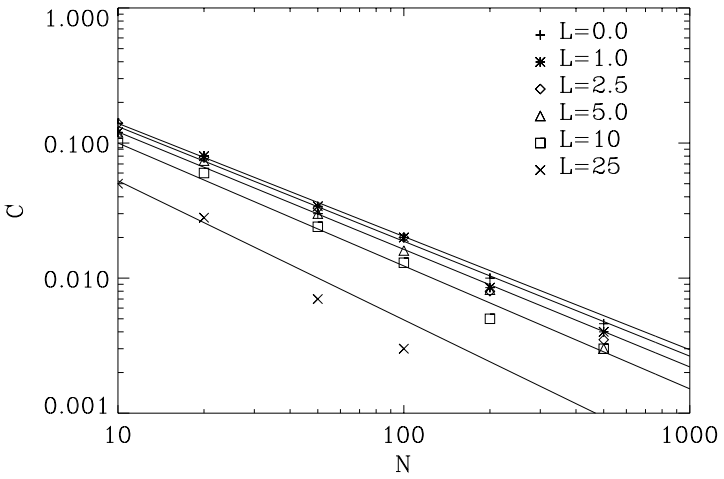

Figure 3.11: *Numerical results of C(N,L) and the empirical relation of equation* 3.48 *for* Λ=1.0 *and different values of N and L, (source: Wijnant, 1998).*

To give an idea of the physical damping values in a 6202 deep groove ball bearing, the damping coefficient c (in Ns/m) is plotted in Figure 3.12 as a function of the viscosity η_0. The damping is calculated for both the inner and the outer contact. For Ω=1800 rpm (revolutions per minute), the sum speed in both contacts equals $v_s = 2.25$ m/s. For that, a contact angle of 13 degrees was assumed. The considered contacts are pre-loaded with 50 N.

A list of the geometrical and the material properties of the bearing and the properties of the lubricant is presented in Appendix C.

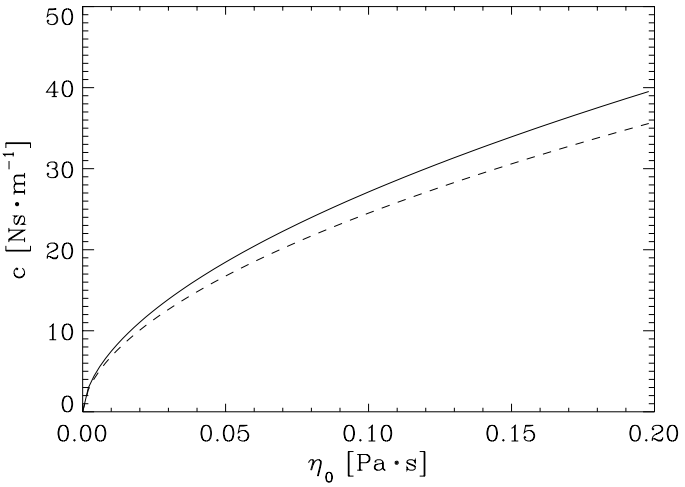

Figure 3.12: *EHL damping as a function of the viscosity for the inner (dashed line) and outer (solid line) contact of a DGBB* 6202.

It can be seen in Figure 3.12 that in an EHL contact the increase in damping is not quite proportional to the viscosity. From relation 3.48, it can be shown that the damping in the model increases to the power of 0.55. This result corresponds well with the value of 0.53 found in experiments by Dietl (1997). Furthermore, it is observed that the damping in both the inner and outer contacts of a DGBB 6202 are of the same order of magnitude.

3.6 Implementation of the EHL contact model

The EHL contact model, presented in this chapter, is used in the remainder of this thesis to model the lubricated contacts in a ball bearing between the rolling elements and the guiding rings (see Figure 3.13). In each contact, the stiffness is described by a nonlinear spring and the damping by a linear viscous damper.

The EHL stiffness model, as described by equation 3.43, is directly implemented in the new bearing model, including the iterative process for the

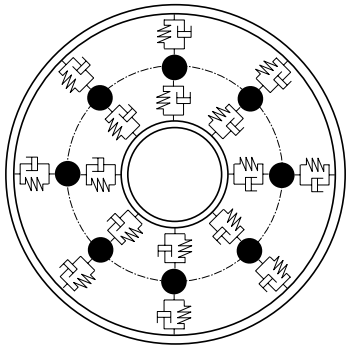

Figure 3.13: *The lubricated contacts in a ball bearing are modelled with the EHL contact model, presented in this chapter.*

determination of the resulting contact forces. The differences between the new EHL stiffness model and the Hertzian stiffness model for dry contact are relatively small. Characteristic for the new model is the asymptotic behaviour for negative mutual approaches. This behaviour is inherent to the assumption of fully flooded conditions.

The EHL damping model, as described by equation 3.48 is used as a preprocess tool to determine the damping coefficients of the linear viscous dampers in the contact. Although important aspects like starvation and the effect of the frequency are not yet included in the model, it can be regarded as a first and important step to understand the damping behaviour in EHL contacts.

Chapter 4

Modelling of housings and shafts

4.1 Introduction

A bearing application is considered consisting of a shaft and two deep groove ball bearings mounted in housings. The bearings and the housings must give sufficient static support to the shaft in order to provide positioning accuracy. As a result, they are relatively stiff. Nowadays, there is a tendency to manufacture bearing housings out of aluminium because of lower production costs. The bearing housings and the shaft are considered as potential noise radiators in the application. The prediction of noise radiated from a bearing application requires an accurate modelling of the dynamic behaviour of the housings and the shaft and an accurate knowledge of the excitation of these components by the bearings.

In most of the bearing models found in the literature, the inner and outer rings are assumed to be rigid. By neglecting the flexibility of the outer ring, the transfer of vibrations caused by the rotating rolling elements and the geometrically imperfect bearing components to the surrounding structure is not described sufficiently accurate. For this reason, in the present study the bearing outer ring is treated as a flexible body. Taking into account the flexibility of the outer ring is complicated, because the outer ring is subjected to a number of rotating loads. The loads are caused by the contacts between the raceway and the rolling elements. A model to predict the contact forces, which also accounts for the lubricant, has been presented in Chapter 3.

For the modelling of the dynamic behaviour of a general bearing application, the engineer must generally resort to numerical techniques. A well known numerical technique in structural dynamics is the so-called finite element method (FEM). In this method the considered structure is divided into a finite number of elements defined by corresponding nodes. For each element, simple shape functions are assumed. By prescribing a continuous displacement field for the structure, a number of equations is obtained which is proportional to the number of nodes. In a real application, it usually takes thousands of nodes with associated equations to obtain solutions of a reasonable accuracy. Especially for the simulation of the time dependent behaviour of complex structures, this may result in unacceptably long computation times.

For noise radiation problems, however, one is usually only interested in structural vibrations that may cause audible noise. In that case, the frequency band of interest ranges from 0 Hz to 20 kHz. The human ear is most sensitive to frequencies between 1 kHz and 4 kHz. After 10 kHz the sensitivity decreases strongly. To limit calculation times in the present study, the frequency band considered ranges from 0 Hz to 10 kHz. By limiting the problem to this specific frequency band, the model can be reduced considerably.

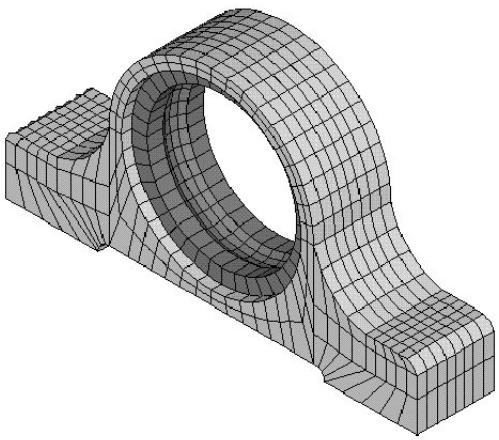

Figure 4.1: *FEM model of an aluminium bearing housing containing an outer ring of a deep groove ball bearing.*

A well known method to reduce the size of dynamic problems is the Ritz method. In this method, the displacements of the structure are described as a series of global shape functions. Often a structure consists of several substructures or components. When the structure is divided into several components and each individual component is described by the Ritz method, then the method is referred to as *component mode synthesis* (CMS). In a simple bearing application, usually two types of linear elastic components can be distinguished: the bearing housings and the shaft. Both component types can be modelled using a CMS technique.

Over the years, the development of CMS methods has resulted in several standard methods. The shaft is modelled according to one of the existing methods. For the bearing housings and the outer rings, a new CMS technique has been developed, which accounts also for the effect of rotating contact loads. Some extra provisions are required when the bearing housing or the outer ring have the possibility to move as a rigid body. The performance of the newly developed CMS method is evaluated by comparing natural frequencies and normal mode shapes of the reduced model with those of the original finite element model. Two examples are discussed, one of the outer ring of a 6202 deep groove ball bearing that can move as a rigid body and one of the same outer ring integrated in an aluminium housing.

4.2 Model reduction

In the Ritz method, the displacement field of the structure is approximated by a linear combination of admissible shape functions. By choosing suitable shape functions in the frequency range of interest, the size of the problem can be reduced significantly.

Let us consider a component that is modelled using the finite element method. The equations of motion for the component are given by

$$[M]\{\ddot{x}\} + [C]\{\dot{x}\} + [K]\{x\} = \{F\} \tag{4.1}$$

where $[M]$ is the mass matrix, $[C]$ the damping matrix and $[K]$ the stiffness matrix. The vector $\{F\}$ contains the externally applied forces. Each node of the finite element model has three degrees of freedom (DOF) i.e. the displacement in each coordinate direction. The total number of equations equals the number of finite element DOF. Following the Ritz method, the displacement field of a component is written as a linear combination of

suitable shape functions Ψ:

$$\{x\} = [\Psi]\{p\} \tag{4.2}$$

The vector $\{p\}$ contains the generalised DOF representing the contribution of the different shape functions. The shape functions are stored column-wise in the matrix $[\Psi]$. The number of generalised DOF is usually much less than the number of finite element DOF. By substitution of equation 4.2 into 4.1 and after pre-multiplication with $[\Psi]^T$, a new reduced set of equations of motion is obtained:

$$[m]\{\ddot{p}\} + [c]\{\dot{p}\} + [k]\{p\} = \{f\} \tag{4.3}$$

where the following relations apply for the reduced mass matrix $[m]$, the reduced damping matrix $[c]$ and the reduced stiffness matrix $[k]$:

$$[m] = [\Psi]^T[M][\Psi] \quad [c] = [\Psi]^T[C][\Psi] \quad [k] = [\Psi]^T[K][\Psi] \tag{4.4}$$

The reduced vector with externally applied forces obeys:

$$\{f\} = [\Psi]^T\{F\} \tag{4.5}$$

Once the solution is obtained for the reduced system, the displacements of the original finite element system can be obtained by back-substitution in equation 4.2.

When the assumed shape functions consist of the undamped natural mode shapes in the frequency range of interest and when the model is proportionally damped, the problem becomes decoupled. In that case the mass matrix $[m]$, the stiffness matrix $[k]$ and the damping matrix $[c]$ become diagonal. This method is known as modal decomposition. Generally, with the Ritz method, the system can be reduced from several thousands of finite element DOF to dozens of generalised DOF or mode shapes. Obviously, the number of required generalised DOF depends on the number of natural frequencies that exist in the considered frequency range.

For the sake of completeness, Guyan's reduction must also be mentioned, which is based on simple Gauss elimination. It is assumed that, within a certain frequency band, certain degrees of freedom, the so-called master DOF, are more important than the others, the so-called slave DOF. When the inertia of the slave DOF is neglected in the equations for the slave DOF, the slave DOF can be written as a linear combination of the master DOF and

a significant reduction is obtained. The method (see also Craig, 1981) was originally developed to solve the eigenvalue problem for large finite element models. It is also widely used in the field of experimental modal analysis to construct Test Analysis Models (TAM). However, for most structures Guyan's reduction method very seldom leads to an efficient and accurate reduction that is suited for a time dependent analysis. Hence, it was not considered as a potential reduction method either for the shaft or the bearing housings.

4.3 Component mode synthesis

4.3.1 Introduction to CMS

For a more efficient design process, mechanical structures are often subdivided into substructures or components. The components are usually connected to each other with well defined interfaces e.g. a rigid coupling or, in case of a bearing, a coupling with the EHL springs presented in Chapter 3. In CMS, the reaction forces at the interfaces are usually referred to as interface loads, here denoted by $\{F_b\}$. The DOF at the interfaces are classified as interface DOF and denoted by $\{x_b\}$. The remaining internal DOF are denoted by $\{x_i\}$. When a mechanical structure has to be modelled, a component-wise approach can be very advantageous since:

- it is easier to establish criteria for the dynamic performance of individual components supplied by subcontractors.
- for reasons of efficiency, design modifications can best be evaluated at a component level.
- the modelling and analysis at the component level can be left to subcontractors.
- identical components only need to be modelled once.
- the testing of a complete structure can be very expensive and sometimes even impossible, so that testing at the component level is the only remaining option.
- the dynamical properties of components, which are difficult to model, can possibly be identified by experiments.

- large systems exhibiting nonlinear behaviour can be analysed more efficiently when decomposed into components that behave in a nonlinear way, and components that behave in a linear way, because the latter can be reduced significantly.

The challenge of CMS methods is to find a minimum set of shape functions or component modes that accurately describe the dynamic behaviour of the assembled system in the frequency range of interest. Because of the component-wise approach, an optimum set of component modes should fulfil two important conditions:

- The capability to describe the static solution, in order to account for the effect of interface loads caused by the adjacent components.
- The generalised DOF of the reduced model must explicitly contain the interface DOF in order to couple adjacent component models.

Component modes are intended to describe the dynamic behaviour of a component in the assembled system. Consequently, they must also account for reaction forces at the interface with connecting components and for externally applied forces. Since the deformations caused by these forces are usually of a local character, they are not well described by the lowest natural mode shapes of the component. Additional component modes, which are referred to as the *static mode set*, are required to account for this effect. In other words, with this extra mode set one must be able to describe the local deformations of a component at its interface DOF. When applicable, the static mode set also has to account for rigid body motions.

To enable an easy coupling between the different components after the reduction, the vector with generalised DOF of each component must explicitly contain the interface DOF. In that way a time consuming transformation to the original finite element DOF can be avoided. Furthermore, to fully benefit from the component-wise approach, it must be possible to calculate the component modes independently from other connecting components. Occasionally, the component modes have to be obtained directly from measurements. The evolution of CMS has brought forward many different types of component modes. An overview of existing component modes is given in Table 4.1. For a detailed description of the specific component modes, see the references in the mentioned table.

component modes	method	Literature reference
Redundant constraint modes	fixed	Hurty, 1965
Boundary constraint modes	fixed	Craig and Bampton, 1968
Fixed interface normal modes	fixed	Craig and Bampton, 1968
Free interface normal modes	free	Hou, 1969
Residual flexibility modes	free	MacNeal, 1971
Attachment modes	free	Hinz, 1975
Inertia relief modes	free	Hinz, 1975
Residual flexibility modes	free	Rubin, 1975
Boundary inertia relief modes	fixed	Craig and Chang, 1976
Precessional modes	fixed	Glasgow and Nelson, 1980

Table 4.1: *Different types of existing component modes.*

The complex terminology in CMS can be avoided by stating that most CMS techniques can be subdivided into two categories. The subdivision is based on the boundary conditions imposed at the interface DOF of the components:

- Fixed interface methods
- Free interface methods

Each set of component modes usually consists of a *static* and a *dynamic mode set*. In fixed interface methods, both the static and dynamic component modes are calculated while keeping the interface DOF suppressed. In free interface methods, the component modes are calculated while keeping the interface DOF free. The number of modes in the static mode set is governed by the number of interfaces of the component. The number of normal modes in the dynamic mode set is determined by the adopted frequency range. In general, within a certain frequency range, only a limited number of normal modes is required to obtain an accurate solution. These are the *kept normal modes*. The normal modes that are omitted from the component mode set are referred to as the *truncated normal modes*. Sometimes, in the literature hybrid methods are also proposed, but these are merely a combination of the two basic methods mentioned before. The use of undamped normal modes is most efficient when the components are undamped, slightly damped or proportionally damped.

4.3.2 Fixed interface methods

The first developments in CMS were based on fixed interface methods, to enable an easy coupling between connecting substructures. The principle of fixed interface methods can most easily be explained by the beam problem of Figure 4.2. The beam is modelled with finite elements. The interface

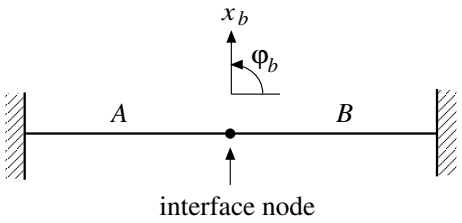

Figure 4.2: *Structure consisting of two beam components.*

node of the beam has one translational DOF x_b and one rotational DOF φ_b. The beam is subdivided into two components, A and B. According to the method of fixed interfaces, for each component, a component mode set must be derived consisting of

- constraint modes
- fixed interface normal modes

The static deformations x_b and φ_b caused by the reaction forces at the interface DOF are described by means of constraint modes. A constraint mode is the resulting displacement field of the beam component caused by a unit displacement or rotation in one of the interface DOF while keeping the other interface DOF zero. It is a static analysis. The first constraint mode for the component on the left hand side (A), with x_b=1 and φ_b=0, is shown in Figure 4.3, the second constraint mode with x_b=0 and φ_b=1 is depicted in Figure 4.4

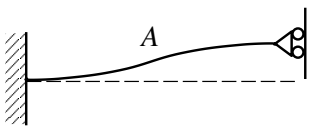

Figure 4.3: *First constraint mode with x_b=1 and φ_b=0.*

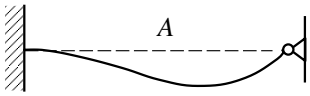

Figure 4.4: *Second constraint mode with x_b=0 and φ_b=1.*

The dynamic mode set consists of the normal modes having fixed interfaces i.e. x_b=0 and φ_b=0. The first fixed normal mode for the component is shown in Figure 4.5. Similar modes must be calculated for the component on the right hand side (B).

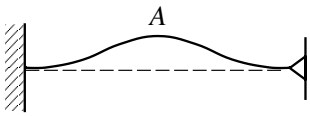

Figure 4.5: *First fixed normal mode with x_b=0 and φ_b=0.*

The number of fixed normal modes that is required for an accurate solution is usually higher than the number of actual normal modes of the component within the frequency range of interest. As a global indicator, it was stated (Wang, 1981) that the frequency of the highest constraint normal mode should be about 35% higher than the upper limit of the frequency band of interest. However, a generalisation of this result is dangerous, since the outcome depends to a large extent on the specific application. A verification is recommended.

Because the normal modes suppress the interface DOF, the method is referred to as a *fixed interface* method. In the fixed interface method, the interface DOF automatically appear in the vector with generalised DOF enabling an easy coupling with other components. In the past, several publications have appeared on this types of component modes, with the objective of making the method more accurate, especially when rigid body motion is involved. One of the most important contributions to fixed interface methods came from Craig and Bampton and, therefore, the method is also referred to as the Craig-Bampton method. Because of its simplicity and high accuracy, their method has been applied successfully in many industrial applications.

4.3.3 Free interface methods

The principle of the free interface method can also be explained by the beam in Figure 4.2. For both components A and B, the component mode set consists of

- Flexibility modes
- Free interface normal modes

A flexibility mode is the resulting displacement field of a component caused by a unit force F_b or a unit moment M_b acting in one of the interface DOF, while keeping all other interface DOF free. Just like constraint modes, flexibility modes account for the static deformation of the assembled system caused by the connecting interface loads between two components. The first flexibility mode for the component on the left hand side (A), with F_b=1 and M_b=0 is shown in Figure 4.6. The second flexibility mode with F_b=0 and M_b=1 is depicted in Figure 4.7.

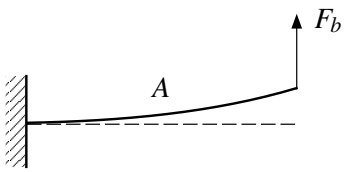

Figure 4.6: *First flexibility mode with F_b=1 and M_b=0.*

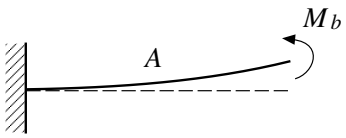

Figure 4.7: *Second flexibility mode with F_b=0 and M_b=1.*

The dynamic mode set consists of the free normal modes. The first normal mode is depicted in Figure 4.8. For the component on the right hand side (B) similar modes must be calculated.

One of the requirements for a proper component mode set is that the interface DOF should appear in the vector with generalised DOF to enable the

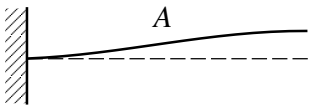

Figure 4.8: *The first free normal mode.*

coupling between the components. For free interface methods this requires an additional transformation procedure in which the generalised DOF $\{p_b\}$ corresponding to the flexibility modes must be replaced by the interface DOF $\{x_b\}$. It can be derived that:

$$\{p_b\} = [\Psi_{bb}^{-1}, -\Psi_{bb}^{-1}\Psi_{bi}]\{x_b\} \tag{4.6}$$

where the subscript b refers to interface DOF and the subscript i to internal DOF.

An important improvement of the free interface method was achieved by the introduction of residual flexibility modes rather than the flexibility modes just described. The residual flexibility of a component represents that part of the flexibility that originates from the truncated normal modes. The residual flexibility matrix $[G^a]$ can be estimated by considering the following expression for the frequency response matrix of an undamped second order system:

$$H_{ii}(\omega) = \sum_{i=1}^{N_e} \frac{\{\Phi_i\}\{\Phi_i\}^T}{\lambda_i^2 - \omega^2} \tag{4.7}$$

where λ_i is the i^{th} natural frequency (rad/s) of the system and $\{\Phi_i\}$ the corresponding normal mode shape. Since the system is described in normal coordinates, the frequency response matrix $[H(\omega)]$ becomes a diagonal matrix. For the truncated modes, it is assumed that $\omega << \lambda_i$ so it follows that:

$$H_{ii}(\omega) = \sum_{i=1}^{n_k} \frac{\{\Phi_i\}\{\Phi_i\}^T}{\lambda_i^2 - \omega^2} + \sum_{i=n_k+1}^{N_e} \frac{\{\Phi_i\}\{\Phi_i\}^T}{\lambda_i^2} \tag{4.8}$$

where n_k is the number of kept normal modes. The last series in equation 4.8 represents the residual flexibility matrix $[G^a]$. It can be obtained by subtracting the contribution of the kept modes from the flexibility matrix $[G] = [K]^{-1}$:

$$[G^a] = [G] - [\Phi_k][\Lambda_k]^{-1}[\Phi_k]^T \tag{4.9}$$

where $[\Lambda_k]$ is the matrix with the kept eigenvalues λ_k^2 stored on the diagonal. Next, the residual flexibility modes $\{\Psi_b\}$ can be calculated by multiplying the residual flexibility matrix $[G^a]$ with the force vectors $\{F_b\}$ of unit load in each of the interface DOF:

$$\{\Psi_b\} = [G^a]\{F_b\} \tag{4.10}$$

In the presence of rigid body motion, the flexibility matrix $[G] = [K]^{-1}$ does not exist and an alternative formulation is required (MacNeal, 1971). The use of residual flexibility modes greatly improves the accuracy and convergence of the free interface methods. The method using free interface normal modes and residual flexibility modes is generally believed to most closely meet the requirements for an optimum component mode set. Furthermore, the method is well suited to the case in which the component modes are to be obtained directly from measurements. However, the calculation of residual flexibility modes is rather complicated and many commercial FEM packages are not able to compute them, which makes the method less interesting in an industrial environment. The latter is the main reason why in the present study the fixed interface method is adopted. All component modes were calculated with the finite element package ANSYS.

4.4 Component mode set for the housings

4.4.1 A new CMS method

The bearing housing together with the outer ring is treated as a single component with linear elastic properties. The outer ring is subjected to a number of rotating concentrated contact loads created in the EHL contacts between the raceway and the rolling elements. Their constitutive behaviour is described in Chapter 3. The outer ring and the housing are modelled with the finite element method. For a time dependent analysis, the finite element model obtained must be reduced. The CMS methods, presented in Sections 4.3.2 and 4.3.3, are not suited for the reduction of structures subjected to rotating or moving loads, simply because the interfaces are assumed to be located at fixed positions. For this reason, a new CMS method is developed, in which an interface surface is defined at which moving interface loads can be applied.

A characteristic of the contact problem in ball bearings is that the radial component of the contact load is to a large extent determined by the actual

position of the balls relative to the housing. The position is influenced by the clearance and by geometrical imperfections on the contacting surfaces in the bearing. The moving load problem for ball bearings is illustrated in Figure 4.9.

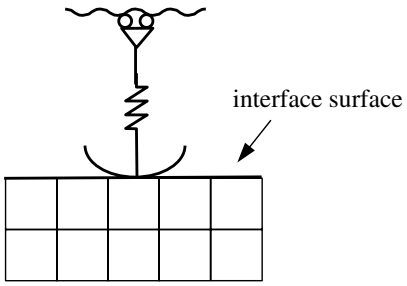

Figure 4.9: *Illustration of the moving load problem encountered in ball bearings.*

For a ball bearing, the whole raceway of the outer ring can be regarded as the interface surface. Consequently, a component mode set based on constraint modes or (residual) flexibility modes will not lead to an efficient reduction, because the number of component modes is proportional to the number of finite element DOF on the interface surface. However, by defining smooth global functions that describe the deformation of the interface surface, a more efficient CMS reduction is obtained.

Another drawback of the use of the constraint modes and flexibility modes presented in Sections 4.3.2 and 4.3.3, is that they only describe the deformation of the interface surface in discrete points, i.e. the finite element nodes. However, in general the point of contact does not match the exact location of these nodes. To determine the deformation at each arbitrary location on the interface surface, one must interpolate between different nodal results. This approach was adopted by Nielsen and Igeland (1995), who investigated a wheel-rail contact. Unfortunately, a method based on low order interpolation is very sensitive to discretisation errors (Rieker, Lin, Trethewey, 1996). In a transient analysis, local discretisation errors cause artificial excitations that disturb the real dynamic behaviour of the application. To reduce the discretisation error, a very fine FEM mesh, with element sizes close to the dimensions of the contact area, must be used. Since this leads to extremely large finite element models, this solution method has not been pursued any

further. Also the use of high order interpolation schemes tends to become very time consuming, because at each time step a new interpolation is required for all ball raceway contacts in the bearing. This can be avoided by describing the deformations of the interface surface with smooth global functions, which can be evaluated at each arbitrary location. Another advantage is that no artificial excitations are generated because the resulting discretisation error is also a smooth continuous function.

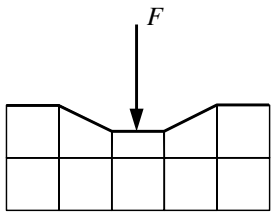

Figure 4.10: *For a concentrated load, the local deformations depend on the mesh size.*

The local deformations caused by the contact load are extremely sensitive to the mesh size in the finite element model. A solution of reasonable accuracy requires at least an element size smaller than the Hertzian contact dimensions, thus leading to a large number of elements. A better solution is to model the local contact deformations with dedicated contact models like the ones based on Hertzian theory. In that case, the adopted CMS method only needs to account for global deformations of the structure with characteristic wavelengths much larger than the dimensions of the area containing local deformations. By definition, constraint modes and flexibility modes represent the displacements caused by point loads. Hence, for small mesh sizes it can be expected that these modes also account for local deformations which are already described by the dedicated contact models. By introducing global functions with characteristic wavelengths longer than the contact area dimensions, this model discrepancy is avoided.

It has to be mentioned that the problem of linear elastic structures subjected to moving or rotating loads frequently occurs in all kind of rotating machinery. Applications for which the new CMS method can be applied are e.g. gear contacts, cutting tools and wheel-rail contacts.

4.4.2 Definition of a new component mode set

In this section, a new component mode set is determined for the bearing housing based on the idea described in the previous section. In this new CMS approach, the displacements of the outer raceway are written as series of smooth analytical functions. The raceway is defined in the cylindrical coordinate system depicted in Figure 4.11.

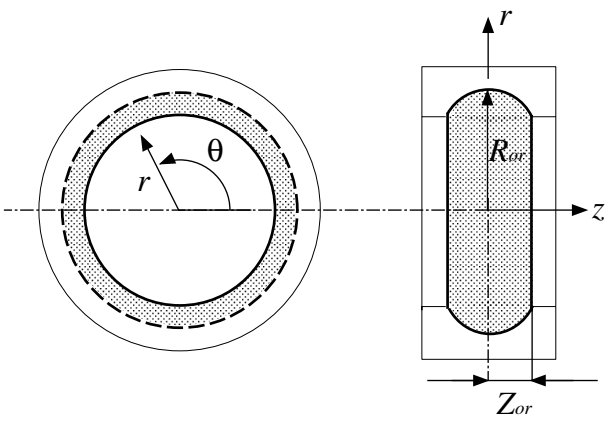

Figure 4.11: *Description of the outer raceway (shaded surface) with cylindrical coordinates.*

In the Hertzian theory it is assumed that contact forces act normal to the contacting surfaces. When friction forces are neglected, this also applies to ball bearings, so the contact forces act perpendicular to the raceway surface. To realise the coupling between the raceway and the rolling elements, the vector with generalised DOF must contain explicitly the radial and axial displacements of the raceway. Because there are no contact forces in the circumferential direction, the displacements tangential to the raceway are eliminated from the vector with generalised DOF. Since the vector with generalised DOF explicitly contains the DOF corresponding to the analytical series, the new component mode set can be classified as a fixed interface method. The component mode set for the bearing housing consists of

- global constraint modes
- fixed interface normal modes

The global constraint modes account for the static deformation of the housing caused by the contact forces in the bearing. The global constraint modes

are related to the analytical series that describe the radial and axial displacements of the raceway. To obtain an efficient component mode set, orthogonal series are introduced. In the circumferential direction Fourier series are used and in both the radial and axial directions Chebyshev polynomials are applied. For an optimum performance, the Chebyshev polynomials are scaled in the radial direction with the radius R_{or} and in the axial direction with the distance Z_{or} (see Figure 4.11).

$$u_r^{or} = \sum_{n=0}^{N_r}\sum_{m=0}^{M_r}\sum_{l=0}^{L_r} a_r(t)\cos(n\theta)\cos(m\arccos(\frac{z}{Z_{or}}))\cos(l\arccos(\frac{r}{R_{or}})) + \\ + \sum_{n=1}^{N_r}\sum_{m=0}^{M_r}\sum_{l=0}^{L_r} b_r(t)\sin(n\theta)\cos(m\arccos(\frac{z}{Z_{or}}))\cos(l\arccos(\frac{r}{R_{or}})) \quad (4.11)$$

$$u_z^{or} = \sum_{n=0}^{N_z}\sum_{m=0}^{M_z}\sum_{l=0}^{L_z} a_z(t)\cos(n\theta)\cos(m\arccos(\frac{z}{Z_{or}}))\cos(l\arccos(\frac{r}{R_{or}})) + \\ + \sum_{n=1}^{N}\sum_{m=0}^{M_z}\sum_{l=0}^{L_z} b_z(t)\sin(n\theta)\cos(m\arccos(\frac{z}{Z_{or}}))\cos(l\arccos(\frac{r}{R_{or}})) \quad (4.12)$$

where a_r, b_r, a_z and b_z denote the new set of interface DOF of the housing, i.e

$$\{x_b\}^T = \{\{a_r\}^T, \{b_r\}^T, \{a_z\}^T, \{b_z\}^T\} \quad (4.13)$$

A global constraint mode is now defined as the resulting displacement field of the housing caused by a prescribed displacement field of unit amplitude in one of the generalised interface DOF a_r, b_r, a_z or b_z, while keeping the others equal to zero. This means that each individual term in the series provides one global constraint mode. All interface DOF end up explicitly in the vector with generalised DOF of the housing, where they represent the time dependent contribution of the corresponding modes . It is noted that the series also account for rigid body motion by means of the first terms in the series n=m=l=0,1. An example of a radial global constraint mode of the housing is illustrated in Figure 4.12.

The Chebyshev polynomials can be written as polynomial expressions with the trigonometric identities. Usually this is done by means of the recurrence formula presented in Appendix B.1. Just like Fourier series, Chebyshev polynomials satisfy certain orthogonality relations, which make them well suited for use in the Ritz method. The calculation of trigonometric functions can be very time consuming in computer programs. A lot of time can

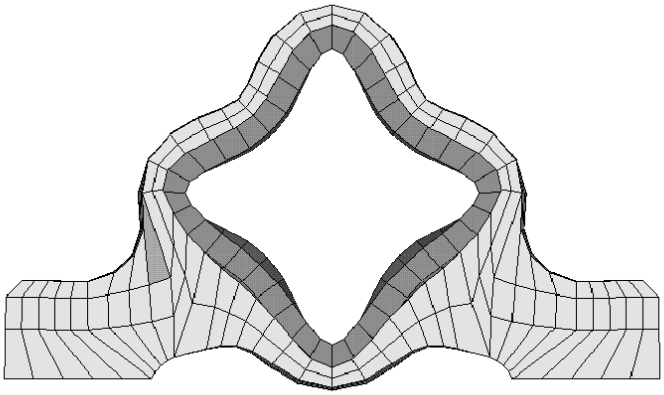

Figure 4.12: *Radial global constraint mode of the bearing housing for* n=4 *and* m=l=0.

be gained by storing frequently used functions and by using Clenshaw's recurrence formula. This is an efficient way to evaluate a sum of coefficients multiplied with functions that obey recurrence formula. For completeness, Clenshaw's recurrence formula are presented in Appendix B.2.

The dynamic mode set of the housing consists of fixed interface normal modes, i.e. the normal modes of the housing with radial and axial displacements of the raceway suppressed. An example of the first fixed interface mode is depicted in Figure 4.13.

In the case of a bearing application, a huge reduction of component modes is obtained by truncation of the series. The degree of the Chebyshev polynomials can usually be kept very small. The number of Fourier series is governed both by the number of kept normal modes and by the ability of the series to describe the static solution. Obviously, the static solution is largely affected by the number of rolling elements in the bearing. The accuracy of the CMS method and the convergence of the series are investigated in Section 4.5.3 for a realistic bearing housing.

The method presented in this section can also be applied to two-dimensional problems. In that case, contact forces act only in the radial plane. Moreover, from the geometry of the raceway, it follows that z=0 and $r = R_{or}$. As a

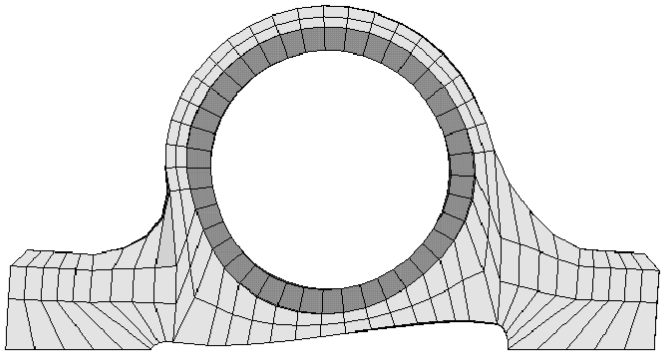

Figure 4.13: *First fixed interface normal mode of the bearing housing with the DOF on the raceway being suppressed in both the radial and axial directions.*

result, the series of analytical functions of equations 4.11 and 4.12 reduce to

$$u_r^{or} = \sum_{n=0}^{N_r} a_r \cos(n\theta) R_{or} + \sum_{n=1}^{N_r} b_r \sin(n\theta) R_{or} \tag{4.14}$$

The model accuracy of the CMS method for a two-dimensional problem was also investigated by the author (Wensing and Nijen, 1996). Here, the CMS method was applied to investigate the effect of waviness on the dynamic behaviour of a bearing housing.

4.4.3 Rigid body motion

The calculation of the global constraint modes requires a number of static analyses. To be able to calculate the static solution, boundary conditions must be defined in *all* coordinate directions to prevent rigid body motions. With CMS, boundary conditions are imposed on all the interface DOF. However, as already mentioned before it is assumed that no contact forces act in the circumferential direction of the raceway and as a result the tangential displacements do not appear in the vector with interface DOF. This means that if there are no other interfaces with prescribed tangential displacements, the global constraint modes cannot be calculated because the inverse of the stiffness matrix $[K]$ in equation 4.1 does not exist. This particular problem is encountered when a ball bearing is mounted on a vibration test

spindle and the outer ring is free to move as a rigid body in all six directions.

The problem of the missing inverse of the stiffness matrix is circumvented by adding an arbitrary tangential DOF of the finite element model to the vector with interface DOF:

$$\{x_b\}^T = \{\{a_r\}^T, \{b_r\}^T, \{a_z\}^T, \{b_z\}^T, u_t\} \tag{4.15}$$

The static mode set is then extended by an additional static mode describing the displacement field caused by a unit displacement of the added tangential DOF, while keeping all other interface DOF zero. The same problem is encountered in two-dimensional models. The accuracy of the presented solution is investigated in Section 4.5.2 for a free bearing outer ring.

4.5 Performance of the new CMS method

4.5.1 Method of evaluation

Before studying assembled systems, the convergence and accuracy of the newly developed CMS method is shown at the component level. The aim of the evaluation is to investigate how many global constraint modes are required to obtain the same modelling accuracy as in classical CMS methods. Moreover, all the components discussed in this section reappear in the following sections as parts of assembled applications.

As a first example, the outer ring of a deep groove ball bearing is considered. The bearing outer ring has six rigid body modes which, as was explained in Section 4.4.3, requires an additional static mode. In a second example, the outer ring of a deep groove ball bearing is considered integrated with an aluminium housing.

The performance of the CMS methods is evaluated by comparing the lowest natural frequencies with the corresponding normal modes of the reduced component with those of the original finite element model. It is inherent to the Ritz method that natural frequencies of the original model are overestimated. The accuracy of the natural mode shapes can be evaluated by computing orthogonality $[O]$ and cross-orthogonality $[XO]$ matrices. It is assumed that the normal modes are mass normalised. Matrix $[\Phi]_{fem}$ contains the normal modes of the finite element model and $[\Phi]_{red}$ the normal

modes of the reduced model.

$$[O] = [\Phi]_{fem}^T [m] [\Phi]_{fem} \tag{4.16}$$

$$[XO] = [\Phi]_{fem}^T [m] [\Phi]_{red} \tag{4.17}$$

To obtain a square matrix for $[XO]$, the natural modes calculated from the finite element model have to be expressed in the generalised DOF. The use of the system's mass matrix leads to a time consuming procedure. A much faster method, which does not involve the mass matrix, is the calculation of the Modal Assurance Criteria or MAC matrix.

$$MAC_{ij} = \frac{\left(\{\Phi_i\}_{red}^T \{\Phi_j\}_{fem}\right)^2}{\left(\{\Phi_i\}_{red}^T \{\Phi_i\}_{red}\right)\left(\{\Phi_j\}_{fem}^T \{\Phi_j\}_{fem}\right)} \tag{4.18}$$

The orthogonality of the mode shape with respect to the mass matrix is not validated with the MAC. However, in the case of a homogeneous mass distribution, an accurate reduction still produces the identity matrix. In the case of coinciding natural frequencies, the natural mode shapes of the reduced system form a linear combination of the natural mode shapes of the original finite element model. The subsequent elements in the MAC matrix must be aggregated. The rigid body modes, for instance, reduce to a single row or column in the MAC matrix. In the present work, the Modal Assurance Criteria method is adopted.

The linear dependence and scaling of the component modes is checked by applying a singular value decomposition on the matrix $[\Psi]$. When the singular values approach zero, the component modes tend to become linearly dependent and the results become sensitive to numerical errors. In the examples presented the singular values are reasonably high and, hence, numerical errors are expected to be small.

4.5.2 Example of a bearing outer ring

For the present investigation, the outer ring of a 6202 deep groove ball bearing is taken. The bearing material is steel. The geometrical properties of a DGBB 6202 are presented in Appendix C. The outer dimensions of the ring are defined according to ISO standards (see also SKF's General Catalogue). The internal geometry is chosen by the ball bearing manufacturer and is of a competitive nature.

A finite element model of the bearing outer ring is built with solid brick elements. The roundings and the shield groove are not modelled. The solid brick elements used have quadratic shape functions. The resulting finite element model contains 288 elements and 2,256 nodes. Each finite element node contains 3 DOF, so the total number of DOF equals 6,768. The total mass of the bearing outer ring is approximately 22 g. Because of symmetry, the first two natural frequencies of the outer ring are accompanied by two similar normal modes, which can only be distinguished by a phase shift in the spatial domain. As a result, the natural vibrations of the outer ring can be described by any linear combination of the two modes. In Figures 4.14 and 4.15, one of the normal modes is depicted for the first two distinct natural frequencies of the outer ring.

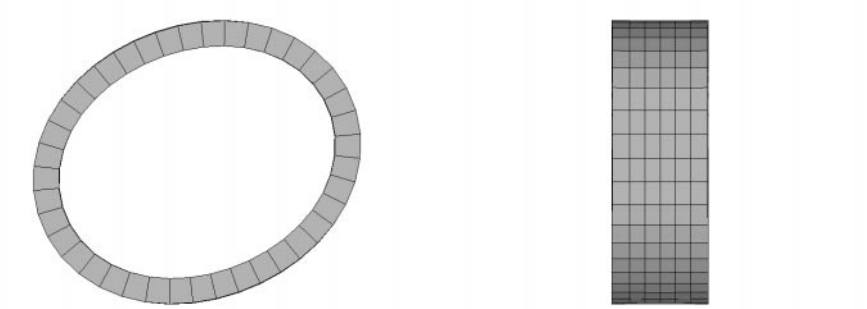

Figure 4.14: *Normal mode of a DGBB* 6202 *outer ring at* 6,626 Hz.

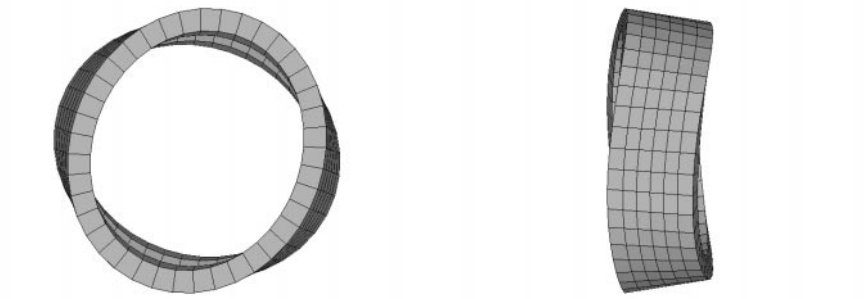

Figure 4.15: *Normal mode of a DGBB* 6202 *outer ring at* 11,776 Hz.

The finite element model is reduced using the CMS method presented in Section 4.4. The outer ring is able to move as a rigid body and thus an additional mode shape is required as explained in Section 4.4. The accuracy of the CMS reduction is investigated by varying the number of Fourier terms $N_r = N_z$, and the number of Chebyshev polynomials M_r, L_r, M_z and L_z in equations 4.11 and 4.12. Also, the number of fixed interface normal modes H is changed. As a measure for the accuracy, in Table 4.2 the relative error ϵ_i of the i^{th} natural frequency and the i^{th} diagonal term of the MAC matrix are calculated. When less than 21 generalised DOF are used,

							$f_1 = 6{,}626$ Hz		$f_2 = 11{,}776$ Hz	
DOF	N_r	M_r	L_r	M_z	L_z	H	$\epsilon_1\%$	MAC_{11}	$\epsilon_2\%$	MAC_{22}
21	2	1	0	0	1	0	0.94	0.99992	0.68	0.99997
31	2	1	0	0	1	10	0.84	0.99994	0.24	0.99999
41	2	1	0	1	1	10	0.15	0.99998	0.24	0.99997
41	2	1	1	0	1	10	0.82	0.99993	0.04	0.99999
51	2	1	1	1	1	10	0.07	0.99999	0.04	0.99999
61	2	2	1	1	1	10	0.03	0.99999	0.04	0.99999

Table 4.2: *Convergence of the new CMS method for a DGBB* 6202 *outer ring.*

the error very quickly increases because then the basic shapes necessary for the description of the normal modes are missing. The effect of harmonics ($N_r = 4$) is very small because of the circular geometry. Moreover, it is observed from Table 4.2 that the effect of fixed interface normal modes is very small because the mass distribution is similar to the stiffness distribution. The lowest natural frequency of the constraint normal modes equals 49 kHz.

From the investigations so far, it can be concluded that 21 generalised DOF are sufficient to accurately model the dynamic behaviour up to 20 kHz. However, in case of a bearing outer ring, the number of generalised DOF is not only determined by the ability of the series to describe the dynamic behaviour, but also by the ability to describe the static solution. Obviously, the static deformation depends on the interface loads applied by the rolling elements. To incorporate the static deformation caused by the passing rolling elements, it can be expected that the number of Fourier terms in equations 4.11 and 4.12 should be at least equal to the number of rolling elements. For a DGBB 6202 this means that $N_r = N_z \geq 8$. An investigation of the actual static deformation field of the outer ring loaded by eight

rolling elements shows that at least a second order Chebyshev polynomial is required for the radial displacement field.

The static deformation field of a DGBB 6202 outer ring is depicted in Figure 4.16. The ring is loaded with eight equally distributed interface loads at the centre of the raceway (contact angle is zero). The axial and tangential displacements of the loaded nodes are suppressed to obtain a statically determined structure. Consequently, extensional deformations of the ring are suppressed.

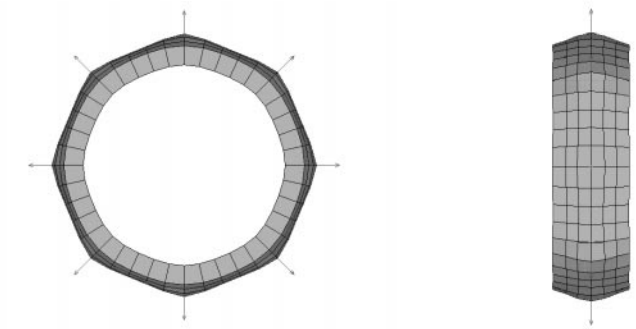

Figure 4.16: *Static solution of a DGBB* 6202, *uniformly loaded by eight equal contact forces.*

So far, it can be concluded that in order to incorporate all the essential deformations of the bearing outer ring with reasonable accuracy, at least 85 global constraint modes are required for the static mode set. It can also be concluded that the extra mode shape required to enable rigid body motion of the outer ring does not affect the overall accuracy of the CMS method. For the bearing outer ring, the 35% criterion stated by Wang (see Section 4.3.2) would result in one fixed normal mode. This does not give satisfying results. For the bearing outer ring at least three fixed normal modes are required. The resulting number of generalised DOF equals 89.

4.5.3 Example of a bearing housing

In addition to the example of a bearing outer ring a typical bearing housing is considered. The bearing housing is made of aluminium and contains the steel DGBB 6202 outer ring of the previous section. The outer ring is

connected to the housing by assuming compatible displacement fields. At the bottom, a bolt fixture is assumed and the displacements of the bearing housing are suppressed. The housing is modelled with solid brick elements that have quadratic shape functions. The resulting finite element model contains 1,312 elements and 7,278 nodes. The total number of active DOF equals 19,832. The first two natural modes of the housing are illustrated in Figures 4.17 and 4.18.

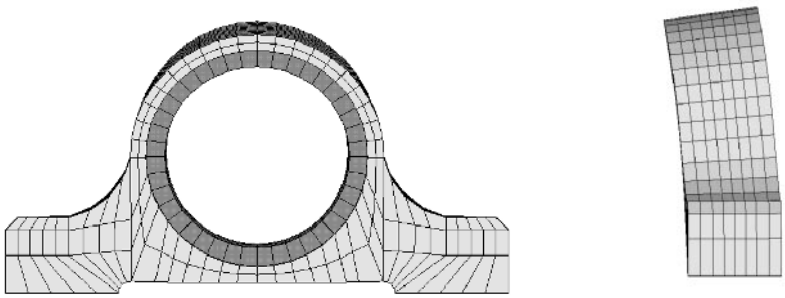

Figure 4.17: *First normal mode of the aluminium housing at* 5,529 Hz.

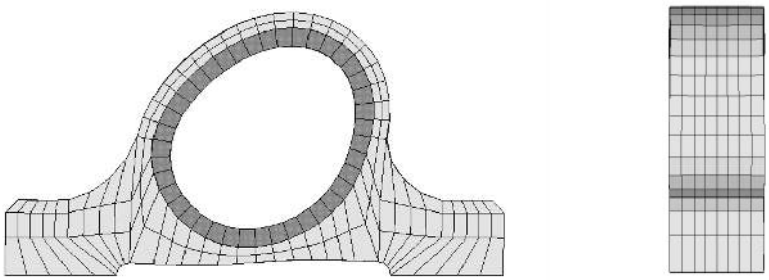

Figure 4.18: *Second normal mode of the aluminium housing at* 8,993 Hz.

Again the finite element model is reduced with the CMS method of Section 4.4 and the number of Fourier terms, the number of Chebyshev terms and the number of fixed interface normal modes are varied. In Table 4.3, the relative error of the natural frequencies and the diagonal terms of the MAC matrix are presented for the first two normal modes of the bearing housing. Compared with the example of a bearing outer ring, the harmonics

							f_1 = 5,529 Hz		f_2 = 8,993 Hz	
DOF	N_r	M_r	L_r	M_z	L_z	H	ϵ_1%	MAC_{11}	ϵ_2%	MAC_{22}
21	2	1	0	0	1	0	1.21	0.99960	12.0	0.97790
31	2	1	0	0	1	10	1.20	0.99959	10.3	0.98407
46	4	1	0	0	1	10	0.18	0.99999	2.00	0.99961
78	8	1	0	0	1	10	0.12	0.99999	0.36	0.99996
88	8	1	0	0	1	20	0.02	0.99999	0.30	0.99998
105	8	2	0	0	1	20	0.02	0.99999	0.24	0.99998

Table 4.3: *Convergence of the new CMS method for the aluminium housing with the DGBB* 6202 *outer ring.*

$N_r = 2, 4...$ have become much more important because the geometry of the component is no longer axially symmetric. The influence of the fixed interface normal modes has increased. This is also indicated by the frequency of the lowest fixed interface normal mode, which is 24.7 kHz. Up to 20 kHz, the housing has four more natural frequencies. However, the total amount of constraint modes is still determined by the ability of the series to describe the static deformation field. Just as for the outer ring, at least 85 global constraint modes are recommended for the static mode set. In this study, ten fixed interface normal modes were used for the dynamic mode set, leaving a total of 95 generalised DOF for the complete housing. In Table 4.4 the relative error is given for all natural frequencies below 20 kHz based on a reduction of up to 95 generalised DOF.

i	frequency	ϵ_i
1.	5,529 Hz	2e-4
2.	8,993 Hz	2e-3
3.	11,533 Hz	8e-4
4.	13,363 Hz	3e-3
5.	15,651 Hz	2e-3

Table 4.4: *Error of the natural frequencies of the aluminium housing with the DGBB* 6202 *outer ring after a CMS reduction to 95 DOF.*

The results in Tables 4.4, 4.3 and 4.2 show the good performance of the present CMS method. In all cases, a huge model reduction is obtained, while the principal dynamic behaviour is still accurately described in the frequency range of interest. This also includes the static solution.

4.6 Component mode set for the shaft

Both CMS methods presented in Sections 4.3.2 and 4.3.3 are well suited for the modelling of flexible shafts. In the present study, the fixed interface method has been adopted, mainly because of practical reasons. The component modes can be calculated directly using a commercial finite element package. The component mode set for the shaft consists of:

- Fixed interface normal modes
- Constraint modes

The component modes also account for the rigid body motion of the shaft in all six DOF. Optionally, inertia relief modes can be used to increase the convergence and accuracy of the method (Craig and Chang, 1976).

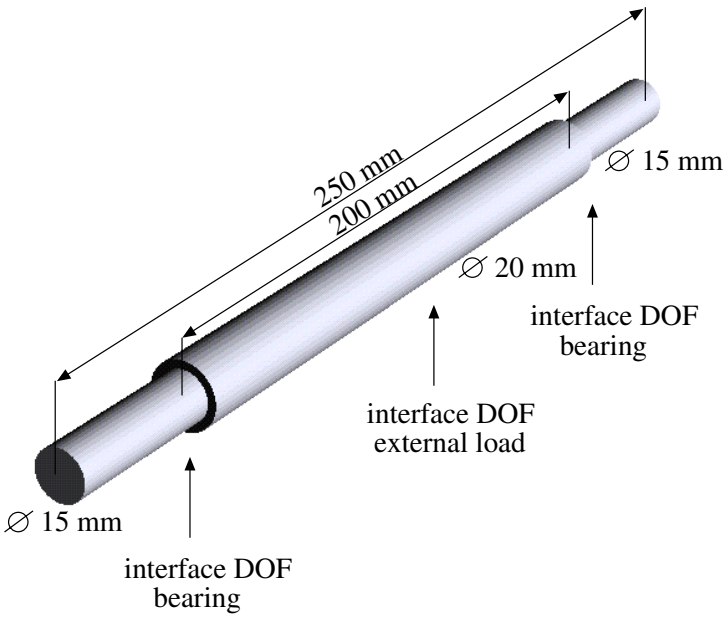

Figure 4.19: *Geometry of the flexible shaft indicating the location of the interface DOF.*

The circular shaft shown in Figure 4.19 is made out of steel (ρ= 7800 kg/m^3, $E = 210 \cdot 10^9$ N/m^2) and weighs 0.628 kg. In the middle, the shaft diameter

is somewhat larger to position the bearing inner rings. Gyroscopic effects are neglected. The shaft was modelled in ANSYS with 80 beam elements (PIPE16) of circular cross section. The total number of finite element DOF equals 246. Three interface DOF are defined. Two interface DOF are used for the coupling of the shaft with the bearings and one interface DOF is used to apply external loads. As a result, the total number of constraint modes equals 6x3=18. The number of fixed interface normal modes equals 16 and is based on the 35% rule proposed by Wang (see Section 4.3.2). The final model is reduced from 246 finite element DOF down to 34 generalised DOF.

In Table 4.5, the relative error ϵ is given between the first four natural bending frequencies of the reduced shaft model and the corresponding natural frequencies of the original finite element model. Because the shaft is axially symmetric, all natural frequencies exist in pairs. Table 4.5 shows the excellent performance of the applied CMS method.

i	frequency	ϵ_i
1.	1,168 Hz	4e-5
2.	2,782 Hz	4e-5
3.	4,752 Hz	8e-4
4.	7,207 Hz	2e-3

Table 4.5: *Relative error between the natural frequencies of the reduced CMS model and the original FEM model of the shaft.*

Chapter 5

Modelling of applications

A model is presented with which the dynamic behaviour can be studied of a rotor dynamic application containing ball bearings (see Figure 5.1). The equations of motion of the model are derived with the help of Lagrange's equations.

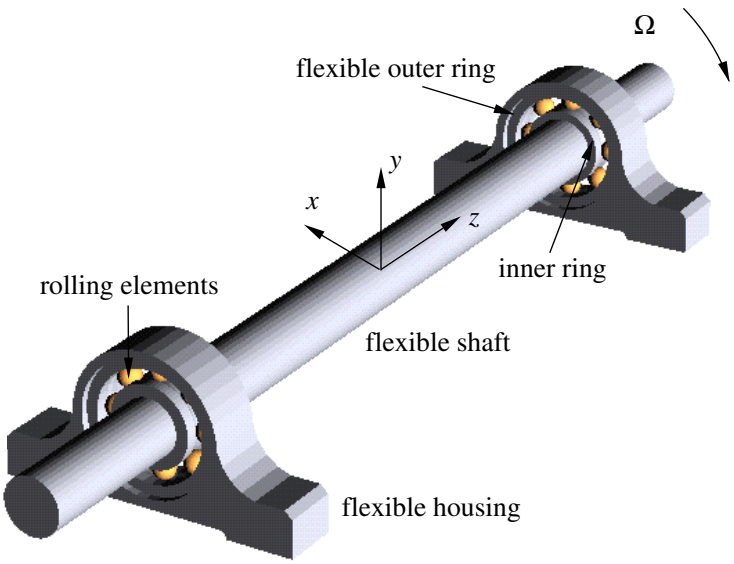

Figure 5.1: *Model of a rotor dynamic application containing ball bearings.*

The model consists of a flexible shaft supported by two similar deep groove ball bearings both mounted in flexible housings. In the present approach

the bearings and the housings are treated in a similar way from a modelling point of view. For that reason, the equations of motion are presented only for one bearing and one housing.

The outer rings of the bearings are flexible. The inner rings and the rolling elements are assumed to be rigid, except for local deformations in the contacts. The stiffness and damping in the lubricated contacts between the rolling elements and the raceway are described using the contact model presented in Chapter 3. The contact model is used to couple the rotating shaft with the fixed inner rings to the housings with the mounted outer rings.

The housing and the outer ring are treated as a single component with linear elastic material properties. The connection between the outer ring and the housing is described with a linear constitutive relation so that component mode synthesis can be applied. The constitutive relation is implemented in the finite element model with the help of constraint equations between the DOF of the outer ring and the DOF of the housing at their joint interface.

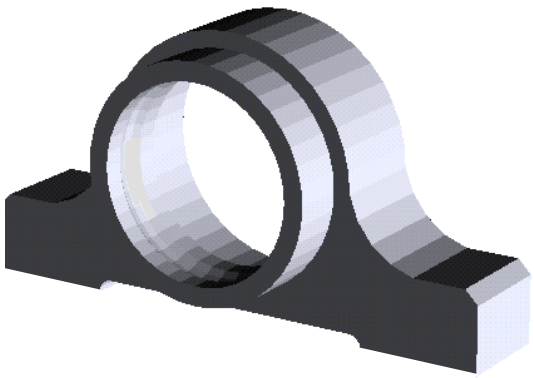

Figure 5.2: *Rigid body mode of the outer ring as a result of the "loose" fit between the outer ring and the housing.*

Often the bearing outer ring can move freely in the axial direction in order to compensate for temperature effects of the shaft and for the application of an axial pre-load to the outer ring of the bearing. In that case the bearing outer ring has one rigid body DOF in the axial direction, as shown in Figure 5.2. The construction of an accurate constitutive model for the connection between the outer ring and the housing bore is beyond the scope of this re-

search. In the present model, it is assumed that one of the outer rings is free to move in the axial direction. In the radial plane the ring is still connected to the housing by equating the radial and the tangential displacements of the outer ring to those of the housing at their joint interface.

For the other outer ring it is assumed that at the interface with the housing all the displacements of the outer ring are equal to the displacements of the housing. Each unit consisting of a housing and an outer ring is modelled with solid elements. Their model size is reduced by component mode synthesis and the dynamic behaviour is described by means of the generalised DOF that represent the contributions of pre-defined component modes. For the housing with the outer ring the new component mode set, presented in Section 4.4, is applied.

The circular shaft in Figure 4.19 has linear elastic material properties and rotates with a constant angular speed. The shaft is modelled with beam elements. The model size is reduced with component mode synthesis as described in Section 4.6. The inner ring of the bearing is press-fitted on the shaft. Hence, it can be expected that the flexural deformations of the inner ring are small. The only remaining significant deformations are the local deformations in the lubricated contacts. The inner ring is modelled as a rigid body and its dynamic behaviour is described by three translational DOF and two rotational DOF. The third rotational DOF of the inner ring is prescribed, since the rotational speed of the inner ring is equal to the rotational speed of the shaft. At the interface between the inner ring and the shaft, the DOF of the inner ring are compatible with the generalised DOF of the shaft.

Apart from the local deformations in the lubricated contacts, the rolling elements are modelled as rigid bodies. The dynamic behaviour of each rolling element is described by translational DOF only, which means that the rotational inertia of the rolling elements is neglected. The rolling elements are guided by the cage and rotate about the central axis of the bearing with an angular speed Ω_c. The angular speed is proportional to the rotational speed of the inner ring and depends on the internal geometry of the bearing. Also, the rolling elements rotate with an angular speed Ω_{re} about their own central axis. In Figure 5.3 it can be observed that, if the rolling elements operate at a contact angle α, the direction of the central axis of the bearing and the direction of the central axes of the rolling elements do not coincide. This causes gyroscopic forces and spinning motion of the rolling elements. In Figure 5.3, the spin velocity is denoted by Ω_s. Usually, the gyroscopic

forces are resisted by friction forces and for that reason it is justified not to include them in the model.

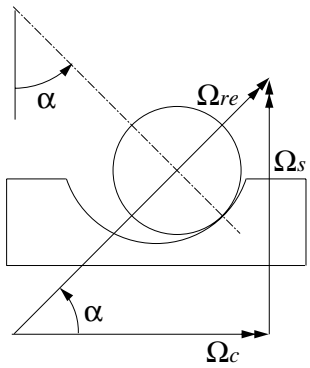

Figure 5.3: *Rotational velocities of a rolling element.*

As a rule, the rolling elements are pressed between the inner and outer ring of the bearing. The rolling elements are separated from the raceway by a thin lubricant film. Each lubricated contact between a rolling element and the raceway is described by a spring-damper model.

The stiffness in the contact can be represented by a nonlinear spring. Under load the spring can take different contact angles. Because these contact angles α are not necessarily small, they are not linearised and the contacts become geometrically nonlinear. As a result of this nonlinearity second order derivatives of the mutual approach do not vanish. In fact, they provide an additional term in the stiffness matrix of the bearing. Due to this second order effect, the rolling elements experience not only a stiffness in the direction normal to the contact but also in the tangential direction. The latter implies that, in general, a force is required to change the contact angle in a pre-loaded bearing. Because this second order effect is the only contribution to the stiffness in the tangential direction, it cannot be neglected.

Since the tangential contact stiffness is much lower than the Hertzian stiffness normal to the contact, it can be expected that the lowest resonances in the bearing will have large contact angle variations. To be able to describe the damping of these resonances, a linear viscous damper is introduced that operates tangential to the contacting surfaces. To be able to describe the

damping of resonances with large variations of the mutual approach a second linear viscous damper is introduced operating normal to the contact (see Figure 5.4).

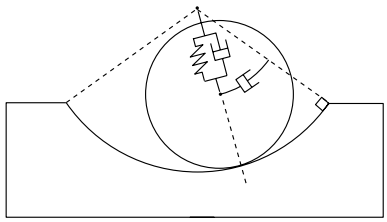

Figure 5.4: *The spring damper model that describes an EHL contact in the three-dimensional bearing model.*

The cage is not modelled as a structural element. Cages are relatively soft elements in the bearing. Hence, the contact forces between the cage and the rolling elements are expected to be small compared to the contact forces between the rolling elements and the raceway. The omission of cage effects greatly reduces the size and complexity of the bearing model.

5.1 Lagrange's equations

The equations of motion that describe the dynamic behaviour of the complete model can be derived using Lagrange's equations. They read:

$$\frac{d}{dt}\frac{\partial T}{\partial\{\dot{p}\}} - \frac{\partial T}{\partial\{p\}} + \frac{\partial V}{\partial\{p\}} + \frac{\mathcal{F}}{\partial\{\dot{p}\}} = \{f\} \tag{5.1}$$

where: T = kinetic energy
V = potential energy
$\mathcal{F}$ = Rayleigh's dissipation function
$\{f\}$ = vector with generalised external forces
$\{p\}$ = vector with generalised DOF

The kinetic, potential and dissipation energies can be subdivided into the contributions from the various components, i.e. from the shaft, from the inner ring, from the housing with the outer ring and from the rolling elements.

The total kinetic energy amounts to:

$$T = T^{sh} + T^{ir} + T^{ho} + \sum_{j=1}^{Z} T_j^{re} \tag{5.2}$$

where Z equals the total number of rolling elements. The superscripts *sh*, *ir* and *ho* refer to, respectively, the shaft, the inner ring and the housing with the outer ring. The rolling elements are indicated by the superscript *re* and the subscript j refers to the element under consideration.

The potential energy is provided by the elastic deformations of the shaft and the housing with the outer ring and by the local elastic deformations in the EHL contacts. The contacts between the rolling elements and the raceway of the outer ring are indicated by the superscript *oc* and the contacts between the rolling elements and the raceway of the inner ring by the superscript *ic*. The potential energy reads:

$$V = V^{sh} + V^{ho} + \sum_{j=1}^{Z} V_j^{ic} + \sum_{j=1}^{Z} V_j^{oc} \tag{5.3}$$

Rayleigh's dissipation function contains the energy dissipated via material damping in the structural elements and the energy dissipated via the EHL contacts by the viscous losses in the lubricant. Local hysteresis in the EHL contacts is neglected. For Rayleigh's dissipation function it follows that:

$$\mathcal{F} = \mathcal{F}^{sh} + \mathcal{F}^{ho} + \sum_{j=1}^{Z} \mathcal{F}_j^{ic} + \sum_{j=1}^{Z} \mathcal{F}_j^{oc} \tag{5.4}$$

The energy dissipated in the EHL contacts can be attributed to a damper operating normal to the contacting surfaces and one operating in the tangential direction (see Figure 5.4).

The generalised DOF $\{p\}$ consist of the generalised DOF of the shaft and the housing and the DOF of the rolling elements. It follows that:

$$\{p\}^T = \{\{p^{sh}\}^T, \{p^{ho}\}^T, \{x^{re}\}^T\} \tag{5.5}$$

In contrast with the generalised DOF of the housings and the shaft, the DOF of the rolling elements are physical DOF. The potential energy and the dissipated energy of the inner and outer contacts depend on the mutual approach

between the centres of curvature of the contacting bodies. In order to derive the final equations, the mutual approaches must be expressed in terms of the generalised DOF $\{p\}$. In order to calculate the dissipated energy, the time rate of change of the mutual approach must also be determined for each contact.

5.1.1 Contribution of the inner ring

Apart from local deformations in the contacts, the inner ring is considered as a rigid body. To describe the position and the orientation of the ring, an inertial clockwise Cartesian reference frame is defined with axes x_0, y_0 and z_0 and a second Cartesian frame is defined fixed to the inner ring with axes x, y and z. The position of the origin of the moving frame relative to the reference frame is described by three translational DOF, u_x^{ir}, u_y^{ir} and u_z^{ir}. The orientation of the moving frame relative to the reference frame

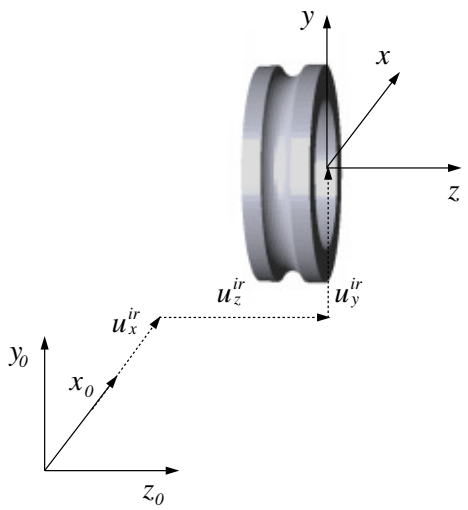

Figure 5.5: *Definition of the coordinate frames and the translational DOF of the inner ring.*

is described by three angles, ϕ^{ir}, ψ^{ir} and θ^{ir}. Following the definition of Bryant angles, first, the inner ring is rotated by an angle ϕ^{ir} about the x_0-axis, then by an angle ψ^{ir} about the new $y-$axis, denoted by y_1, and finally, by an angle θ^{ir} about the $z-$axis. The rotations are shown in Figure 5.6.

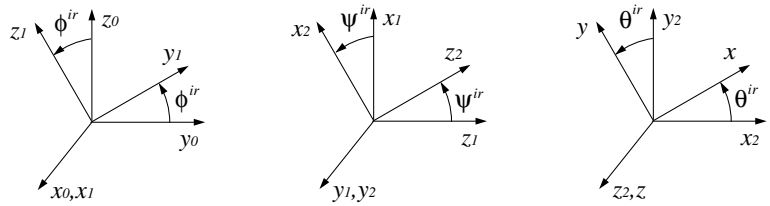

Figure 5.6: *Definition of the rotational DOF according to Bryant by three subsequent rotations.*

The kinetic energy of the inner ring about its centre of mass is evaluated in the $x-$, $y-$, $z-$ frame. For the angular velocity vector we can derive:

$$\{\omega\} = \dot{\phi}^{ir}[R_\theta][R_\psi]\{e_{x1}\} + \dot{\psi}^{ir}[R_\theta]\{e_{y2}\} + \dot{\theta}^{ir}\{e_z\} \tag{5.6}$$

where $\{e_{x1}\}$, $\{e_{y2}\}$ and $\{e_z\}$ are unit vectors along the x_1-, y_2- and $z-$ axes. Note that $\{e_{x1}\}$=$\{e_{x0}\}$, $\{e_{y2}\}$=$\{e_{y1}\}$ and $\{e_z\}$=$\{e_{z2}\}$. The two elementary rotation matrices in equation 5.6 are given by

$$[R_\theta] = \begin{bmatrix} \cos\theta^{ir} & \sin\theta^{ir} & 0 \\ -\sin\theta^{ir} & \cos\theta^{ir} & 0 \\ 0 & 0 & 1 \end{bmatrix} \tag{5.7}$$

$$[R_\psi] = \begin{bmatrix} \cos\psi^{ir} & 0 & -\sin\psi^{ir} \\ 0 & 1 & 0 \\ \sin\psi^{ir} & 0 & \cos\psi^{ir} \end{bmatrix} \tag{5.8}$$

Substitution of equations 5.7 and 5.8 in equation 5.6 results in the following expression for the angular velocity vector:

$$\{\omega\} = \begin{Bmatrix} \omega_x \\ \omega_y \\ \omega_z \end{Bmatrix} = \begin{Bmatrix} \dot{\phi}^{ir}\cos\psi^{ir}\cos\theta^{ir} + \dot{\psi}^{ir}\sin\theta^{ir} \\ -\dot{\phi}^{ir}\cos\psi^{ir}\sin\theta^{ir} + \dot{\psi}^{ir}\cos\theta^{ir} \\ \dot{\theta}^{ir} + \dot{\phi}^{ir}\sin\psi^{ir} \end{Bmatrix} \tag{5.9}$$

The mass of the inner ring is denoted by m^{ir} and the mass moment of inertia matrix in the principal direction is given by

$$[I^{ir}] = \begin{bmatrix} I_x^{ir} & 0 & 0 \\ 0 & I_y^{ir} & 0 \\ 0 & 0 & I_z^{ir} \end{bmatrix} \tag{5.10}$$

The expression for the kinetic energy of the inner ring reads:

$$T^{ir} = \tfrac{1}{2}m^{ir}\left(\dot{u}_x^{ir\,2} + \dot{u}_y^{ir\,2} + \dot{u}_z^{ir\,2}\right) + \tfrac{1}{2}\left(I_x^{ir}\omega_x^2 + I_y^{ir}\omega_y^2 + I_z^{ir}\omega_z^2\right) \quad (5.11)$$

The expression can be simplified because the ring is axially symmetric and thus $I_x^{ir} = I_y^{ir}$. Furthermore, the angles ϕ^{ir} and ψ^{ir} are small and the angular velocity around the z-axis is constant i.e. $\dot{\theta}^{ir} = \Omega_{ir}$. After these simplifications the expression for the kinetic energy of the inner ring reads:

$$\begin{aligned} T^{ir} = \tfrac{1}{2}m^{ir}\left(\dot{u}_x^{ir\,2} + \dot{u}_y^{ir\,2} + \dot{u}_z^{ir\,2}\right) + \tfrac{1}{2}I_x^{ir}\dot{\phi}^{ir\,2} + I_y^{ir}\dot{\psi}^{ir\,2} + \\ + \tfrac{1}{2}I_z^{ir}\left(\Omega_{ir}^2 + 2\Omega_{ir}\dot{\psi}^{ir}\phi^{ir}\right) \end{aligned} \quad (5.12)$$

where $I_z^{ir}\Omega_{ir}\dot{\psi}^{ir}\phi^{ir}$ represents the gyroscopic effect. The term $\frac{1}{2}I_z^{ir}\Omega_{ir}^2$ is constant and has no influence on the force balance.

5.1.2 Contribution of the rolling elements

The rolling elements are also considered as rigid bodies. For the determination of their contribution to the kinetic energy, the position of the j^{th} rolling element is described by two translational DOF, u_{rj}^{re} and u_{zj}^{re}, which means that the mass moment of inertia of a rolling element with respect to its mass centre is neglected. The translational DOF are defined in a cylindrical coordinate frame, of which the origin coincides with the origin of the inertial frame of the inner ring (see Figure 5.7). As a reference for the radial DOF u_{rj}^{re} the pitch radius R_p is taken.

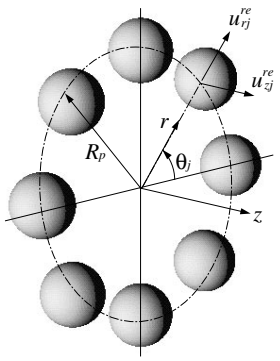

Figure 5.7: *Definition of the coordinate frame with the translational DOF of the rolling elements.*

No DOF's are defined in the tangential direction. The tangential coordinate θ_j of a rolling element is known because the rolling element set rotates at a constant angular speed about the central axis of the bearing. In the literature, the angular speed of the rolling element set is also referred to as the cage speed. The relation between the angular speed of the rolling element set, denoted by Ω_c, and the inner ring or shaft speed, denoted by Ω_{ir}, reads:

$$\Omega_c = \frac{\Omega_{ir}}{2}\left(1 - \frac{R_{re}\cos(\alpha)}{R_p}\right) \tag{5.13}$$

where R_{re} is the ball radius and α the average contact angle of the rolling elements. Due to the time dependent load distribution in the application, α may vary in time. However, since a variation of α has only a very small influence on Ω_c, it is treated as a constant. For the tangential coordinate of the j^{th} rolling element, we can derive:

$$\theta_j = \Omega_c t + \frac{2\pi}{Z}(j-1), \quad j = 1..Z \tag{5.14}$$

where t is the time coordinate and Z the total number of equally spaced rolling elements. All rolling elements have the same mass, here denoted by m^{re}. The kinetic energy of the j^th rolling element reads:

$$T_j^{re} = \tfrac{1}{2}m^{re}\left(\dot{u}_{rj}^{re2} + \dot{u}_{zj}^{re2} + (R_p + u_{rj}^{re})^2\Omega_c^2\right) \tag{5.15}$$

The last term on the right hand side of equation 5.15 also accounts for centrifugal effects.

5.1.3 Contribution of the housing

The housing and the outer ring are modelled with the finite element method (SOLID95, ANSYS) as one unit. Subsequently, the system matrices are reduced with component mode synthesis. The dynamic behaviour of the system is described with generalised DOF that represent the contributions of pre-defined component modes, as defined in Section 4.4. The kinetic energy of the bearing housing reads:

$$T^{ho} = \tfrac{1}{2}\{\dot{p}^{ho}\}^T[m^{ho}]\{\dot{p}^{ho}\} \tag{5.16}$$

The contribution of the flexible unit consisting of the housing and the outer ring to the potential energy amounts to:

$$V^{ho} = \tfrac{1}{2}\{p^{ho}\}^T[k^{ho}]\{p^{ho}\} \tag{5.17}$$

Usually in a flexible structure, a small amount of material damping is present. In this study the material damping is modelled as proportional viscous damping and, therefore, modal decoupling is allowed. The following definition is used:

$$[c^{ho}] = [u^{ho}]^{-T}[c_d^{ho}][u^{ho}]^{-1} \tag{5.18}$$

where $[u^{ho}]$ is the matrix with eigenvectors, which is the solution of the reduced undamped eigenvalue problem. The matrix $[c_d^{ho}]$ is a diagonal matrix, which contains the viscous damping coefficients c_i for each decoupled modal equation of the housing. The relation between c_i and the dimensionless damping constant ζ_i is given by

$$c_i = 2\zeta_i m_i \omega_i \tag{5.19}$$

where m_i is the corresponding modal mass and ω_i the corresponding undamped natural frequency in radians per second. For steel or aluminium, common values for ζ_i range from 0.1% to 0.5%. The contribution of the bearing housing to Rayleigh's dissipation function finally reads:

$$\mathcal{F}^{ho} = \tfrac{1}{2}\{\dot{p}^{ho}\}^T[c^{ho}]\{\dot{p}^{ho}\} \tag{5.20}$$

5.1.4 Contribution of the shaft

The axially symmetric shaft is modelled with beam elements (PIPE16, ANSYS). The system matrices of the shaft are reduced with component mode synthesis and its dynamic behaviour is described with generalised DOF that represent the contributions of pre-defined component modes as defined in Section 4.3.2. The kinetic energy of a symmetric shaft rotating at a constant angular speed Ω reads:

$$T^{sh} = \tfrac{1}{2}\{\dot{p}^{sh}\}^T[m^{sh}]\{\dot{p}^{sh}\} + \tfrac{1}{2}I_z^{sh}\Omega^2 \tag{5.21}$$

where I_z^{sh} denotes the mass moment of inertia about the axis of rotation of the shaft. In the present work, gyroscopic effects are neglected. For ways to include gyroscopic coupling, the reader is referred to the literature (Childs, 1993).

The contribution of the flexible shaft to the potential energy amounts to:

$$V^{sh} = \tfrac{1}{2}\{p^{sh}\}^T[k^{sh}]\{p^{sh}\} \tag{5.22}$$

In the shaft, a small amount of material damping is assumed. The same damping model is adopted as for the bearing housings (see equations 5.18

and 5.19). The contribution of the shaft to Rayleigh's dissipation function reads:

$$\mathcal{F}^{sh} = \tfrac{1}{2}\{\dot{p}^{sh}\}^T[c^{sh}]\{\dot{p}^{sh}\} \tag{5.23}$$

5.1.5 Contribution of the EHL contacts

The contact forces in the lubricated contacts can be divided into elastic restoring forces and dissipative forces. The restoring forces contribute to the potential energy and the dissipative forces contribute to Rayleigh's dissipation function.

The potential energy

The restoring contact forces F_e depend in a nonlinear way on the mutual approach δ. The potential energy, obtained after integration, yields:

$$V = \int_0^{\delta} F_e(\delta')d\delta' \tag{5.24}$$

In a dry contact, the restoring contact forces are described by means of the Hertzian solution. For convenience this solution, given previously by equation 3.19, is recalled:

$$F_e = \kappa\delta^{3/2}H(\delta) \qquad \kappa = \frac{\pi\epsilon E'}{3\mathcal{K}}\sqrt{\frac{2\mathcal{E}R}{\mathcal{K}}} \tag{5.25}$$

where $H(\delta)$ is the Heaviside step function. After substitution of equation 5.25 in equation 5.24, the following expression is obtained for the potential energy of the j^{th} inner contact:

$$V_j^{ic} = \tfrac{2}{5}\kappa^{ic}{\delta_j^{ic}}^{\frac{5}{2}}H(\delta_j^{ic}) \tag{5.26}$$

For the j^{th} outer contact, a similar expression is obtained. In the lubricated contacts, the restoring forces are described by a dimensionless relation based on a curve-fit of the results of numerical simulations. The relation, given earlier by equation 3.43, reads:

$$\Delta(N, L) = 1 - p(L)N^{q(L)} \tag{5.27}$$

with:

$$p(L) = \left((4 - 0.2L)^7 + (3.5 + 0.1L)^7\right)^{\frac{1}{7}} \tag{5.28}$$

$$q(L) = \left(-(0.6 + 0.6(L + 3)^{-\frac{1}{2}}\right)^{\frac{1}{7}} \tag{5.29}$$

The quantity Δ is the mutual approach between the contacting bodies *scaled* on the Hertzian deformation and N is a dimensionless quantity, which is proportional to the static load F_e. The parameter L is also dimensionless but independent of the load. As opposed to the Hertzian solution, in equation 5.25, the contact load is not expressed as a function of the mutual approach but the mutual approach is expressed as a function of the contact load. By means of a coordinate transformation, the following formulation is obtained for the potential energy of the inner contacts:

$$V_j^{ic} = \int_0^{F_{ej}^{ic}} F' \frac{d\delta_j^{ic}}{dF'} dF' \tag{5.30}$$

A similar expression is obtained for the outer contacts.

Rayleigh's dissipation function

The dissipation in the lubricated contacts is described by two linear viscous dampers. One is acting normal and one tangential to the contacting surfaces. The damping coefficient of the damper operating in the normal direction is determined by a curve-fit relation derived from numerical solutions. The relation, previously presented in equation 3.48, reads:

$$C(N, L) = r(L) N^{s(L)}, \qquad C = c \frac{a v_s}{4 F_e R} \frac{\mathcal{K}}{\mathcal{E}} \tag{5.31}$$

with:

$$r(L) = 0.98 - 0.017L \tag{5.32}$$

$$s(L) = -0.83 - 0.008L \tag{5.33}$$

where R denotes the reduced radius of curvature of the contacting bodies, a half of the Hertzian contact length, v_s the sum speed and $\mathcal{K}$ and $\mathcal{E}$ the elliptical integrals of the first and second kind given by equations 3.20 and 3.21. The contribution of the inner contacts to Rayleigh's dissipation function reads:

$$\mathcal{F}_j^{ic} = \tfrac{1}{2} c^{ic} \dot{\delta}_j^{ic2} + \tfrac{1}{2} \mu_c c^{ic} \dot{\tau}_j^{ic2} \tag{5.34}$$

For the outer contacts a similar expression is valid. The quantity $\dot{\tau}$ denotes the time rate of change of the mutual approach in the direction tangential to the contacting surfaces. With the constant μ_c, the contribution of the

tangential damper can be controlled. It shows a great similarity with general friction coefficients.

For the inner contacts, we can write:

$$\dot{\tau}_j^{ic} = D_j^{ic} \dot{\alpha}_j^{ic} \tag{5.35}$$

where D denotes the instantaneous distance between the centre of the rolling element and the centre of curvature of the raceway groove (see Figure 5.8) and $\dot{\alpha}$ denotes the time rate of change of the contact angle. A similar expression is obtained for the outer contacts.

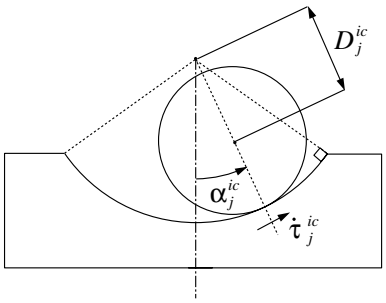

Figure 5.8: *Geometry at the inner ball-raceway contact.*

The determination of μ_c from numerical simulations requires an extension of the present EHL model. In this work μ_c is derived from measurements. The results of these measurements are discussed in Chapter 6.

5.2 The mutual approach

The kinetic, potential and dissipated energy of the inner ring, the rolling elements, the shaft and the unit consisting of the housing and the outer ring are now expressed in terms of the generalised DOF $\{p\}$. The potential and dissipated energy of the EHL contacts are expressed as a function of the quantities δ, $\dot{\delta}$ and $\dot{\tau}$. To obtain the equations of motion, these parameters have to be expressed also in terms of the generalised DOF $\{p\}$.

The parameter δ is defined as the change in distance between the centre of curvature of the raceway groove and the centre of the rolling element. Due to the complex internal geometry of a ball bearing, the determination of δ

results in complicated geometric algebra, which is not essential for understanding the essence of the present model. Hence, for a detailed derivation the reader is referred to Appendix D.

To determine the contribution of the EHL contacts to Rayleigh's dissipation function, the time rate of change $\dot{\delta}$ and $\dot{\tau}$ have to be expressed in terms of the generalised DOF. Due to the rotation of the contacts at a constant angular speed, $\dot{\delta}$ and $\dot{\tau}$ become explicitly dependent on the time coordinate. Hence, their time rate of change reads:

$$\frac{d\delta}{dt} = \{\dot{p}\}^T \frac{\partial \delta}{\partial \{p\}} + \frac{\partial \delta}{\partial t} \qquad \frac{d\tau}{dt} = \{\dot{p}\}^T \frac{\partial \tau}{\partial \{p\}} + \frac{\partial \tau}{\partial t} \tag{5.36}$$

For the calculation of the partial derivatives, it is referred to Appendix E. It can be observed that $\dot{\delta}$ and $\dot{\tau}$ are functions of both $\dot{p}$ and p. This means that (a small) part of the damping forces contributes to the stiffness matrix of the bearing.

The displacements of the outer ring are described by the analytical series of equation 4.11 and 4.12. For the calculation of the mutual approach in the outer contact, the series have to be evaluated in the centre of curvature of the outer raceway groove. This particular point is not part of the raceway (see Figure 5.9). The radial and axial displacements of the centre of curvature of

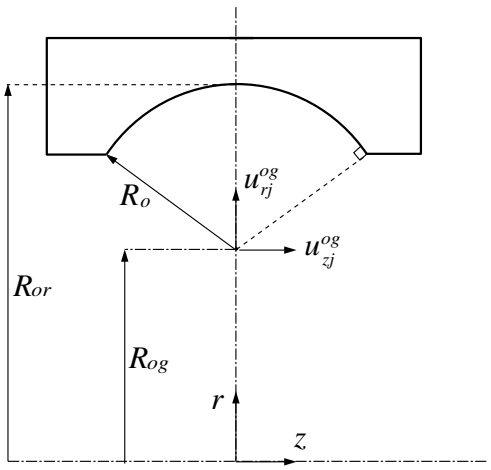

Figure 5.9: *Centre of curvature of the outer raceway groove.*

the outer raceway groove at the contact with the j^{th} rolling element, yield:

$$u_{rj}^{og} = \sum_{n=0}^{N_r}\sum_{m=0}^{M_r}\sum_{l=0}^{L_r} a_r(t)\cos(n\theta_j)\cos(m\frac{\pi}{2})\cos(l\arccos(\frac{R_{og}}{R_{or}})) + \\ + \sum_{n=1}^{N_r}\sum_{m=0}^{M_r}\sum_{l=0}^{L_r} b_r(t)\sin(n\theta_j)\cos(m\frac{\pi}{2})\cos(l\arccos(\frac{R_{og}}{R_{or}})) \quad (5.37)$$

$$u_{zj}^{og} = \sum_{n=0}^{N_z}\sum_{m=0}^{M_z}\sum_{l=0}^{L_z} a_z(t)\cos(n\theta_j)\cos(m\frac{\pi}{2})\cos(l\arccos(\frac{R_{og}}{R_{or}})) + \\ + \sum_{n=1}^{N}\sum_{m=0}^{M_z}\sum_{l=0}^{L_z} b_z(t)\sin(n\theta_j)\cos(m\frac{\pi}{2})\cos(l\arccos(\frac{R_{og}}{R_{or}})) \quad (5.38)$$

The coefficients a_r, b_r, a_z and b_z denote the time dependent contribution of the corresponding terms in the series. The parameter R_{og} is the radius of the centre of curvature of the outer raceway groove. It is observed that expressions 5.37 and 5.38 are independent of the contact angle α. This strongly simplifies the modelling of the contact between the rolling elements and the flexible outer ring.

5.3 Geometrical imperfections

The waviness imperfections on the rolling elements and on the raceways provide a time varying disturbance in the contacts. As a result excitations are generated normal to the contacting surfaces. It is obvious that the amplitude of the waviness is much smaller than the dimensions of the structural elements. Hence, waviness does not contribute to the mass and stiffness matrix of the outer ring, of the inner ring and the of rolling elements. Because the contacts are modelled as point contacts, they over-roll only one waviness track on the raceway and on the rolling elements (see Figure 5.10). To ensure harmonic excitations and to avoid aliasing effects, the waviness tracks are developed into truncated Fourier series. The waviness tracks on the inner raceway, on the outer raceway and on the rolling elements are each over-rolled with a different speed.

The inner contacts

For the disturbance W of the mutual approach at the inner contact caused by waviness on the j^{th} rolling element, the following statistical relationship

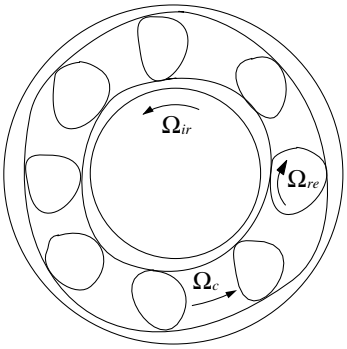

Figure 5.10: *Waviness excitation in a ball bearing.*

is valid (see also equation 2.1):

$$W_j^{re} = \sum_{n=1}^{N_b} \frac{A_j}{n^s} \cos(n\Omega_{re}t + \varphi_n) \tag{5.39}$$

The amplitude A has a Rayleigh distribution and it is defined by the parameter α (see equation 2.2). The phase φ_n is uniformly distributed over the interval $[0, 2\pi]$. The exponent s describes the amplitude decay over the subsequent wave orders. For each wave order, a new number is randomly generated for A. Each rolling element has a different waviness profile. If f_{max} is the upper bound of the frequency range of interest, then the maximum wave order N_b is given by:

$$N_b = \frac{2\pi f_{max}}{\Omega_{re}} \tag{5.40}$$

The inner contacts are also disturbed by inner ring waviness. The disturbance of the mutual approach at the contact with the j^{th} rolling element due to waviness on the inner ring reads:

$$W_j^{ir} = \sum_{n=1}^{N_i} \frac{A}{n^s} \cos(n(\theta_j - \Omega_{ir}t) + \varphi_n) \tag{5.41}$$

The amplitude A in equation 5.41 is different from the one in equation 5.39. In each contact the disturbance due to inner ring waviness is induced by the same track, but at different instants or, in other words, at different phase angles. The circumferential angle θ_j is given by equation 5.14. After

including the effect of a non-uniform ball spacing, the expression for θ_j becomes:

$$\theta_j = \Omega_c t + \frac{2\pi}{Z}(j-1) + \frac{\varepsilon}{R_p}\sin(\Omega_c t) \tag{5.42}$$

where ε is a measure for the distance between the cage centre and the centre of the inner or outer ring (see also Figure 2.12). Note that the inner ring waviness profile is over-rolled in the opposite direction. For the maximum wave order N_i, it follows:

$$N_i = \frac{2\pi f_{max}}{(\Omega_{ir} - \Omega_c)} \tag{5.43}$$

The outer contacts

For the disturbance at the outer contacts due to waviness on the rolling elements it follows

$$W_j^{re} = \sum_{n=1}^{N_b} \frac{A_j}{n^s}\cos(n(\Omega_{re}t + \pi) + \varphi_n) \tag{5.44}$$

The amplitudes A_j in equation 5.44 are the same as in equation 5.39. The only difference between the two disturbances is a phase shift equal to π radians. As a result even waves of the rolling elements do not induce a net disturbance.

The mutual approach in the outer contacts is also disturbed by outer ring waviness. The disturbance in the outer contacts due to outer ring waviness reads:

$$W_j^{or} = \sum_{n=1}^{N_o} \frac{A}{n^s}\cos(n\theta_j + \varphi_n) \tag{5.45}$$

Also for outer ring waviness the disturbance in each contact is induced by the same track. The maximum wave order N_o is given by

$$N_o = \frac{2\pi f_{max}}{\Omega_c} \tag{5.46}$$

The waviness disturbances are superimposed on the mutual approach δ in each inner and outer contact. For the calculation of the damping forces, the time rate of change of the disturbances need to be determined also. The resulting excitation force generated by waviness consists of two parts.

The first part is generated by the rotating springs and the second part is generated by the rotating dampers. Generally, the first part is dominant. However, in the case of low loads and high damping values the contribution of the second part becomes significant for high frequencies. Since these conditions frequently occur in noise-sensitive applications, the effect of the time rate of change must be included in the model.

5.4 The equations of motion

From the various energy contributions presented in the previous sections, the equations of motion can be derived. Via Lagrange's equations, the equations of motion are obtained in terms of the generalised DOF $\{p\}$. For the shaft and the bearing housings the generalised DOF represent the contribution of pre-defined component modes. Each rolling element is described by two physical DOF, one in the radial direction and one in the axial direction. The inner ring is rigidly coupled to the shaft. So in the final model, the DOF of the inner ring can be eliminated and replaced by the generalised DOF of the shaft.

The housing and the outer ring

For the unit consisting of the housing and the outer ring the equations of motion read:

$$[m^{ho}]\{\ddot{p}^{ho}\} + [c^{ho}]\{\dot{p}^{ho}\} + [k^{ho}]\{p^{ho}\} + \sum_{j=1}^{Z} F_{ej}^{oc} \frac{\partial \delta_j^{oc}}{\partial \{p^{ho}\}} + \\ + \sum_{j=1}^{Z} c^{oc} \dot{\delta}_j^{oc} \frac{\partial \dot{\delta}_j^{oc}}{\partial \{\dot{p}^{ho}\}} + \sum_{j=1}^{Z} \mu_c c^{oc} \dot{\tau}_j^{oc} \frac{\partial \dot{\tau}_j^{oc}}{\partial \{\dot{p}^{ho}\}} = \{f^{ho}\} \tag{5.47}$$

where $\{f^{ho}\}$ is the vector with the generalised external forces acting on the housing and the outer ring. The forces F_{ej}^{oc} are the elastic restoring forces in the outer EHL contacts, which can be derived from an expression similar to the one in equation 5.30. The vector $\{p^{ho}\}$ represents the contributions of the global constraint modes and the fixed interface normal modes presented in Section 4.4.

$$\{p^{ho}\}^T = \{\{a_r\}^T, \{b_r\}^T, \{a_z\}^T, \{b_z\}^T, \{p_{fx}\}^T\} \tag{5.48}$$

The contributions of the global constraint modes are denoted by the coefficients $\{a_r\}^T$, $\{b_r\}^T$, $\{a_z\}^T$ and $\{b_z\}^T$. They account for the contribution of

the analytical series presented in equation 4.11 and 4.12. The contributions of the fixed interface normal modes of the housing are denoted by $\{p_{fx}\}$. For a description of the partial derivatives in equation 5.47 the reader is referred to Appendix E.

The rolling elements

The dynamic behaviour of each rolling element is described by two translational DOF, one in the radial and the one in the axial direction:

$$\{x_j^{re}\}^T = \{\{u_{rj}^{re}\}^T, \{u_{zj}^{re}\}^T\} \tag{5.49}$$

The equation of motion for the radial DOF of the j^{th} rolling element reads:

$$\begin{aligned} m^{re}\ddot{u}_{rj}^{re} + F_{ej}^{oc}\frac{\partial\delta_j^{oc}}{\partial u_{rj}^{re}} + c^{oc}\dot{\delta}_j^{oc}\frac{\partial\dot{\delta}_j^{oc}}{\partial\dot{u}_{rj}^{re}} + \mu_c c^{oc}\dot{\tau}_j^{oc}\frac{\partial\dot{\tau}_j^{oc}}{\partial\dot{u}_{rj}^{re}} + \\ + F_{ej}^{ic}\frac{\partial\delta_j^{ic}}{\partial u_{rj}^{re}} + c^{ic}\dot{\delta}_j^{ic}\frac{\partial\dot{\delta}_j^{ic}}{\partial\dot{u}_{rj}^{re}} + \mu_c c^{ic}\dot{\tau}_j^{ic}\frac{\partial\dot{\tau}_j^{ic}}{\partial\dot{u}_{rj}^{re}} = m^{re}R_p\Omega_c^2 \end{aligned} \tag{5.50}$$

The forces F_{ej}^{ic} are the elastic restoring forces in the inner EHL contacts to be derived from equation 5.30. The equation of motion in the axial direction reads:

$$\begin{aligned} m^{re}\ddot{u}_{zj}^{re} + F_{ej}^{oc}\frac{\partial\delta_j^{oc}}{\partial u_{zj}^{re}} + c^{oc}\dot{\delta}_j^{oc}\frac{\partial\dot{\delta}_j^{oc}}{\partial\dot{u}_{zj}^{re}} + \mu_c c^{oc}\dot{\tau}_j^{oc}\frac{\partial\dot{\tau}_j^{oc}}{\partial\dot{u}_{zj}^{re}} + \\ + F_{ej}^{ic}\frac{\partial\delta_j^{ic}}{\partial u_{zj}^{re}} + c^{ic}\dot{\delta}_j^{ic}\frac{\partial\dot{\delta}_j^{ic}}{\partial\dot{u}_{zj}^{re}} + \mu_c c^{ic}\dot{\tau}_j^{ic}\frac{\partial\dot{\tau}_j^{ic}}{\partial\dot{u}_{zj}^{re}} = 0 \end{aligned} \tag{5.51}$$

where m^{re} denotes the mass of a rolling element. The right hand side vector in equation 5.50 accounts for centrifugal forces acting on the rolling elements. The partial derivatives are presented in Appendix E.

The shaft and the inner ring

At the interface between the inner ring and the shaft, the displacements and rotations of the inner ring are equal to the displacements and rotations of the shaft. Therefore, the equations of motion for the inner ring can be eliminated. The contribution of the inner ring is still accounted for in the equations of motion for the shaft. They read:

$$([m^{sh}] + [m^{ir}])\{\ddot{p}^{sh}\} + [c^{sh}]\{\dot{p}^{sh}\} + [k^{sh}]\{p^{sh}\} + \sum_{j=1}^{Z} F_{ej}^{ic}\frac{\partial\delta_j^{ic}}{\partial\{p^{sh}\}} +$$

$$+\sum_{j=1}^{Z} c^{ic}\dot{\delta}_j^{ic}\frac{\partial\dot{\delta}_j^{ic}}{\partial\{\dot{p}^{sh}\}}+\sum_{j=1}^{Z}\mu_c c^{ic}\dot{\tau}_j^{ic}\frac{\partial\dot{\tau}_j^{ic}}{\partial\{\dot{p}^{sh}\}}=\{f^{sh}\} \tag{5.52}$$

where $\{f^{sh}\}$ is the vector with the generalised external forces acting on the shaft. The vector may also account for forces due to imbalance of the shaft. The generalised DOF $\{p^{sh}\}$ represent the contribution of constraint modes and fixed interface normal modes. The constraint modes are denoted by p_x, p_y, p_z, p_ϕ and p_ψ and the fixed interface normal modes of the shaft are denoted by $\{p_{fx}\}$. Hence, the vector with generalised DOF of the shaft reads:

$$\{p^{sh}\}^T=\{p_x,p_y,p_z,p_\phi,p_\psi,\{p_{fx}\}^T\} \tag{5.53}$$

The matrix $[m^{sh}]$ is the generalised mass matrix of the shaft. The matrix $[m^{ir}]$ is a diagonal matrix, which represents the mass contribution of the inner ring to the shaft. The matrix reads:

$$[m^{ir}]=\begin{bmatrix} m^{ir} & 0 & 0 & 0 & 0\\ 0 & m^{ir} & 0 & 0 & 0\\ 0 & 0 & m^{ir} & 0 & 0\\ 0 & 0 & 0 & I_x^{ir} & 0\\ 0 & 0 & 0 & 0 & I_y^{ir}\end{bmatrix} \tag{5.54}$$

Because the inner rings are mounted on a thin shaft, the moments of inertia of the shaft and the rings can be neglected. For that reason, gyroscopic forces of the shaft and the inner rings are not accounted for.

5.5 Implementation in computer code

To make the equations of motion for the shaft, for the rolling elements, and for the housing with the outer ring suitable for implementation in computer code, they must be written in matrix notation:

$$[m]\{\ddot{p}\}+[\,c\,]\{\dot{p}\}+[\,k\,]\{p\}=\{R(t)\}-\{F(p,\dot{p},t)\} \tag{5.55}$$

The mass matrix $[m]$, the damping matrix $[c]$ and the stiffness matrix $[k]$ are constant and determined beforehand with component mode synthesis. The vector $\{F(p,\dot{p},t)\}$ accounts for the nonlinear contact forces in the bearing, which explicitly depend on time. The vector $\{R(t)\}$ contains the external forces $\{f\}$ and the centrifugal forces of the rolling elements.

To find a good initial approximation for the transient analysis, first, the static solution is solved, i.e. the displacements of the application as a result of the externally applied and centrifugal forces. The nonlinear equations are solved using Newton-Raphson iteration. As a next step, the eigenfrequencies and the normal modes of the application are calculated based on the linearised stiffness matrix that was obtained from the static solution. Finally, the nonlinear equations of motion are numerically integrated with the Newmark method, which is based on a constant-average acceleration scheme (Bathe, 1982). The nonlinear equations are solved using a modified Newton-Raphson iteration (For details, see Appendix F). Usually, before the actual time interval is calculated, the simulation is run for some time to allow transient effects to die out.

A schematic overview of the software developed for the present investigation is given in Figure 5.11. First, the individual components are modelled with the finite element method resulting in huge mass and stiffness matrices. The geometry of the components is read from the binary output files provided by the ANSYS program. In particular, the geometry of the raceway is needed to prepare the load cases for the calculation of the static and dynamic component mode sets. The dynamic mode set is calculated by solving the fixed interface eigenvalue problem in the ANSYS program using subspace iteration. The static mode set is determined with a static analysis. The mode shapes are read from the binary output files of ANSYS and stored in a component mode matrix. As a next step, the large finite element matrices are reduced with the just obtained component mode matrix. The symmetric element matrices are treated one by one to avoid the storage of the complete system matrices.

The reduced system matrices are read by the main program, which reassembles the components, using the EHL contact model, and solves the obtained equations. Other input data for the main program are the bearing geometry, given in Appendix C, the waviness tracks of the rings and the rolling elements, as defined in Chapter 2 and the operating conditions like the rotational speed of the shaft and the magnitude of the externally applied loads. The output of the main program are the generalised coordinates $\{p\}$ as a function of time. To retrieve the calculated response in terms of the original finite element DOF, the solution vector is multiplied with the component mode matrix. The obtained result can be used for vibration analyses. With the help of the original finite element models, a graphical simulation module is built, with which the time dependent behaviour can be studied.

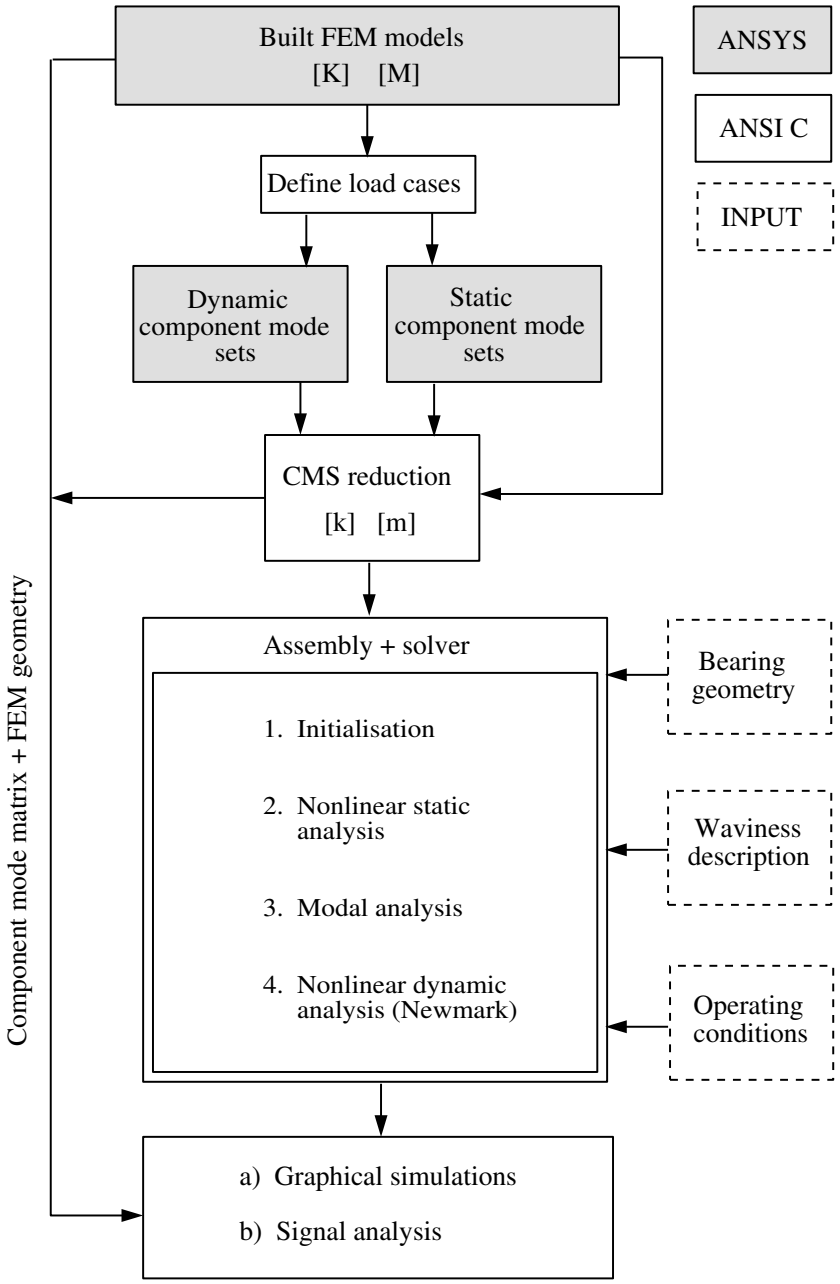

Figure 5.11: *Schematic overview of the computer software developed.*

Chapter 6

Experimental Validation of the bearing model

6.1 Vibration test spindles

After the ball bearings are assembled, their quality is tested on a vibration test spindle, to ensure silent running in the application. The test complies with the ANSI/AFBMA Standard 13-1987, an international standard, which prescribes a vibration testing method for ball bearings. The test must be performed under well defined conditions so that external influences are limited. Under such conditions, a computer simulation of the test requires only the modelling of the bearing to be tested. This makes the test very well suited for validation of our bearing model with experiments.

In the present investigation, two different spindle configurations are used. The standard test is usually performed on a spindle, which is supported by hydrodynamic bearings, rotating at a fixed angular speed. The spindle is connected to an electric motor by means of a belt tension unit as shown in Figure 6.1. The inner ring of the bearing to be tested is mounted on the rotating spindle. The spindle is designed in such a way that it represents a fixed reference frame for the central axis of the inner ring. In the standard test, the spindle rotates at 1800 rpm ($\pm 2\%$) for test bearings with an outer diameter of up to 100 mm. Due to the relatively large mass of the spindle, a constant angular speed is maintained within the required accuracy range. The outer ring of the bearing to be tested is free and subjected to a constant externally applied axial load. The load is applied by means of air pressure. To ensure freedom of motion of the outer ring in all directions, the load-

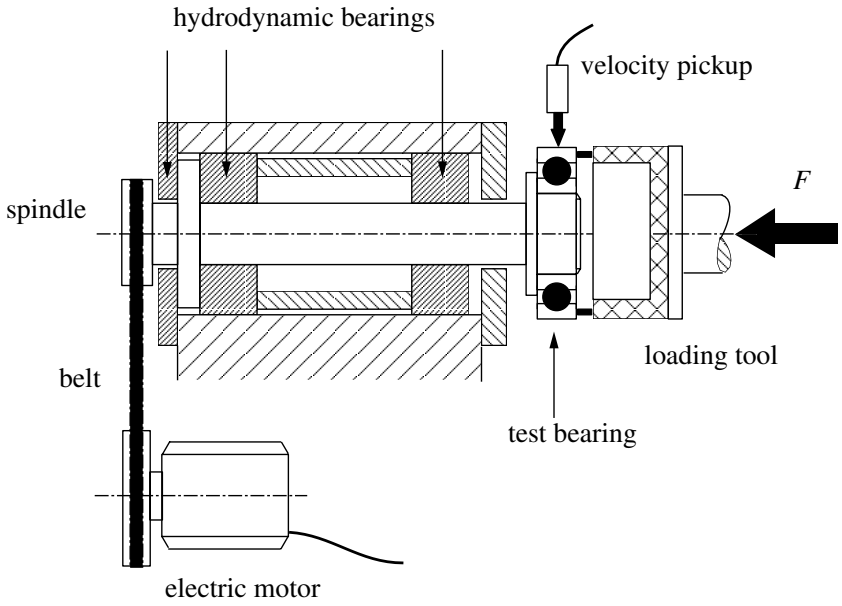

Figure 6.1: *Scheme of the hydrodynamic test spindle for standard vibration testing of ball bearings.*

ing tool is equipped with a soft rubber material. At the interface with the bearing, the rubber contains a steel ring to avoid misalignment of the test bearing.

The standard test prescribes 4 different load levels dependent on the size of the bearing to be tested. For small deep groove ball bearings the standard load is 60 N. The radial load on the bearing must be less that 1.1 N and the misalignment angle less than 3 minutes of arc. The eccentricity of the loading device should be less than 0.25 mm. The vibrations of the bearing outer ring are measured in the radial direction with a velocity pickup. According to the international standard, the vibrations are represented in terms of the root mean square (rms) velocity. Since the kinetic energy is proportional to the square of the velocity, the root mean square average of the velocity is a better measure for the energy content of the vibration signal than its peak value.

In the present research, also a high speed spindle, of which the rotational speed can be varied, was used. The maximum speed of the spindle is ap-

proximately 8500 rpm. The high speed spindle is supported by aerostatic bearings. The spindle acts at the same time as the rotor of an electric motor as shown in Figure 6.2. For the determination of the frequency response functions of the bearing, the loading tool is extended with a soft wave spring, to avoid damping effects from the rubber loading tool. The radial and axial vibrations of the bearing outer ring and the axial vibrations of the motor casing are measured with accelerometers.

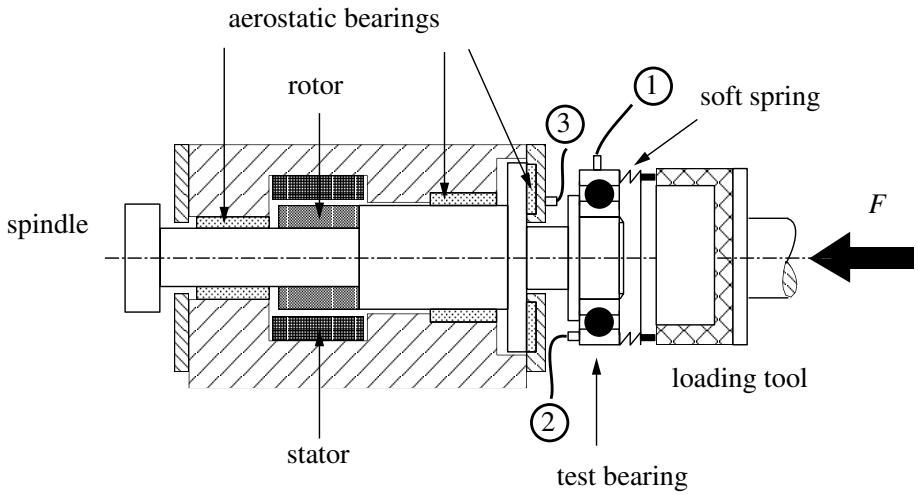

Figure 6.2: *Scheme of the high speed air test spindle for vibration testing of ball bearings.*

Usually, the quality of the bearings is quantified by the rms velocity in three different frequency bands, i.e. the low band (50-300 Hz), the medium band (300-1,800 Hz) and the high band (1,800-10,000 Hz). The question now arises of whether these velocities are indeed representative for the actual vibrational behaviour of the bearing in the application. In the low frequency band quasi-static conditions apply. Under these conditions, a clear relation between the excitation forces in the bearing and the band power exists. In the medium and high frequency band the behaviour is much more complex due to the presence of resonance frequencies. In general, resonance frequencies are determined by the properties of both the bearing and the application. In the vibration test it is assumed that the bearing is mechan-

ically decoupled from the spindle and the loading tool. Here, the resonance frequencies are solely determined by the properties of the bearing. The amplitude of vibrations with the resonance frequency is bounded by the amount of damping available. It is assumed that most of the damping is generated by the lubricant film. Therefore, it is expected that the velocities in the medium and high frequency bands be very sensitive to the properties of the lubricant, in particular its viscosity.

6.2 Description of the simulations

The bearing tested was a 6202 deep groove ball bearing. The geometrical and material properties of the bearing are presented in Appendix C. Because the inner ring is assumed to be rigidly connected to the spindle, the displacements of the inner ring are taken equal to zero. This eliminates the five equations of motion for the inner ring. The response of the bearing is usually determined on the outer ring. The bearing model, used in the numerical simulations, is shown in Figure 6.3.

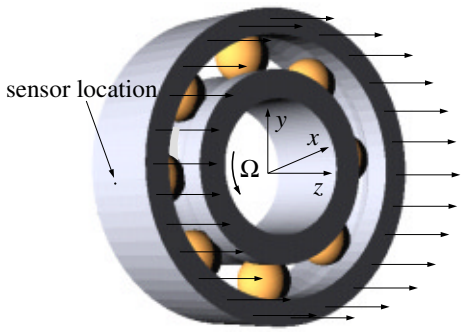

Figure 6.3: *The ball bearing model used for simulations of the vibration test.*

The outer ring of the bearing was loaded with a uniform axial load equal to 60 N. The flexibility of the outer ring is described with harmonics, of up to 16 waves per circumference. This accurately describes the first and second harmonic of the ball pass frequency. In the present investigation, the following excitation mechanisms were considered:

- variable compliance
- inner ring waviness

- outer ring waviness
- ball waviness
- cage run-out

The inner ring, the outer ring and the rolling elements all contain geometrical imperfections. In the model, account was also taken of unavoidable statistical variations of the imperfections. The non-uniform spacing of the rolling elements due to run-out of the cage was studied for both steel and plastic cages. Ball diameter variations were not considered in the present investigation. They mainly generate low frequency vibrations, which are less important in (audible) noise-related problems.

To minimise transient effects at the start of the simulation, the static solution is used as an initial condition. The static deformation field of an axially loaded ball bearing, as shown in Figure 6.4, is dominated by extensional and flexural deformations of the outer ring with 8 waves per circumference. For

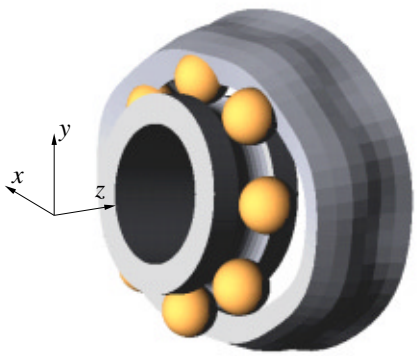

Figure 6.4: *Static deformation field of an axially loaded ball bearing with geometrical imperfections mounted on the vibration test spindle.*

clarity, the deformations are strongly exaggerated. The actual extensional deformation of the outer ring is of the order of 100 nm and the amplitude of the flexural mode is approximately 20 nm. Furthermore, it is observed that the symmetry of the statically deformed outer ring is disturbed by the presence of the geometrical imperfections.

An accurate vibration analysis of waviness requires a sufficient resolution in the frequency domain. For the investigations in the low frequency band, a resolution of 0.3 Hz was aimed at. During the simulations, a total of 30,000 time steps were calculated corresponding to 10,000 samples per second. For investigations in the medium and high frequency bands the resolution was 1 Hz. Here, a total of 200,000 time steps were calculated corresponding to 200,000 samples per second. Before the actual time signal was collected, a simulation was run for some time to allow transients effects to die out. In Figure 6.5, the instantaneous deformation field of the bearing is shown at some arbitrary point in time. For reasons of visualisation, the static deformation field of Figure 6.4 was subtracted from the actual solution.

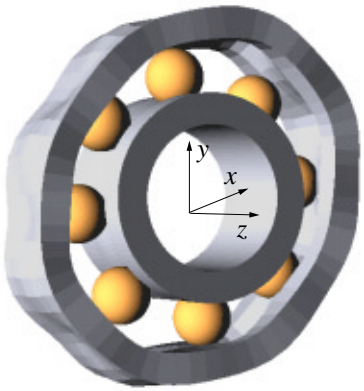

Figure 6.5: *Snapshot of the time dependent solution of a rotating ball bearing after subtraction of the static deformation field.*

The predicted radial response at the sensor location (see Figure 6.3) is plotted in Figure 6.6. To analyse the complex time signals, a Fast Fourier Transform was performed and a Hanning window was used to avoid signal leakage in the frequency domain. The loss of energy caused by the Hanning window was compensated for by multiplying the vibration signal by a factor of $\sqrt{8/3}$ in order to obtain the same moduli (de Kraker, 1992). After the Fourier transform was obtained, the spectral contributions of the displacement signal were multiplied by $\pi\sqrt{2}f$ to obtain the rms velocities. The Fourier spectrum in the low frequency band of the signal in Figure 6.6 is shown in Figure 6.7.

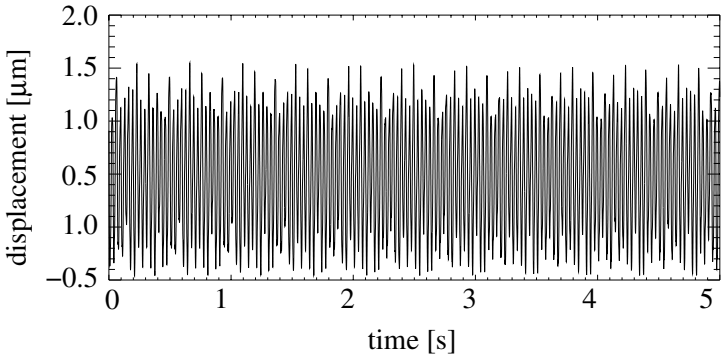

Figure 6.6: *Predicted radial displacement at the sensor location on the outer ring of a DGBB* 6202 *for* $\Omega = 1800$ *rpm.*

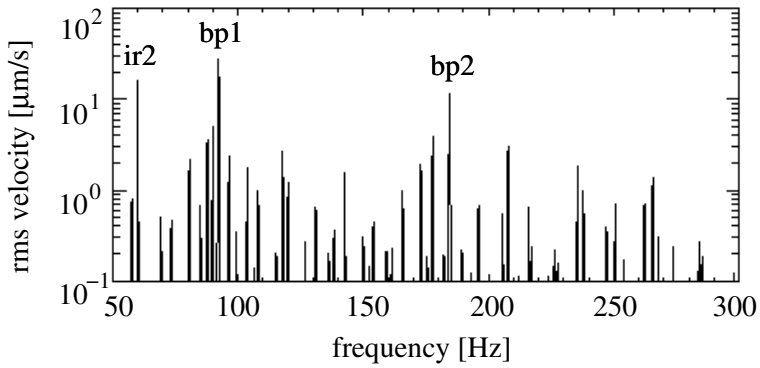

Figure 6.7: *Predicted vibration spectrum of the radial velocity on the outer ring of a DGBB* 6202 *for* $\Omega = 1800$ *rpm.*

The most important peaks in the spectrum of Figure 6.7 are the ball pass frequency (bp1) at 92 Hz, the second harmonic of the ball pass frequency (bp2) at 184 Hz and the response of the outer ring due to inner ring ovality (ir2) at 60 Hz.

6.3 The low frequency band

6.3.1 Vibration generation due to waviness

The waviness profiles for the inner and outer rings and the rolling elements are each described by Fourier series, as presented in equations 2.1 and 5.39. For the waviness imperfection W it follows that:

$$W(\theta) = \sum_{n=1}^{N_w} \frac{A}{n^s} \cos(n\theta + \varphi_n) \tag{6.1}$$

The phase angle φ_n has an arbitrary value between 0 and 2π. The parameter s describes the amplitude decay of subsequent harmonics. For vibrations generated in the low frequency band, only the first twelve waves are of importance. From surface measurements it was found that for low wavenumbers the amplitude decay of inner ring profiles is quadratic, which means $s = 2$ (see Figure 2.9). It is assumed that this also applies to the outer ring and the rolling elements.

The quantity A denotes the magnitude of the first harmonic. It has a Rayleigh distribution and is described by the stochastic property α (see equation 2.2). The magnitude A can be determined by the following relation:

$$A = \sqrt{A_c^2 + A_s^2} \tag{6.2}$$

where A_c denotes the amplitude of the cosine term and A_s the amplitude of the sine term. Both A_c and A_s have normal distributions with equal standard deviations $\sigma_c = \sigma_s = (2\alpha)^{-1}$.

When the stochastic properties of a normal distribution are known , one can calculate the number of samples required to obtain results with a certain statistical accuracy and probability. In the present investigation, the number of collected bearing samples was limited to 10. The total number of rolling elements in the case of DGBB 6202's (Z=8) was 8 x 10 = 80. It can be shown that for 10 samples, the standard deviation has an error of 31% with 95% confidence. In the present study, this applies to inner and

outer ring waviness. For 80 samples the error in the same confidence interval equals 11%. This applies to the waviness on the rolling elements.

Predictions

For all present waviness profiles, the standard deviation $\sigma_c \approx 0.5\mu$, where μ denotes the mean value of A. From surface measurements it emerged that $\mu \approx 30$ nm for the inner and outer rings. For ball waviness, μ was about five times smaller. In Figure 6.8, the predicted velocity spectrum is shown of the radial vibrations of the outer ring generated *solely* by inner ring waviness. The numbers in the figure refer to the individual wavenumbers.

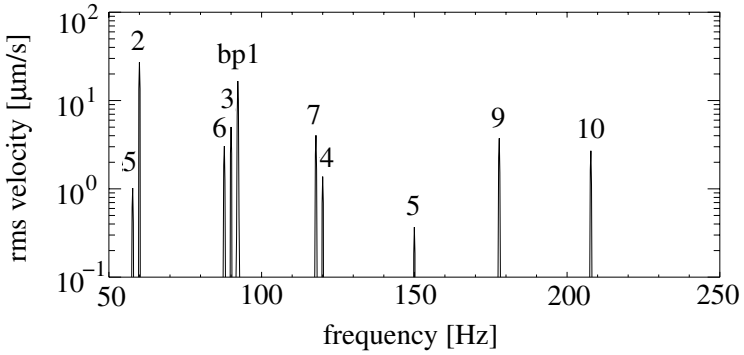

Figure 6.8: *Predicted velocity spectrum of the radial vibrations on the outer ring of a DGBB* 6202 *caused by inner ring waviness at* $\Omega = 1800$ *rpm.*

The most important peaks in the spectrum of Figure 6.8 are related to ovality n=2 at 60 Hz, n=7 at 117 Hz and n=9 at 177 Hz. The latter two peaks correspond to rigid body vibrations of the outer ring. For the complete list of spectral peaks, see Table 2.1 with $\omega = 2\pi f$.

The predicted radial vibrations of the outer ring generated by ball waviness $n = 2$ are shown in the velocity spectrum of Figure 6.9. The numbers in the figure refer to the integer k, which is associated with the mode of the vibration. The most important peaks for $k = \pm 1$ at 108 Hz and 131 Hz correspond to rigid body vibrations. Note that the frequency of the spectral peaks is independent of the number of rolling elements Z.

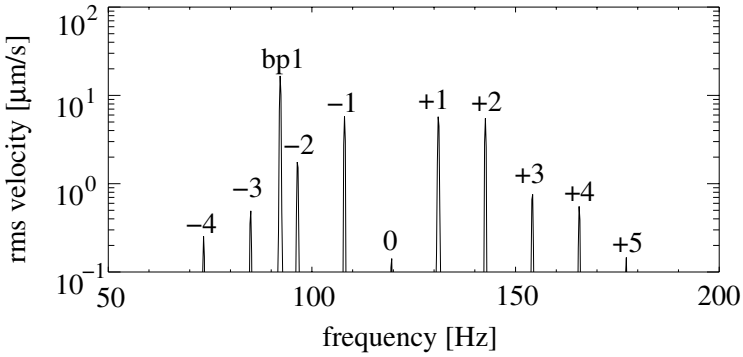

Figure 6.9: *Predicted velocity spectrum of the radial vibrations on the outer ring of a DGBB* 6202 *caused by ball waviness at* $\Omega = 1800$ *rpm.*

In general, the effect of outer ring waviness differs from the effect of inner ring and ball waviness. Because the sensor does not move relative to the outer ring, the vibrations generated by outer ring waviness are not modulated. As a result the individual wavenumbers do not generate vibrations with unique frequencies. Outer ring waviness generates vibrations with the ball pass frequency and harmonics of the ball pass frequency. In Figure 6.10 the sensor is placed at different locations along the circumference of the outer ring and the vibration amplitude is predicted at the ball pass frequency.

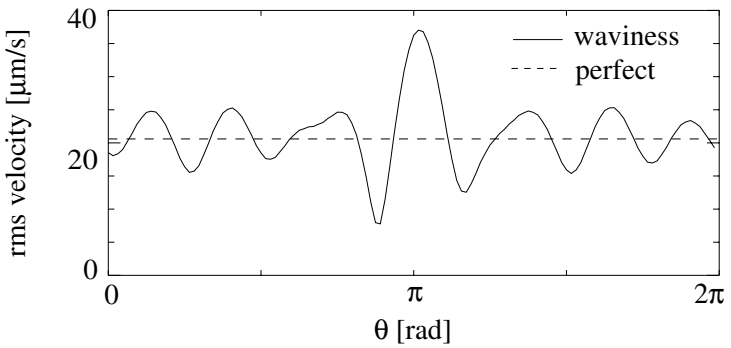

Figure 6.10: *Predicted amplitude of the ball pass frequency as a function of the circumferential position on the ring at* $\Omega = 1800$ *rpm.*

The vibration amplitude strongly varies with the circumferential coordinate on the ring. This means that the location of the sensor is critical for measuring outer ring waviness. In general, for DGBB 6202's, the low frequency band is dominated by the ball pass frequency. Hence, the velocity of the low band also depends strongly on the location of the sensor. Furthermore, for a DGBB 6202, the amplitude of the ball pass frequency strongly depends on the axial coordinate of the outer ring. This is a consequence of the static deformation field of the outer ring as a result of eight equal uniformly distributed contact forces (see Figure 4.16).

Comparison with measurements

To increase the signal-to-noise ratio in the measurements, a high pass filter is often used to suppress the dominant effect of the rotation frequency of the spindle. As a result, frequencies up to 50 Hz are distorted and, therefore, omitted in the presented results. A measured velocity spectrum in the low frequency band of the outer ring of the bearing is shown in Figure 6.11. The measured spectrum can be compared with the predicted spectrum in Figure 6.7.

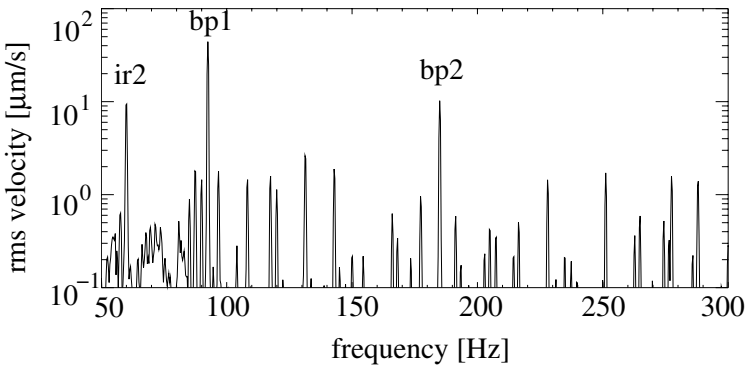

Figure 6.11: *Measured velocity spectrum of the radial velocity on the outer ring of a DGBB* 6202 *at* $\Omega = 1800$ *rpm.*

Also in the measurements the most important peaks are the ball pass frequency (bp1) at 92 Hz, the second harmonic of the ball pas frequency (bpf2) at 184 Hz and the response of the outer ring due to inner ring ovality (ir2) at 60 Hz.

To investigate the statistical variations in the frequency spectra, a batch of 10 bearings was measured and simulated. In Table 6.1, the mean value μ and the standard deviation σ of the measured and predicted spectral velocities are presented for vibrations generated by waviness on the inner ring, on the outer ring and on the rolling elements. For ball waviness, the rms velocity was calculated for all values of k (see Table 2.1).

vibration source	n	μ_{meas}	σ_{meas}	μ_{pred}	σ_{pred}
outer ring waviness	4..11	24.3	7.0	28.0	2.6
	12..19	9.6	4.7	10.5	0.7
inner ring waviness	2	15.5	8.2	14.3	6.3
	3	3.2	1.7	3.5	2.5
	4	1.0	0.6	1.0	0.5
	5	2.0	0.8	1.2	0.6
	6	2.1	1.1	2.7	1.4
	7	4.9	3.2	2.4	1.9
	9	3.4	1.6	2.7	1.2
	10	1.7	0.9	2.3	0.9
ball waviness	2	5.3	3.3	5.7	1.7
	4	4.2	1.3	2.9	0.5
low band	all	35.8	6.9	35.3	4.1

Table 6.1: *Measured and predicted spectral velocities ($\mu m/s$) in the standard vibration test due to different waviness orders n at $\Omega = 1800$ rpm.*

In the table, it can be observed that, although the imperfect surfaces are described using only a few parameters, a significant statistical agreement is obtained between measured and predicted results. The differences between the measurements and predictions are always less than the corresponding standard deviations. The statistical variations of vibrations generated by outer ring waviness are much smaller than for vibrations generated by inner ring and ball waviness. This is explained by recalling that also a perfect bearing generates vibrations at the ball pass frequency (and harmonics) as in the case of outer ring waviness.

6.3.2 Determination of cage run-out

It is assumed that the non-uniform spacing of the rolling elements can be attributed to a small run-out of the cage (see also Figure 2.12). At low

speeds, the run-out is largely determined by the clearances in the bearing. With respect to the clearance, it is important to know whether the cage is inner ring-, outer ring-, or ball-guided. All cages used in the present study are ball-guided, which means that the total clearance of the cage is determined by the clearances in the cage pockets. For the investigation on the effect of different cages, both steel and plastic cages were used.

Predictions

With the help of the numerical model, the run-out parameter ε can be determined from vibration measurements. In Figure 6.12 the predicted velocity spectrum is shown of the radial vibrations on the outer ring of a perfect bearing with a small run-out of the cage $\varepsilon = 0.1$ mm.

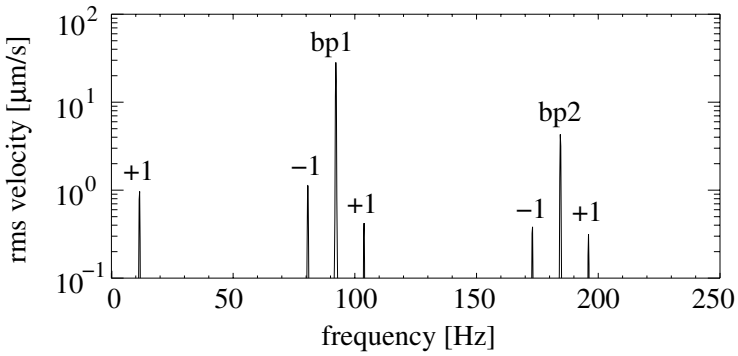

Figure 6.12: *Predicted velocity spectrum of the radial vibrations on the outer ring of a DGBB* 6202 *at* $\Omega = 1800$ *rpm, caused by a small run-out of the cage.*

The most important peaks in the spectrum are the cage frequency at 11 Hz, the ball pass frequency (bp1) plus and minus the cage frequency at 81 Hz and 103 Hz and the second harmonic of the ball pass frequency (bp2) plus and minus the cage frequency at 173 Hz and 195 Hz. The complete list of vibrations generated by cage run-out is presented in Table 2.1.

Measurements

The radial vibrations were measured on the outer rings of 20 bearings, of which 10 had plastic cages and 10 had steel cages. For each bearing, the

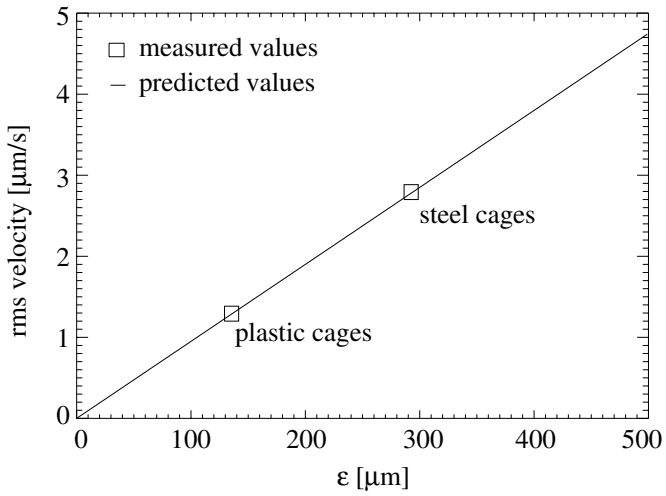

Figure 6.13: *The vibration velocity as a function of ε for a DGBB* 6202 *at* $\Omega = 1800$ *rpm.*

rms velocity was determined for the vibrations generated by cage run-out . In Table 6.2, the mean values of the velocities are presented together with the corresponding standard deviations. In the table, it can be observed that steel cages cause much higher vibration amplitudes than plastic cages. Also, the statistical variations are much higher for steel cages.

cage material	μ_{meas}	σ_{meas}
steel	2.7	2.4
plastics	1.2	0.4

Table 6.2: *The measured rms velocities on the outer ring of a DGBB* 6202 *with steel and plastic cages,* $\Omega = 1800$ *rpm.*

To determine the run-out parameter ε for the steel and plastic cages, the vibration velocity was predicted as a function of ε (see Figure 6.13). The predictions result in a linear relationship between the run-out and the vibration velocity, because for small run-outs the pre-loaded bearing behaves in a linear way.

In Figure 6.13, the measured average velocities for the steel and plastic cages are marked. It can be deduced that for steel cages the run-out must be approximately 285 μm and for plastic cages 125 μm. From the results, it can be concluded that steel cages have larger cage pocket clearances compared to plastic cages. Moreover, considering the standard deviations, it seems that the manufacturing accuracy for plastic cages is higher than for steel cages.

6.4 The natural modes of the bearing

6.4.1 Predicted natural frequencies

The lowest natural frequencies of the bearing all lie in the medium and high frequency bands. Hence, it could be expected that these frequencies show up in the vibration characteristics of the bearing in these bands. The natural frequencies and the corresponding normal mode shapes can be predicted by solving the undamped eigenvalue problem. In this eigenvalue problem, the generalised mass matrix and the stationary part of the generalised stiffness matrix must be used. In Figure 6.14, the natural frequencies and the normal mode shapes are presented for a DGBB 6202. The bearing is subjected to an externally applied axial load of 60 N. The inner ring of the bearing is fixed. The geometrical and material properties of the bearing are presented in Appendix C.

The first two normal modes are the so-called rocking or tilting modes, in which the bearing rotates out of the radial plane. In the case of a geometrically perfect bearing, both natural frequencies coincide. Due to additional deformations in the contact, which are the result of geometrical imperfections, the contact stiffness is changed. Hence, in the presence of geometrical imperfections, the natural frequencies of the rocking modes are slightly different. When the normal modes are scaled to unit length, the modal mass of the rocking modes is half the mass of the outer ring. Nevertheless, their natural frequency is very low because of the extreme low stiffness for rotations.

The third normal mode is a single one, in which the bearing oscillates in the axial direction. The modal mass is approximately equal to the mass of the outer ring. The next eight normal modes are the so-called rolling element modes. They can exist due to the low stiffness in the direction tangential to the contacting surfaces. Each individual rolling element mode has a char-

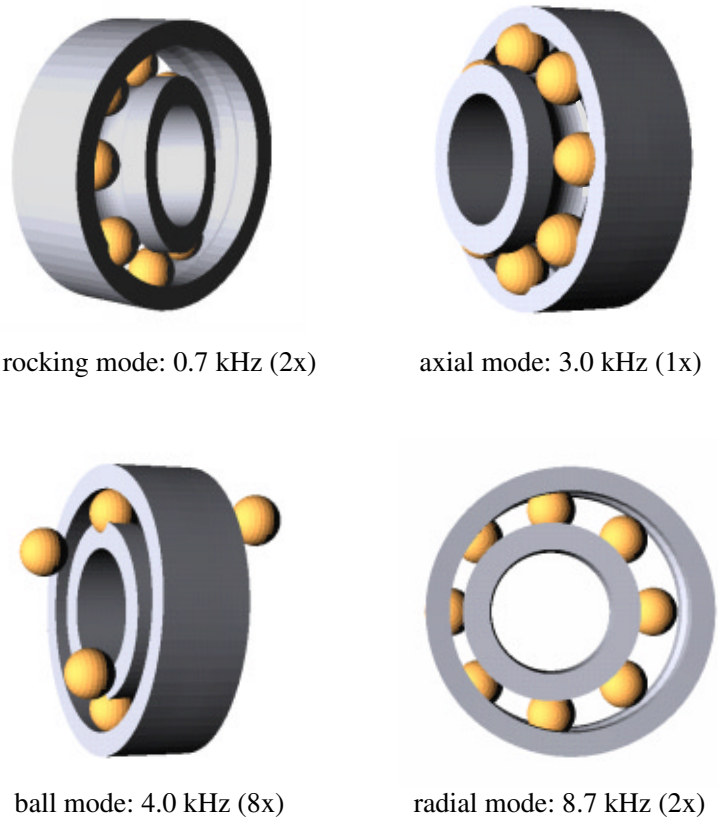

Figure 6.14: *Normal modes and natural frequencies of an axially loaded ball bearing*

acteristic pattern and the corresponding natural frequencies differ slightly in the presence of geometrical imperfections, as explained before with the rocking modes. The amplitude of the outer ring is almost zero, which indicates that these modes will be hard to detect during measurements. The last two modes just below 10 kHz are radial modes. In both modes the outer ring vibrates as a rigid body along perpendicular axes and the corresponding natural frequencies differ slightly when geometrical imperfections are present. For both modes, the modal mass approximately equals the mass of the outer ring. The first two modes just above 10 kHz are twisting and flexural modes with two waves in the circumferential direction.

The natural frequencies of the bearing depend on the externally applied axial load and the radial clearance. Both must be measured before starting a vibration measurement. In general, all the predicted natural frequencies will increase when the axial load is increased. This has to do with the Hertzian character of the contact deformations. When the radial clearance is increased, the contact angles also increase (see also Figure 1.4). As a result the natural frequency of the axial mode increases, whereas the natural frequencies of the radial, rocking and rolling element modes will decrease.

6.4.2 Measured resonance frequencies

To investigate the stiffness and damping contributions of the lubricant film, the measurements must be performed under rotating conditions. The resonance frequencies and the modal damping in a ball bearing can be determined with the help of a frequency response function. Under rotating conditions, the frequency response function of the bearing cannot be determined using classical modal analysis because the excitation spectrum in the bearing is not known.

In the present approach, the acceleration spectra of the axial and radial vibrations on the outer ring of a DGBB 6202 are measured for increasing rotational speeds. The measured spectra are collected in a matrix. The contour plot of this matrix is called a Campbell diagram. In a Campbell diagram, resonance frequencies show up as vertical bands. The width of such a band is a measure for the amount of modal damping. Excitation frequencies are characterised by straight (order) lines, which are proportional to the rotational speed of the spindle. The ratio between the excitation frequency and the spindle frequency is referred to as the excitation order. When an excitation order line intersects the vertical band of a resonance, the vibration amplitude increases. The increase is largest when the spatial distribution of the excitation matches the normal mode shape.

In Figures 6.15 and 6.16 the Campbell diagrams are shown of the axial and radial vibrations on the outer ring of a DGBB 6202. The bearing was subjected to an externally applied axial load of 60 N. The rotational speed of the spindle was varied from 2,000 to 8,000 rpm in 100 steps. The resolution of the frequency spectra is 12.5 Hz. The measurements showed a good reproducibility of the results. The most clear excitation orders in the Campbell diagram are related to ball waviness and harmonics of the ball pass frequency. The importance of ball waviness is a consequence of the

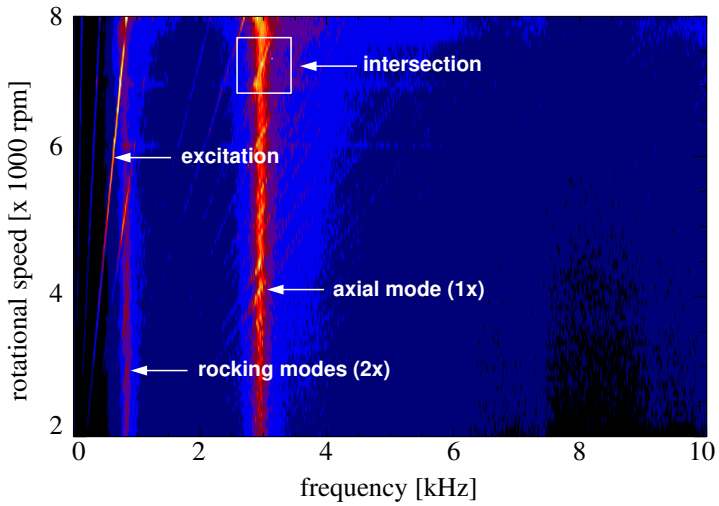

Figure 6.15: *Campbell diagram of the axial accelerations on the outer ring of a DGBB* 6202.

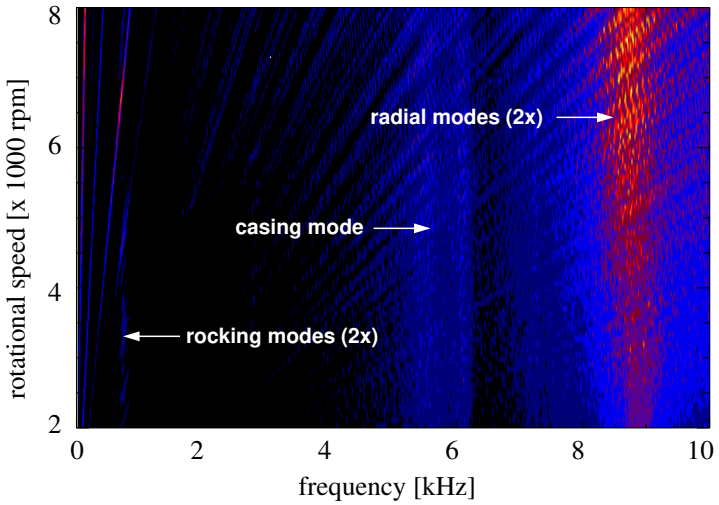

Figure 6.16: *Campbell diagram of the radial accelerations on the outer ring of a DGBB* 6202.

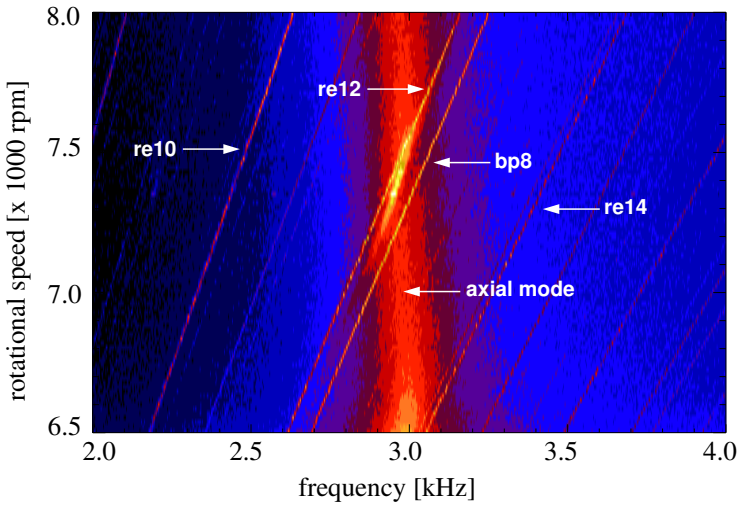

Figure 6.17: *High resolution Campbell diagram of the axial accelerations of the outer ring.*

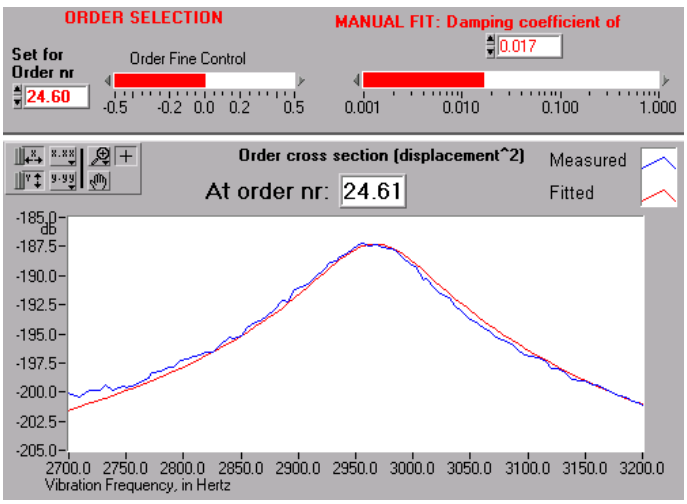

Figure 6.18: *An order line intersecting a resonance is curve-fitted with the frequency response function of a single DOF system.*

high rotational speed of the rolling elements compared to the rotational speed of the cage and the inner ring. Even wavenumbers of the order of 40 can still be observed.

In Figure 6.15, two resonance frequencies are identified at approximately 0.7 and 3.0 kHz. These resonance frequencies were predicted by the numerical model to within an accuracy of 5%. According to the simulations, the frequencies correspond to, respectively, a rocking mode and an axial mode. The modal damping is low so the frequency of the damped system is about the same as the frequency of the undamped system. The rolling element modes predicted at 4.0 kHz are not observed in the measurements. For each of these modes, the outer ring displacements are very small. Moreover, rolling element modes are heavily damped because of their low modal mass.

In Figure 6.16, a resonance is observed at approximately 8.7 kHz. In the computed results, this resonance frequency corresponds to a radial mode of the bearing. The radial mode is also predicted to within 5% accuracy. The rocking mode at 0.7 kHz is slightly visible. Furthermore, a resonance frequency is observed around 5.5 kHz. This resonance frequency is, however, not related to the bearing but to the spindle motor. This was verified by measuring the accelerations on the casing of the spindle motor in the axial direction in the absence of the bearing.

6.5 Determination of EHL contact damping

An accurate prediction of the vibration amplitudes in the medium and high frequency bands requires a reliable estimation of the damping of the natural modes of the bearing. The damping is expected to be generated by viscous losses in the EHL contacts. In Chapter 3, the EHL damping of a single contact was predicted by means of a computational model.
In the experiments on the high speed spindle, first, the dimensionless modal damping was determined for the individual bearing resonances. This was done for several lubricants. With the computer model of Chapter 5, the modal damping was "translated" to the viscous damping coefficients of the dampers in the contact model.

6.5.1 Determination of modal damping

In order to determine the frequency response functions of the bearing, order tracks, taken from the Campbell diagram, were plotted against the fre-

quency. As an example, the 8^{th} harmonic of the ball pass frequency was considered. For this purpose, the rotational speed of the spindle was varied from 6,500-8,000 rpm in 100 steps. The resolution of the frequency spectra was changed to 2.5 Hz.

A Campbell diagram of the collected frequency spectra is shown in Figure 6.17. Two excitation orders can be observed that intersect the vertical band of the axial resonance mode. The lower one with the highest excitation order corresponds to the 8^{th} harmonic of the ball pass frequency (bp8). The second excitation order, intersecting the resonance, is induced by ball waviness $n = 12$ (re12). Generally, ball waviness causes very high vibration amplitudes when the excitation frequency coincides with the resonance frequency because the spatial distribution of the excitation matches the normal mode shape.

The 8^{th} harmonic of the ball pass frequency intersects the vertical band of the axial resonance at approximately 7300 rpm. The modal damping is determined with the help of a curve-fit, based on the frequency response function of a single DOF system (see Figure 6.18). In this way, the modal damping coefficients are determined for three normal modes of the bearing (see Table 6.3). The lubricant viscosity is η_0=0.220 Pas at 40 °C. For one mode, the modal damping was determined also for η_0=0.009 Pas and η_0=0.050 Pas.

lubricant viscosity	rocking mode	axial mode	radial mode
$\eta_0 = 0.220$ Pas	4.0%	2.0%	3.0%
$\eta_0 = 0.050$ Pas	-	1.2%	-
$\eta_0 = 0.009$ Pas	-	0.7%	-

Table 6.3: *Modal damping ζ of three normal modes of an axially loaded (*60 *N) DGBB* 6202 *rotating at* $\Omega = 1800$ *rpm.*

The damping is very sensitive to certain parameters, for instance, the amount of oil injected in the bearing, that are hard to control. Nevertheless, the reproducibility of the results proved to be rather good. In the measurements it was observed that after the oil was injected, the damping decreased with time because of oil leakage. The values given in Table 6.3 were obtained after a few hours' running and it is expected that at this point in time the lubricated contacts be rather starved.

An additional uncertainty in the experiment was the temperature. In Section 3.3.4, it was shown that the damping is very sensitive to temperature variations. In the present experiment, the temperature in the bearing was not measured.

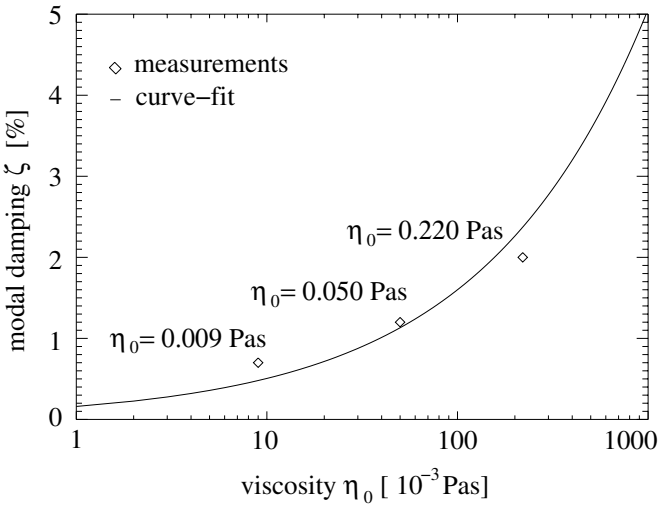

Figure 6.19: *The relation between the modal damping of the axial mode and the viscosity* η_0.

For the axial mode of vibration at 3.0 kHz, the modal damping was determined for three different values of the viscosity. The measured results are presented in Figure 6.19. Almost all theoretical models on EHL damping in the literature (Walford and Stone, 1983; Dietl, 1997) conclude that the damping is proportional to the square root of the viscosity. The same is true for the model presented in Chapter 3. This information can be used to generalise the measured results in Figure 6.19. An important conclusion that follows from the present results is that in general a large increase of the viscosity is required in order to significantly increase the damping.

6.5.2 Modal damping versus EHL contact damping

The model of a single EHL contact contains two linear viscous dampers, characterised by the parameters c and μ_c (see Section 5.1.5). With the help of numerical simulations, the values of these parameters can be determined

using the results obtained in the previous section. The measured frequency response functions (FRF's) of the bearing were fitted with predicted FRF's for given values of c and μ_c. For the determination of the FRF's of the numerical bearing model, a random excitation was applied in each modal coordinate of the bearing. Since the bearing was loaded with a pure axial force, it could be assumed that all lubricated contacts had the same operating conditions, which means that c and μ_c were equal for each contact.

The real part of the FRF of a single DOF always has a maximum at f_1 and a minimum at f_2 (see Figure 6.20). The modal damping can be determined from the real part with the following expression (Tijdeman, 1990):

$$2\zeta = \frac{\left(\frac{f_2}{f_1}\right)^2 - 1}{\left(\frac{f_2}{f_1}\right)^2 + 1} \tag{6.3}$$

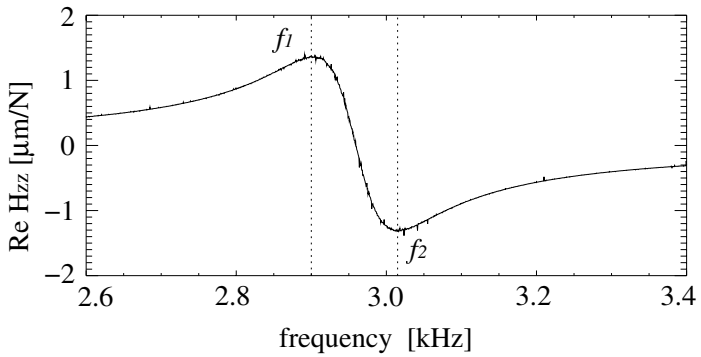

Figure 6.20: *Example of the calculated real part of the frequency response function for the axial mode of vibration, $\zeta = 2\%$.*

After curve-fitting the calculated FRF's with the measured FRF's for the rocking mode at 0.7 kHz, for the axial mode at 3.0 kHz and for the radial mode at 8.7 kHz, the following values were obtained for the viscous damping coefficients in the model:

$$c = 40\text{Ns/m} \qquad \mu_c = 0.07$$

The results are based on a lubricant viscosity equal to η_0=0.220 Pas at 40 °C. The obtained values for c are of the same order of magnitude as the ones predicted by Wijnant (1998), discussed in Chapter 3.

6.6 The medium and high frequency bands

The frequency response functions of the axially loaded ball bearing was verified successfully with experiments below 10 kHz. With this knowledge, the validity of the excitation model, as presented in section 2.3.1, was investigated for the medium and high frequency bands. It is of particular interest to investigate the validity of the assumption that the amplitudes of subsequent wavenumbers decrease with the power of 2, since this assumption greatly influences the total power of the response.

Predictions

The predicted velocity spectrum of the radial vibrations on the outer ring of an axially loaded bearing is shown in Figure 6.21. The vibration spectrum is characterised by two resonance frequencies at 3.0 kHz and 8.7 kHz. The resonance at 0.7 kHz does not show up in the radial direction because it is only marginally excited. The total power of the spectrum is largely influenced by the damping of the resonances. The damping is provided by viscous losses in the lubricant. The present lubricant viscosity equals η_0=0.1 Pas.

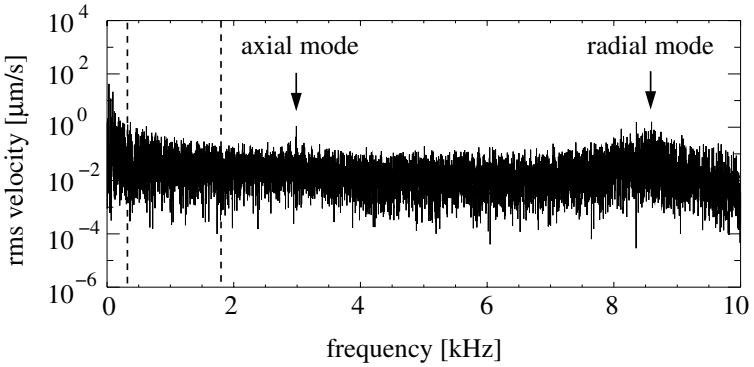

Figure 6.21: *Predicted spectral velocities in the low, medium and high frequency bands for* $\Omega = 1800$ *rpm.*

In Figure 6.22 the predicted rms velocities of the low, medium and high frequency bands are plotted as a function of the circumferential coordinate on the outer ring. It can be observed that contrary to the low frequency band, the velocities in the medium and high frequency bands hardly depend on

the circumferential coordinate. The strong dependence of the low frequency band is caused by the dominant contribution of the ball pass frequency (see also Figure 6.10).

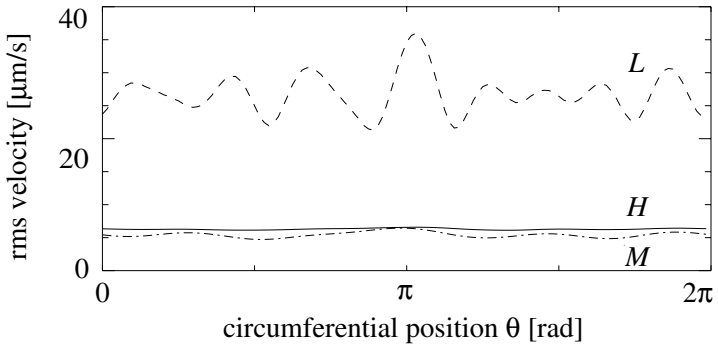

Figure 6.22: *Predicted spectral velocities in the low (L) medium (M) and high (H) frequency bands as a function of the circumferential coordinate on the outer ring of a DGBB* 6202 *rotating at* $\Omega = 1800$ *rpm.*

Comparison with measurements

In the medium frequency band it is still possible to relate the peaks in the spectrum to the individual wavenumbers of the imperfections, but it requires a sufficient resolution in the frequency domain. In the numerical study as well as in the measurements the spectral resolution is 1 Hz. In the high frequency band, the identification of the peaks has proven to be very cumbersome. In the calculations this is mainly due to period elongation (of the order of 1%), which is inherent to the Newmark time integration method.

In Table 6.4 both measured and predicted velocities are presented for the medium and high frequency bands. For the medium frequency band, the contributions from the individual bearing components were also determined.

Several explanations can be offered to explain the differences between the measured and the predicted results. First of all, the numerical model describes an idealised situation. In practice, there will always be (small) external influences from the spindle and the loading tool, which will increase the

	measured	predicted
Medium band	12.1	6.3
- Ball waviness	7.9	4.5
- Inner ring waviness	5.5	3.6
- Outer ring waviness	3.8	2.6
- Unclassified	6.3	0.0
High band	11.9	6.9

Table 6.4: *Measured and predicted rms velocities of the bearing outer ring ($\mu m/s$) for the medium and high frequency band.*

vibration level. In addition to that, small contributions can also be expected from transient effects in the bearing caused by defects and dirt. This might also explain the amount of unclassified rms velocity in the measurements. Namely, in the predictions, all the velocity could be related to the individual bearing components.

In Table 6.5, the unclassified rms velocity in the medium frequency band is subtracted from the total rms velocity. Subsequently, the relative contributions were determined for the individual bearing components.

	measured	%	predicted	%
Medium band classified	10.3	100	6.3	100
- Ball waviness	7.9	59	4.5	51
- Inner ring waviness	5.5	28	3.6	32
- Outer ring waviness	3.8	13	2.6	17

Table 6.5: *Measured and predicted contributions of the bearing components to the classified rms velocity ($\mu m/s$) in the medium frequency band.*

Although the absolute levels in the measurements are still higher, the relative contributions of the individual components are predicted quite well. It can be concluded that ball waviness contributes most to the vibrations in the medium frequency band. Also in the high frequency band it is expected that ball waviness generates most of the vibrations.

Amplitude decay of waviness harmonics

The comparison between calculated and measured results did not yet give conclusive evidence that the amplitude of waviness harmonics decreases with the power of 2. Therefore, it was investigated numerically how the rms velocity in the medium and high frequency bands changes as a function of the exponent s. The parameter was introduced by equation 2.1:

$$W(\theta) = \sum_{n=1}^{\infty} \frac{A}{n^s} \cos(n\theta + \varphi_n) \tag{6.4}$$

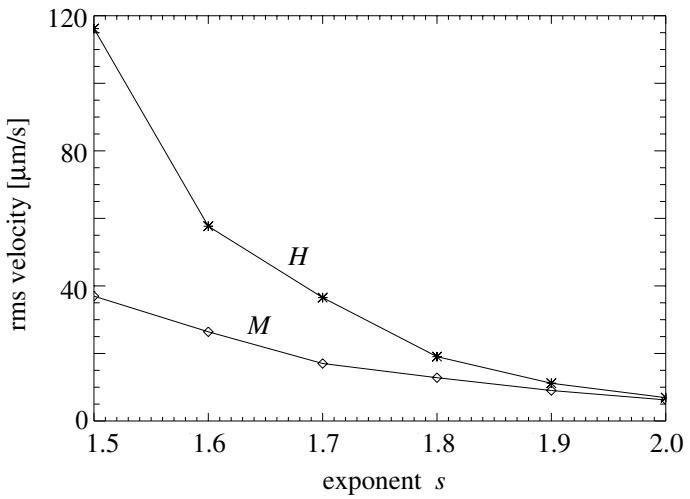

Figure 6.23: *Spectral velocities in the medium (M) and high (H) frequency bands as a function of the exponent s, describing the amplitude decay of waviness harmonics.*

It is observed that the spectral velocities in the medium and high frequency bands increase exponentially for a decreasing value of the exponent s. Therefore, it is concluded that the considered exponent must have a value of at least very close to 2 also for large wavenumbers. This is different from the surface measurements presented in Figure 2.9, since in these measurements the amplitudes of the harmonics decreased linearly for high wavenumbers. However, it has to be recalled that the present excitation model does not describe the surface imperfections themselves, but the disturbances in the contacts due to the imperfections.

6.7 Summary of validated results

The bearing model presented in the previous chapters was validated by experiments for frequencies of up to 10 kHz. The validation concerned both the frequency response functions of the bearing and the vibration generation due to waviness imperfections, parametric excitations and run-out of the cage. The bearings under consideration were 6202 deep groove ball bearings of high surface quality. The following conclusions were drawn:

- The stiffness of the outer ring and the EHL contacts is accurately described by the present approach.
- The waviness profiles are well described by a limited number of (stochastic) surface topography parameters.
- Plastic cages generate less vibrations than steel cages.
- The frequency response functions of the bearing are well described after curve-fitting of the measured damping values with the EHL contact model presented here.
- The viscosity dependence of the damping is predicted well by the present EHL damping model. The absolute damping values are less accurate.
- The excitation in the contact due to waviness approximately decrease with the power of 2 with the corresponding wavenumber.

As a next step, the bearing model can be applied to investigate the influence of the bearing on the dynamic behaviour of a complete rotor dynamic application. Ball bearings are usually an uncertain factor in the analysis of rotating applications. With the new numerical models this uncertainty is significantly reduced.

Chapter 7

Example of a rotor dynamic application

7.1 Case description

To illustrate the importance of the ball bearings on the dynamic behaviour of the application, the rotor dynamic system in Figure 7.1 was studied using the new numerical model. The system consists of a steel shaft supported by two 6202 deep groove ball bearings mounted in aluminium plummer block housings. The dimensions and the material properties of the shaft have been given in Section 4.6. The geometrical and material properties of the ball bearings are presented in Appendix C. The aluminium housings on both sides of the application are identical, except for the way in which they are connected to the outer ring of the bearing. In the one case, the outer ring forms an integral part of the housing. The unit is similar to the one in Section 4.5.3. The other housing is connected "loosely" to the outer ring, which means in this case that the outer ring is free to move in the axial direction relative to the housing (see also Figure 5.2). In the other directions the outer ring is connected to the housing by prescribing equal displacements for the outer ring and the housing at their mutual interface.

In the previous chapter the influence of geometrical imperfections on the dynamic behaviour of a single ball bearing was examined. The outer ring of the bearing considered was loaded with an externally applied axial force, which resulted in almost equal contact forces. In such a system the contribution of parametrically excited vibrations is relatively low and the response of the bearing is mainly dominated by vibrations that can be attributed to

waviness on the components. Since parametric excitation is induced by time dependent stiffness variations of the system, its contribution to the overall vibration level will be much larger when the load distribution in the bearing is asymmetrical. In the present example, a clear parametric excitation is created by applying a vertical load of 500 N at the centre of the shaft. Figure 7.1 shows the static deformation field resulting from this load. The static solution is calculated for a stationary rotating system.

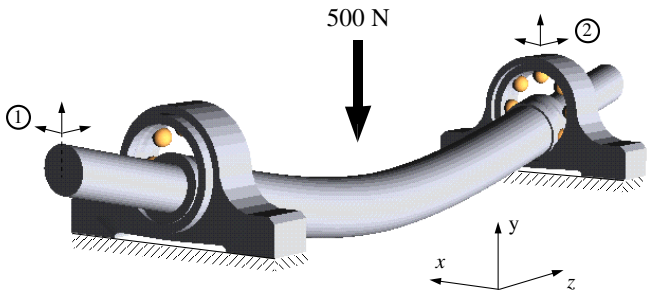

Figure 7.1: *Static deformation field of the application due to an externally applied vertical load of* 500 *N.*

Naturally, the shaft will bend as a result of the vertical load. Furthermore, large deformations will occur in the contacts between the rolling elements in the loaded zone and the raceways. In the present example, the number of rolling elements in the loaded zone is 2 or 3, depending on the circumferential position of the rolling elements (see Figure 7.2). When the bearing rotates the loaded zone will change as a function of time resulting in parametric excitations. Under the present loading conditions, the EHL stiffness model presented in Section 3.4 does not always converge. For convenience the EHL stiffness model has been replaced by the stiffness model for dry contacts.

The bearing housings are relatively stiff compared to the shaft. In the example they are fixed to a body of infinite stiffness and mass. This is modelled by placing constraints on the bottom of each housing. Figure 7.1 clearly shows the different behaviour of the two bearing housings. The outer ring which is mounted loosely in the housing moves in the axial direction due to the reaction forces in the bearing. The other outer ring, which is fixed to the housing, maintains its position. The different numbers in Figure 7.1 refer to the locations in which the response of the system will be studied.

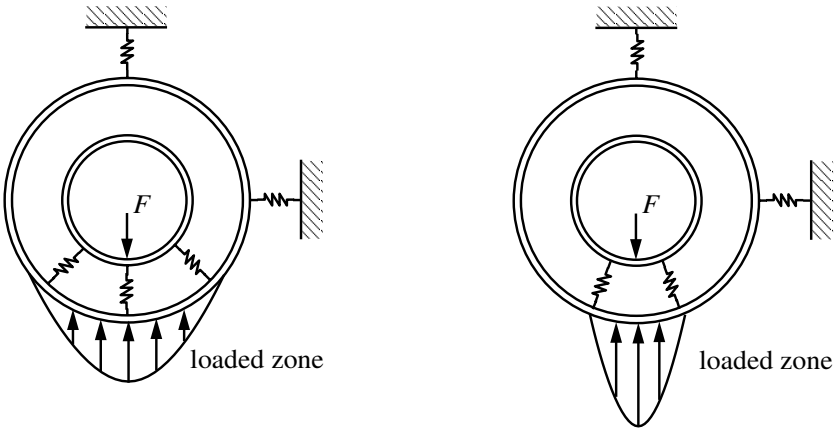

Figure 7.2: *The loaded zone is a function of the circumferential position of the rolling elements resulting in parametric excitations.*

7.2 Natural frequencies

The dynamic behaviour of the application is largely determined by its natural frequencies and its normal modes. In a linear system the undamped natural frequencies are found by solving the eigenvalue problem. In the present example this is not a straightforward matter since the stiffness matrix is nonlinear and time dependent. However, the stiffness matrix can be linearised around the static equilibrium position. Furthermore, it is justified to assume that the time variant part of the stiffness matrix is much smaller than the time invariant part.

In accordance with the philosophy of component mode synthesis, the natural frequencies and the normal modes are first calculated at the component level. For both housings and the shaft the undamped natural frequencies are given in Tables 7.1, 7.2 and 7.3.

f (Hz)	normal mode
5,529 (1x)	axial mode
8,993 (1x)	radial mode

Table 7.1: *Undamped natural frequencies of the housing with the fixed outer ring (see also Section* 4.5.3).

f (Hz)	normal mode
0 (1x)	rigid body mode
6,996 (1x)	axial mode
9,176 (1x)	radial mode

Table 7.2: *Undamped natural frequencies of the housing with the loose outer ring.*

f (Hz)	normal mode(s)
0 (5x)	rigid body modes
1,168 (2x)	bending mode n=1
2,783 (2x)	bending mode n=2
4,753 (2x)	bending mode n=3
7,207 (2x)	bending mode n=4
9,848 (1x)	extensional mode

Table 7.3: *Undamped natural frequencies of the shaft (see also Section* 4.6).

The normal modes of the housing with the loose outer ring at 6,996 Hz and 9,176 Hz are similar to the normal modes of the housing with the fixed outer ring at, respectively, 5,529 Hz and 8,993 Hz, shown in Figures 4.17 and 4.18. The shaft has 5 rigid body modes instead of six. Torsional motion is suppressed because the torsional modes are not excited by the bearings (no friction). The bending modes of the shaft are characterised by the number n, which denotes the number of waves per shaft length.

The undamped natural frequencies of the assembled system below 8 kHz are listed in Table 7.4 together with a short description of the normal modes. A number of important normal modes is shown in Figure 7.3. The total number of natural frequencies has grown significantly compared to the number of natural frequencies of the individual components.

Each ball bearing has 5 rolling elements outside the loaded zone. Due to the presence of centrifugal forces, they are all pressed against the outer raceway resulting in a small contact stiffness. Consequently, 10 normal modes are observed at 294 Hz, characterised by large rolling element displacements relative to the raceways. Because the corresponding displacements of the shaft and the housing remain small, the modes are hard to observe at the pe-

Figure 7.3: *A number of important normal modes of the application.*

f (Hz)	normal mode	f (Hz)	normal mode
216	axial shaft	2,867	y-bending shaft n=2
294	rolling elements (10x)	4,381	extensional shaft
831	x-bending shaft n=1	4,426	extensional shaft
887	y-bending shaft n=1	4,856	x-bending shaft n=3
1,215	axial outer ring	5,066	y-bending shaft n=3
1,552	θ_x-rigid shaft	5,543	axial right house
1,687	x-bending shaft n=1	6,957	axial right house
2,073	θ_y-rigid shaft	7,167	x-bending shaft n=4
2,109	y-bending shaft n=1	7,233	y-bending shaft n=4
2,806	x-bending shaft n=2	7,308	y-bending shaft n=4

Table 7.4: *Undamped natural frequencies of the assembled system.*

riphery of the application. The outer ring of the bearing, which is mounted loosely in the housing on the left hand side of Figure 7.1 has a local axial mode at 1,215 Hz. Also for this mode the displacements of the shaft and the housings are small. Hence, the mode is only observed on the outer ring itself.

The shaft has many bending modes. Some of them seem to be similar, for instance, at 831 Hz and 1,687 Hz. However, these modes can be distinguished by a different motion relative to the housings.

7.3 Parametric excitation

The application sketched in Figure 7.1 is externally loaded with a vertical force of 500 N. Due to this force the effective stiffness between the balls and the guiding rings depends on the circumferential position of the rolling elements. As a result the application is parametrically excited. In parametrically excited systems, it is always difficult to estimate the frequency content of the response in advance. This information is needed to determine the time step in the Newmark time-integration method. It was experienced that harmonics up to 50 kHz could easily be excited. Hence, in the calculations time steps were chosen equivalent to 400,000 time steps per second. A total of 100,000 time steps were calculated, which resulted in a resolution of 4 Hz in the frequency domain.

The effect of parametric excitation is studied first with geometrically perfect bearings. In the example, the outer groove radius of the bearings is chosen $R_o = 3.15$ mm and the clearance is chosen C_d=20μm. In the first example the shaft rotates at 5,000 rpm. Imbalance of the shaft is not accounted for. The damping coefficients of the viscous contact dampers in the bearings are all given by $c = 30$ Ns/m. In the flexible components material damping is modelled as proportional viscous damping. The modal damping coefficient is $\zeta_i = 0.005$ for all normal modes (see also equation 5.19). The rolling elements in the bearing on the left hand side have the same circumferential positions as the rolling elements in the bearing on the right hand side.

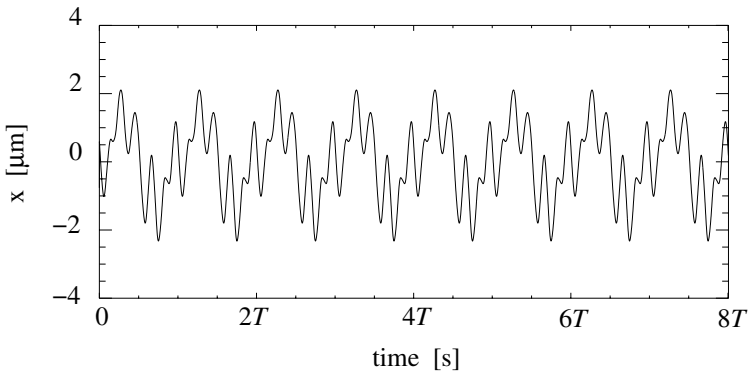

Figure 7.4: *Horizontal response of the shaft (point 1 in Figure 7.1) for* Ω*=5,000 rpm and* $T\approx 0.004s$.

The horizontal response at the end of the shaft (point 1 in Figure 7.1) is shown in Figure 7.4. The plotted response corresponds with one revolution of the bearing. Although the response looks complex, it is still periodic. The amplitudes are of the order of 2 μm. It is recalled that the total radial clearance in the bearing is 20 μm. The rms velocity spectrum of the response in Figure 7.4 is shown in Figure 7.5.

Peaks in the spectrum are found at the ball pass frequency (256 Hz) and its harmonics. The harmonics cover a wide frequency range. In particular, harmonics close to natural frequencies of the application are important. Their amplitude is bounded by the amount of damping provided both by the material damping of the components and the contact damping in the bearings. Resonances that can be observed in the spectrum of Figure 7.5

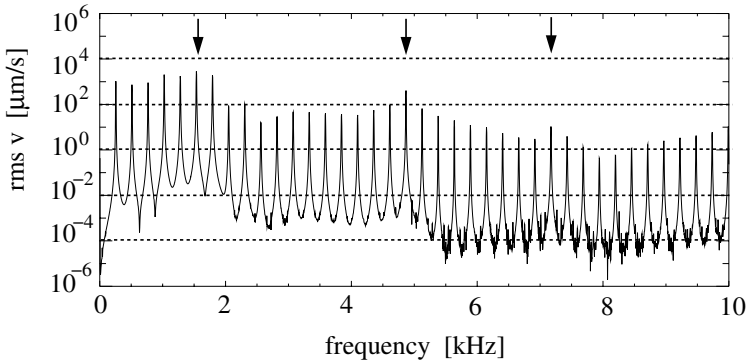

Figure 7.5: *Velocity spectrum of the horizontal vibrations of the shaft (point 1 in Figure 7.1) for* Ω=5,000 *rpm.*

are indicated by arrows. They correspond to bending modes of the shaft at, respectively, 1.7 kHz (n=1), 4.9 kHz (n=3) and 7.2 kHz (n=4).

The ball pass frequency is proportional to the shaft speed. When it is increased beyond the first natural frequency corresponding to a bending mode of the shaft (831 Hz) the character of the response can suddenly change. In Figure 7.6 the velocity spectrum is shown of the horizontal response of the shaft (point 1 in Figure 7.1) for Ω=20,000 rpm. If we look closely, it can be observed that the principal frequency of the response is no longer the ball pass frequency at 1,024 Hz, but half the ball pass frequency at 512 Hz. In other words, the solution contains a *subharmonic* component. This is an important observation, since this subharmonic component is not listed in Table 2.1 as being one of the main excitation frequencies in the bearing. The table is based on a linear bearing model (Yhland, 1992).

The system in Figure 7.1 has a vertical axis of symmetry. However, due to the rotation of the rolling elements, the response of the application is not symmetrical about the $y-$axis. The rotating contact dampers, for example, contribute to the stiffness matrix with skew-symmetric terms. The final response of the application is anti-symmetric with respect to Ω. This is illustrated by Figure 7.7, where the shaft orbit is plotted for both $\Omega = +20,000$ rpm (counter clockwise) and $\Omega = -20,000$ rpm (clockwise). The response in the figure on the left hand side is exactly the mirror image of the response in the figure on the right hand side. The amount of asymmetry in

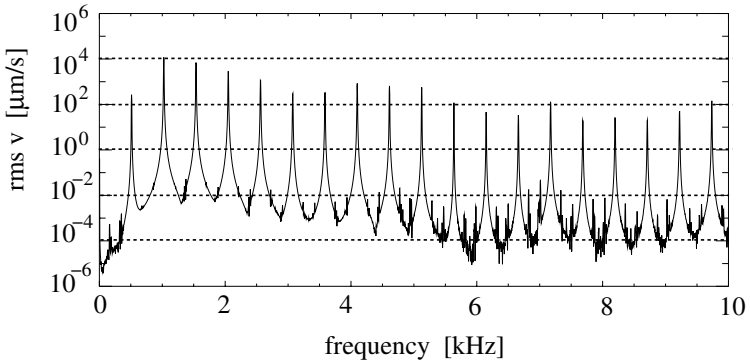

Figure 7.6: *Velocity spectrum of the horizontal vibrations of the shaft (point 1 in Figure 7.1) for* Ω=20,000 *rpm.*

the response is considerable, which indicates the significant contribution of skew-symmetric damping terms.

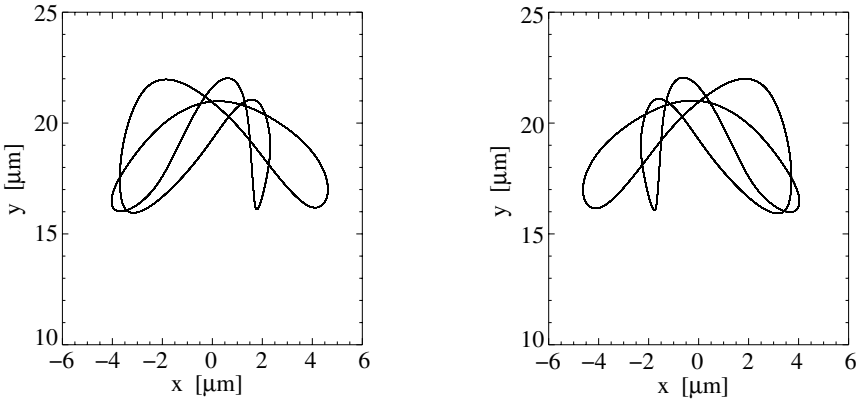

Figure 7.7: *Shaft orbits at point 1 in Figure 7.1 for* $\Omega = +20,000$ *rpm (left) and* $\Omega = -20,000$ *rpm (right).*

7.4 Geometrical imperfections

In an axially loaded ball bearing the parametrically excited vibrations are usually much smaller than the vibrations generated by geometrical imperfections, in particular waviness. In radially loaded applications the contri-

bution of parametrically excited vibrations can be much larger, as shown in the previous section. Figure 7.8 shows the velocity spectrum of the horizontal vibrations of the shaft, when geometrical imperfections in both bearings are accounted for. The same profiles are used as in Chapter 6. The waviness profiles in the bearing on the left hand side are shifted by an arbitrary number of degrees compared to the waviness profiles in the bearing on the right hand side.

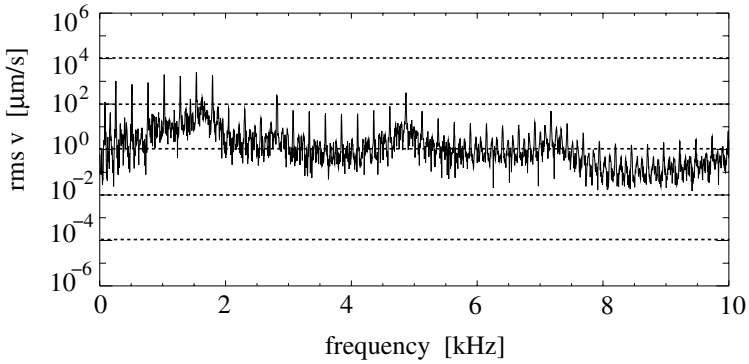

Figure 7.8: *Velocity spectrum of the horizontal vibrations of the shaft (point 1 in Figure 7.1) for* Ω=5,000 *rpm, including geometrical imperfections.*

Figure 7.8 clearly shows the resonance frequencies corresponding to bending modes of the shaft. Evidently, the vibrations generated by parametric excitation dominate the spectrum. It is recalled that the surface quality of the ball bearings is relatively high.

In Figure 7.9 the velocity spectrum is shown for the axial vibrations of the housing with the fixed outer ring. One resonance frequency can be observed at 5.5 kHz. Also, on the housing the vibrations generated by parametric excitation are the dominant ones. Because the stiffness of the housings is much higher than the stiffness of the shaft and the ball bearings, the vibration level of the housings is significantly smaller than the vibration level of the shaft.

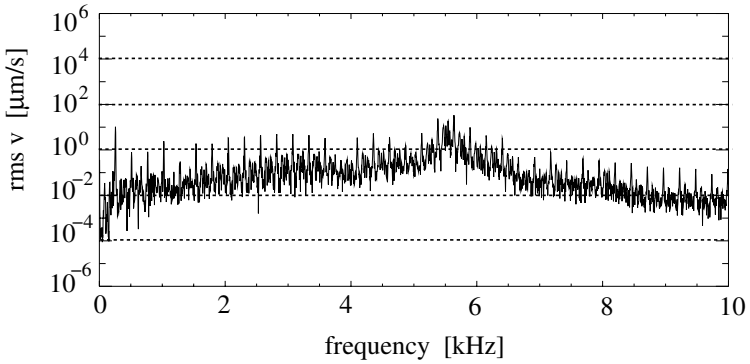

Figure 7.9: *Velocity spectrum of the axial vibrations on the housing (point 2 in Figure 7.1) for* Ω=5,000 *rpm, including geometrical imperfections.*

7.5 Reduction of parametric excitation

7.5.1 Changing the radial clearance

The radial clearance largely influences the parametric excitation in the bearing. When the clearance is reduced, the number of rolling elements in the loaded zone will increase (see also Figure 2.4), resulting in smaller stiffness variations. In the present example, the radial clearance is decreased from 20 μm down to 5 μm. In the new design, the number of rolling elements in the loaded zone is 4 or 5. The velocity spectra of the horizontal vibrations of the shaft and the axial vibrations of the housing are shown in Figures 7.10 and 7.11.

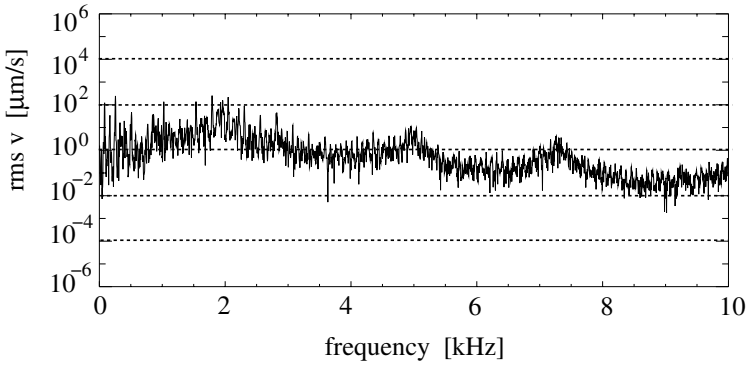

Figure 7.10: *Velocity spectrum of the horizontal vibrations of the shaft (point 1 in Figure 7.1) for* Ω=5,000 *rpm with* $C_d = 5\mu m$.

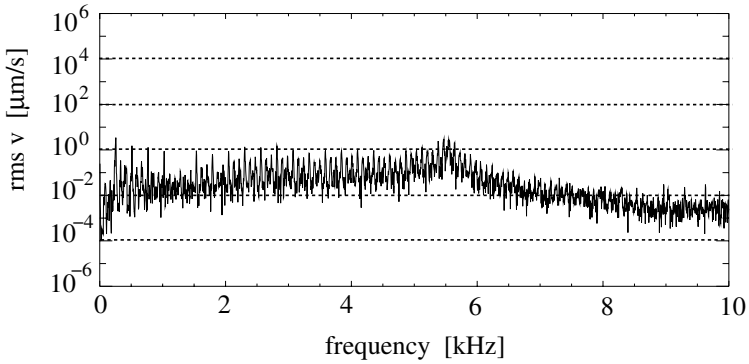

Figure 7.11: *Velocity spectrum of the axial vibrations on the housing (point 2 in Figure 7.1) for* Ω=5,000 *rpm with* $C_d = 5\mu m$.

In both spectra it can be observed that the level of the parametrically excited vibrations have decreased significantly compared to the levels in Figures 7.8 and 7.9, respectively. At low frequencies the vibrations of the housing are still dominated by parametric excitation. At higher frequencies geometrical imperfections have become the most important vibration source, in particular imperfections of the balls.

7.5.2 Introduction of an axial preload

When ball bearings with a smaller clearance are not available, an axial preload can be used to decrease the level of the parametrically excited vibrations. In the present example, an axial preload is applied on the outer ring which is mounted loosely in the housing. The load is directed outwards, as shown in Figure 7.12.

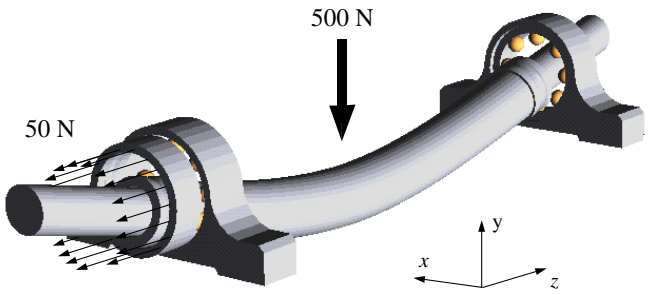

Figure 7.12: *Static deformation field of the application due to an externally applied vertical load of* 500 *N and an axial preload of* 50 *N.*

The velocity spectra of the horizontal vibrations of the shaft and the axial vibrations of the housing are shown in Figures 7.13 and 7.14.

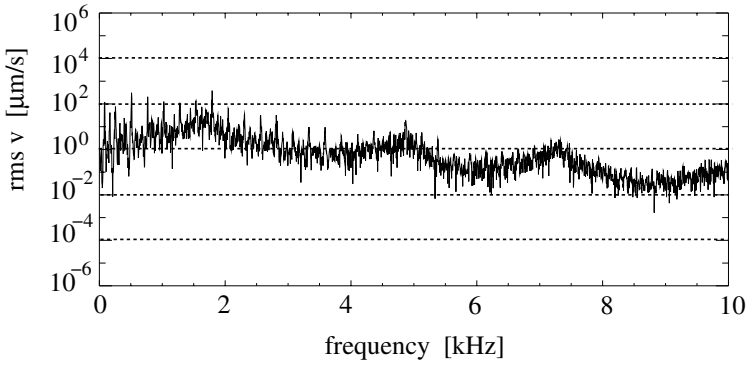

Figure 7.13: *Velocity spectrum of the horizontal vibrations of the shaft (point 1 in Figure 7.1) for* Ω=5,000 *rpm, after applying an axial preload of* $50N$.

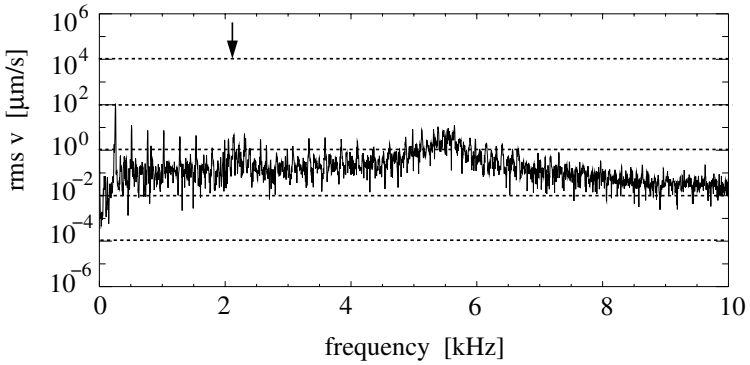

Figure 7.14: *Velocity spectrum of the axial vibrations on the housing (point 2 in Figure 7.1) for* Ω=5,000 *rpm, after applying an axial preload of* $50N$.

Also here, it can be observed that in both spectra the levels of the vibrations generated by parametric excitation are reduced compared to the levels in Figures 7.8 and 7.9. As a consequence of the preload the natural frequencies and the normal mode shapes of the application have changed to some extent. In the spectrum in Figure 7.14 an additional resonance can be observed at approximately 2 kHz (see arrow). Here, the bending mode of the shaft with $n = 1$ has a strong interaction with the housing via the ball bearing. The

resonance increases the vibration level of the housing. However, the overall level is still lower than the vibration level of the shaft.

7.6 Summary of results

A ball bearing application loaded with a pure radial load may be subject to severe parametric excitation. In that case the resulting response of the application is highly dependent on the material damping of the flexible components and the viscous losses in the lubricant. Above the first natural frequency corresponding to a bending mode of the shaft, the response may also contain subharmonic components, which would not have been predicted by a linear model.

With numerical simulations two ways were shown to suppress parametric excitation in ball bearings. One way was to reduce the radial clearance and the other way was to apply an axial preload. An overview of the rms velocities in the low (50 Hz - 300 Hz), medium (300 Hz - 1,800 Hz) and high (1,800 Hz - 10,000 Hz) frequency bands for the cases calculated in this chapter is given in Tables 7.5 and 7.6.

frequency band	waviness (Fig. 7.8)	clearance (Fig. 7.10)	preload (Fig. 7.13)
L	682	508	191
M	5,445	446	840
H	1,277	347	190
Σ	5,634	760	881

Table 7.5: *The rms velocities ($\mu m/s$) of the horizontal vibrations of the shaft.*

frequency band	waviness (Fig. 7.9)	clearance (Fig. 7.11)	preload (Fig. 7.14)
L	80	14	55
M	5	3	22
H	13	5	136
Σ	81	15	148

Table 7.6: *The rms velocities ($\mu m/s$) of the axial vibrations of the housing.*

In the simulations, a reduction of the radial clearance appeared to be the most effective way to reduce the vibration level in the considered application. An axial preload load could also be applied, although it increased the overall vibration level of the housing.

The present numerical study has shown that the new simulation tool can provide the engineer with useful (quantitative) guidelines that can help him to solve real noise and vibration related problems in rotor dynamic applications with ball bearings.

Chapter 8

Conclusions

Component mode synthesis (CMS) is a very efficient method for modelling the dynamic behaviour of flexible machine components. In this work the method was successfully applied to an application with ball bearings. To deal with the rotating contact loads on the raceway of a flexible outer ring, a new method had to be developed. In this new CMS technique, the displacements of the outer raceway are written as combinations of Fourier series and Chebyshev polynomials. The method has proven to be very fast and accurate and it can be applied to general moving load problems in all kinds of engineering applications.

An advantage of the present approach is the possibility to treat the lubricated contacts between the guiding rings and the rolling elements as individual massless components. Here, their stiffness and damping behaviour was described at the component level first with advanced time dependent contact calculations. These computations were done in a parallel project.

With the help of the new CMS method it was found that the outer ring of a 6202 deep groove ball bearing deforms significantly in real applications as a result of the time varying contact forces caused by the geometrical imperfections on the rotating components in the bearing. The geometrical imperfections are well described by a small number of stochastic surface topography parameters that can be measured relatively easy. This was applied to the bearing model and good agreement was obtained with measurements. Moreover, it was shown with the help of measurements that for small deep groove ball bearings of high quality the amplitude of waviness harmonics approximately decreases by a power of 2. Although the imperfections on

the rolling elements are usually much smaller than the imperfections on the inner and outer ring, they proved to be one of the most important sources of vibration in the bearing. This is a direct consequence of their high rotational speed compared to the rotational speeds of the cage and the inner ring.

A comparison between measured and predicted frequency response functions of the bearing showed that the stiffness in a ball bearing is well described by the present model. With respect to the damping it was concluded that the dissipation in a lubricated contact cannot be described by one single damper. At least two dampers are required in each contact to damp all principal resonances in the bearing. An important parameter that greatly influences the damping of the resonances in the bearing, is the viscosity of the lubricant used. Both predictions and measurements showed that the viscosity must be increased considerably in order to obtain a higher damping value. With respect to the absolute damping values, the damping model appeared to be less consistent with the measurements. The model predicted too low values, even without the inclusion of starvation effects. A possible reason for this discrepancy might be the frequency dependence of the damping. This was confirmed by line contact calculations at SKF.

Also, the cage may act as an additional damping source in the bearing but this was beyond the scope of the present work. The influence of the cage on the dynamic behaviour of the bearing seems to be small since the predictions based on the present "cageless" model correlated well with the measurements. The main dynamic effect induced by the cage concerns the generation of vibrations due to a small run-out. In this respect the plastic cages performed better than the steel ones.

Acknowledgement

This research is part of a long term cooperation between the Applied Mechanics group and the Tribology group at the University of Twente and the SKF Engineering & Research Centre BV in Nieuwegein. During the last 4 years of research I was employed at the University, but I was fortunate to carry out my work at SKF. Hence, I am indebted to a lot of people in both organisations that have supported and contributed to my work.

Especially, I would like to thank Henk Tijdeman, Peter van der Hoogt and Ruud Spiering from the Applied Mechanics group at the University and my mentor Gerrit van Nijen from the Noise and Vibration Team at SKF ERC for their valuable contributions and continuous support during my research work.

Thanks also to the other members of the Noise and Vibration Team at SKF ERC for their great support and interest. The noise and vibration team consists of Teun Zandbergen, Henk Mol, Rob Hendrikx, Paul Dietl, John Eriksson and former members Anton Keim and Harald Elshof. For me, these people have largely contributed to the pleasant time I have had at SKF ERC. From SKF, I also thank Stathis Ioannides, Jan Duits, Piet Lugt, John Tripp, and Yannick Fierling for their encouraging support. Finaly, I thank the Manager Director of SKF ERC for his kind permission to publish this work and for using foto material of SKF.

Parallel to this one, a similar PhD project on elastohydrodynamic lubrication was carried out in cooperation with the Tribology group at the University. From this group, I would like to thank Ysbrand Wijnant, Cees Venner and Wijtze ten Napel for the valuable discussions, input and support. Also, I thank the many students that have contributed to my work and to related topics. In particular I would like to thank Jonathan Tripp for the vibration measurements he performed.

Furthermore, I am indebted to Debbie Vrieze and Annemarie Teunissen for their fantastic administrative support, which has greatly simplified the communication between SKF and the University. Also, I would like to thank Katrina Emmett for her valuable suggestions concerning the English language.

Finally, I would like to thank all my family and friends. I consider their unconditional love, support and endurance as being the most important factor in completing this work. On many occasions I was amazed because their confidence seemed to be even higher than my own. Thank you Saskia, Anton, Betsie, Maurice, Nel, Johan and Jan Willem!

Utrecht, November 1998

Nomenclature

Roman scalars

A	magnitude of the first waviness harmonic
A_c	amplitude of cosine term of first waviness harmonic
A_{or}	cross-sectional area of the outer ring
A_s	amplitude of sine term of first waviness harmonic
a	half of the Hertzian contact length
b	half of the Hertzian contact width
C	dimensionless damping
C_d	radial clearance
c	damping coefficient
c_k	coefficients
D	distance between ball centre and groove centre
D_0	initial distance between ball centre and groove centre for $\delta = 0$
D_r	radial distance between ball centre and groove centre
D_z	axial distance between ball centre and groove centre
d, d_1, d_2	elastic contact deformations
E, E_1, E_2	moduli of elasticity
E'	reduced modulus of elasticity
F, F_i	force
F_b	interface load
F_d	dissipative force
F_e	elastic restoring force
f_1, f_2	natural frequencies
f_i	inner osculation
f_{max}	upper bound frequency range of interest
f_o	outer osculation
$H(\delta)$	Heaviside step function
H_0	dimensionless film thickness or gap width at $x = 0$ and $y = 0$

$H(\delta)$	Heaviside step function
h	film thickness or gap width
h_0	film thickness or gap width at $x = 0$ and $y = 0$
I_{or}	area moment of inertia of the cross-sectional area
k, q	integers
k_1	horizontal housing stiffness
k_2	vertical housing stiffness
k_f	thermal conductivity
L	dimensionless parameter
L_r, M_r, N_r	number of terms in series for u_r^{or}
L_z, M_z, N_z	number of terms in series for u_z^{or}
M	dimensionless parameter
M_b	interface moment
m	mass
N	dimensionless parameter
N_b	maximum wave number ball waviness
N_e	number of nodal degrees of freedom
N_i	maximum wave number inner ring waviness
N_o	maximum wave number outer ring waviness
n	wave number
n_k	number of kept normal modes
P	point load
p	hydrostatic pressure
$p(x, \alpha)$	Rayleigh distribution
R	reduced radius of curvature
R_1, R_2	radii of curvature
R_{1x}, R_{2x}	radii of curvature in x-direction
R_{1y}, R_{2y}	radii of curvature in y-direction
R_{ig}	radius centre of curvature of inner groove
R_{og}	radius centre of curvature of outer groove
R_{or}	bottom radius outer raceway
R_x	reduced radius of curvature in x-direction
R_y	reduced radius of curvature in y-direction
r, θ, z	cylindrical coordinates
s	exponent amplitude decay waviness
T	temperature (Chapter 3)
T	kinetic energy (Chapter 5)
T_0	room temperature
T_n	Chebyshev polynomial of degree n
t	time

u_t	tangential interface degree of freedom
u_i	displacement
u_x, u_y, u_z	displacements in Cartesian coordinate frame
u_r	radial displacement
u_z	axial displacement
V	potential energy
v_1, v_2	surface velocities
v_{ir}	surface velocity inner ring
v_{or}	surface velocity outer ring
v_{re}	surface velocity rolling element
v_s	sum speed
v_{max}	maximum spectral peak velocity
v_{rms}	root mean square velocity
w	deformation
w_0	deformation at $x = 0$ and $y = 0$
W	waviness imperfection
X, Y	stochastic variables
x, y, z	Cartesian coordinates
x_b	translational interface degree of freedom
Z	number of rolling elements
Z_{or}	half-width of the outer raceway

Greek scalars

α	contact angle
α_p	pressure-viscosity coefficient
γ	temperature-viscosity coefficient
Δ	dimensionless mutual approach
δ	mutual approach between contacting bodies
ϵ	ellipticity ratio Hertzian contact (b/a)
$\epsilon_i, \epsilon_1, \epsilon_2$	errors
ε	eccentricity of the cage
ζ	modal damping
η	viscosity
η_0	nominal viscosity
κ	Hertzian stiffness coefficient
Λ	dimensionless frequency
λ	ratio between radii of curvature (R_x/R_y)
μ	mean value
μ_c	constant for tangential damper

ν, ν_1, ν_2	Poisson's ratios
ρ	density
ϕ, ψ, θ	Bryant angles
φ	phase angle
φ_b	rotational interface degree of freedom
ω	angular frequency
ω_i	i^{th} angular frequency
ω_n	natural angular frequency
Ω	rotational speed shaft
Ω_c	rotational speed of the cage
Ω_{ir}	rotational speed of the inner ring
Ω_{re}	rotational speed of the rolling elements
Ω_s	spin velocity
σ_x, σ_y	standard deviations
τ	tangential approach between contacting bodies

Other scalars

$\mathcal{E}$	ellipticity integral of the second kind
$\mathcal{K}$	ellipticity integral of the first kind
$\mathcal{F}$	Rayleigh's dissipation function

Roman vectors

$\{a_r\}, \{b_r\}$	vectors with contributions of the series for u_r^{or}
$\{a_z\}, \{b_z\}$	vectors with contributions of the series for u_z^{or}
$\{c\}$	vector with modal viscous damping coefficients
$\{e_x\}, \{e_y\}, \{e_z\}$	unit vectors along $x-$, $y-$ and z-axes
$\{F\}$	vector with external forces
$\{f\}$	vector with generalised external forces
$\{F_b\}$	vector with interface loads
$\{m\}$	vector with modal masses
$\{p\}$	vector with generalised degrees of freedom
$\{p_b\}$	vector with generalised interface degrees of freedom
$\{p_{fx}\}$	vector with contributions of fixed interface normal modes
$\{R\}$	right hand side vector
$\{\hat{R}\}$	residual vector of dynamic force balance
$\{x\}$	vector with nodal degrees of freedom
$\{x_b\}$	vector with nodal interface degrees of freedom

$\{x_i\}$	complement of $\{x_b\}$

Greek vectors

$\{\zeta\}$	vector with dimensionless modal damping coefficients
$\{\lambda\}$	vector with natural angular frequencies
$\{\omega\}$	angular velocity vector

Roman matrices

$[C]$	damping matrix
$[c]$	generalised damping matrix
$[\tilde{c}]$	linearised damping matrix
$[c_d]$	diagonal modal viscous damping matrix
$[G]$	flexibility matrix
$[G^a]$	residual flexibility matrix
$[H]$	frequency response matrix
$[I]$	mass moments of inertia matrix
$[K]$	stiffness matrix
$[k]$	generalised stiffness matrix
$[\tilde{k}]$	linearised stiffness matrix
$[\hat{k}]$	tangent matrix Newmark
$[M]$	mass matrix
$[m]$	generalised mass matrix
$[MAC]$	modal assurance criteria matrix
$[O]$	orthogonality matrix
$[R_\theta]$	elementary rotation matrix about z-axis
$[R_\psi]$	elementary rotation matrix about y-axis
$[XO]$	cross-orthogonality matrix

Greek matrices

$[\Lambda_k]$	diagonal matrix with kept eigenvalues λ_k^2
$[\Psi]$	matrix with column-wise stored shape functions
$[\Phi]$	matrix with column-wise stored normal modes

super-/subscripts

ho	referring to the housing/outer ring

ic	referring to the inner contacts
ig	referring to the centre of curvature of the inner groove
ir	referring to the inner ring
j	referring to rolling element number
meas	measured values
oc	referring to the outer contacts
og	referring to the centre of curvature of the outer groove
or	referring to outer raceway
pred	predicted values
re	referring to the rolling elements
sh	referring to the shaft

abbreviations

CMS	component mode synthesis
DGBB	deep groove ball bearing
DOF	degrees of freedom
EHL	elasto-hydrodynamic lubrication
FEM	finite element method
MAC	modal assurance criteria
TAM	test analysis model

Appendix A

Analytical solution for a flexible ring

The analytical solution of the extensional and flexural deformations of a rectangular ring loaded with Z equal uniformly distributed loads in the radial plane (see Figure A.1) was derived by Yhland in an internal SKF report (1965).

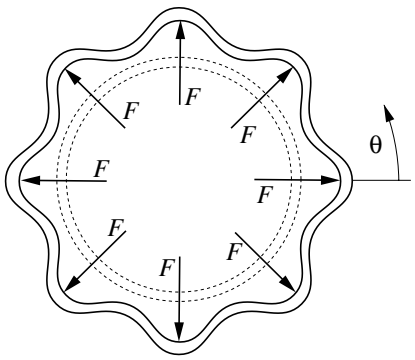

Figure A.1: *Deformations of the outer ring due to eight uniformly distributed contact loads.*

The problem is solved using *Castigliano's theorem* (Timoshenko, 1955) by taking into account the elastic energy V contributed by the bending moment

and by the longitudinal force. Castigliano's theorem states that:

$$\frac{\partial V}{\partial F_i} = u_i \quad i = 1...Z \tag{A.1}$$

In other words, if the strain energy V of an elastic body can be expressed as a function of the loads F_i, then the partial derivative of the strain energy, with respect to a particular load, gives the corresponding displacement at the point of application of that particular load in the direction of that load.

For the radial displacements of the outer ring as a function of the circumferential position, it can be derived:

$$u_r(\theta) = \frac{FZR_{or}}{2\pi EA_{or}} + \frac{FZR_{or}^3}{\pi EI_{or}} \sum_{q=1}^{\infty} \frac{1}{\left((qZ)^2 - 1\right)^2} \cos(qZ\theta) \tag{A.2}$$

The first term on the right hand side accounts for extensional deformations of the ring and the second term for flexural deformations. The parameter R_{or} denotes the centre radius of the outer ring and I_{or} the area moment of inertia of the cross section area A_{or}. The analytical solution is used in the present work to validate the results of the two-dimensional model presented in equation 4.14.

Appendix B

Evaluation of series

B.1 Chebyshev polynomials

A Chebyshev polynomial of degree n, denoted as $T_n(x)$, is given by

$$\begin{aligned} T_0(x) &= 1 \\ T_1(x) &= x \\ T_n(x) &= 2xT_{n-1}(x) - T_{n-2}(x) \;\; n \geq 2 \end{aligned} \tag{B.1}$$

The first four terms of a Chebyshev polynomial are plotted in Figure B.1 for the interval [-1,1].

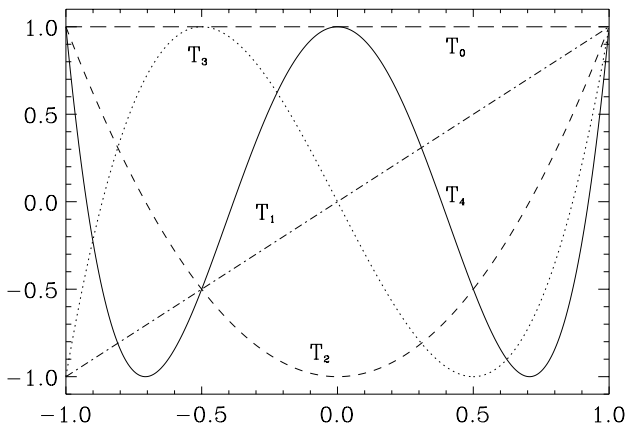

Figure B.1: *First four terms of a Chebyshev polynomial.*

Just like Fourier series, the Chebyshev polynomials satisfy a discrete orthogonality relation. Within the interval [-1,1], the polynomial $T_n(x)$ has n zeros and n+1 extrema including two boundary extrema at -1 and +1. At all the maxima $T_n(x) = 1$ and at all the minima, $T_n(x) = -1$.

B.2 Clenshaw's recurrence formula

The Clenshaw recurrence formula is an efficient way to evaluate a sum of coefficients c_k times functions F_k that obey a recurrence formula. For the Chebyshev polynomials, the recurrence formula of equation B.1 applies, for Fourier series the following recurrence formula applies:

$$\cos(k\theta) = 2\cos(\theta)\cos((k-1)\theta) - \cos((k-2)\theta) \quad \text{(B.2)}$$

$$\sin(k\theta) = 2\cos(\theta)\sin((k-1)\theta) - \sin((k-2)\theta) \quad \text{(B.3)}$$

Now consider the following series

$$f(\theta) = \sum_{k=0}^{N} c_k F_k(\theta) \quad \text{(B.4)}$$

Define the quantity y_k ($k = N...1$, backwards!) by the recurrence

$$y_{N+2} = y_{N+1} = 0$$

$$y_k = 2\cos(\theta)y_{k+1} - y_{k+2} + c_k \quad \text{(B.5)}$$

Then the evaluated function $f(\theta)$ for, respectively, cosine and sine series yield

$$f(\theta) = -y_2 + \cos(\theta)y_1 + c_0 \quad \text{(B.6)}$$

$$f(\theta) = \sin(\theta)y_1 \quad \text{(B.7)}$$

Using this recurrence, only one cosine function has to be calculated at each time step.

Appendix C

Properties of a DGBB 6202

The geometrical and material properties of a 6202 deep groove ball bearing, required for the calculations in Chapter 4 and 6, are listed in Table C.1. Frequently used properties for the lubricant are also mentioned. The listed properties are used unless it is mentioned otherwise.

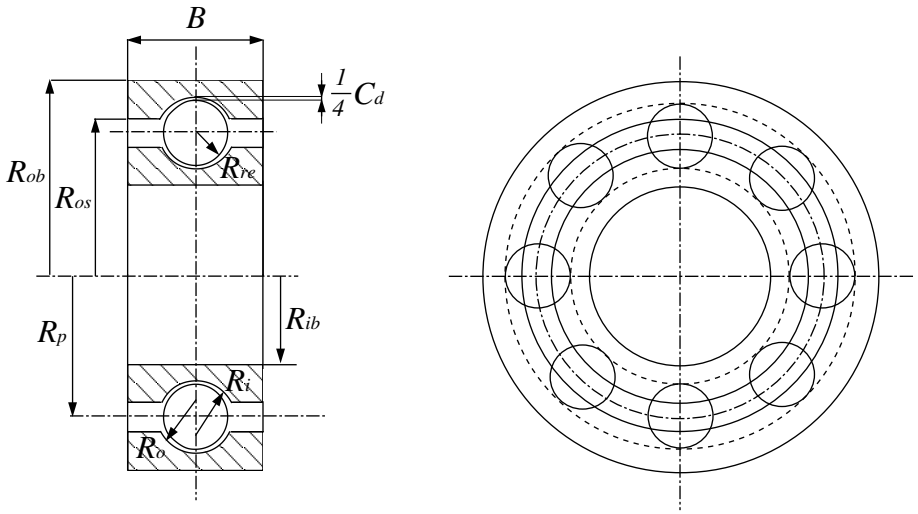

Figure C.1: *Geometrical properties of a deep groove ball bearing.*

ball bearing	
outer ring width:	$B = 11.0$ mm
outer bore radius:	$R_{ob} = 17.5$ mm
outer shoulder radius:	$R_{os} = 14.6$ mm
outer groove radius:	$R_o = 3.24$ mm
inner bore radius:	$R_{ib} = 7.5$ mm
inner groove radius:	$R_i = 3.07$ mm
number of rolling elements:	$Z = 8$
pitch radius:	$R_p = 15.63$ mm
radial clearance:	$C_d = 15$ mm
ball radius	$R_{re} = 3.0$ mm
modulus of elasticity:	$E = 2.06\text{e}11$ Pa
Poisson's ratio:	$\nu = 0.3$
density:	$\rho = 7800$ kg/m^3
lubricant	
nominal viscosity:	$\eta_0 = 0.1$ Pas
pressure-viscosity coefficient:	$\alpha_p = 1.0\text{e-}8$ Pa^{-1}
temperature-viscosity coefficient:	$\gamma = 0.028$ K^{-1}
thermal conductivity:	$k_f = 0.14$ Wm^{-1}K^{-1}

Table C.1: *Geometrical and material properties of a DGBB 6202.*

Because the outer ring is modelled as a flexible body some additional properties must be defined compared to the inner ring. These properties are needed for the modelling of the outer ring with finite elements.

Appendix D

Determination of the mutual approach

D.1 The inner contacts

The contact between a rolling element and the raceway of the inner ring is depicted in Figure D.1. For a geometrically perfect ball bearing, the mutual approach in the contact is defined by the change in distance between the centre of curvature of the raceway groove and the centre of the j^{th} rolling element, i.e.

$$\delta_j^{ic} = D_j^{ic} - D_0^{ic} \tag{D.1}$$

The parameter D_0^{ic} denotes the initial distance between the centres of curvature in the case $\delta_j^{ic} = 0$. It is defined by

$$D_0^{ic} = R_i - R_{re} \tag{D.2}$$

The geometrical properties R_i and R_{re} denote, respectively, the inner groove radius and the ball radius (see Figure C).

The instantaneous distance D_j^{ic} between the centre of curvature of the inner groove and the ball centre is given by

$$D_j^{ic} = \text{sign}(D_{rj}^{ic})\sqrt{(D_{rj}^{ic})^2 + (D_{zj}^{ic})^2} \tag{D.3}$$

where

$$D_{rj}^{ic} = R_{ig} + u_{rj}^{ig} - R_p - u_{rj}^{re} \tag{D.4}$$

$$D_{zj}^{ic} = u_{zj}^{ig} - u_{zj}^{re} \tag{D.5}$$

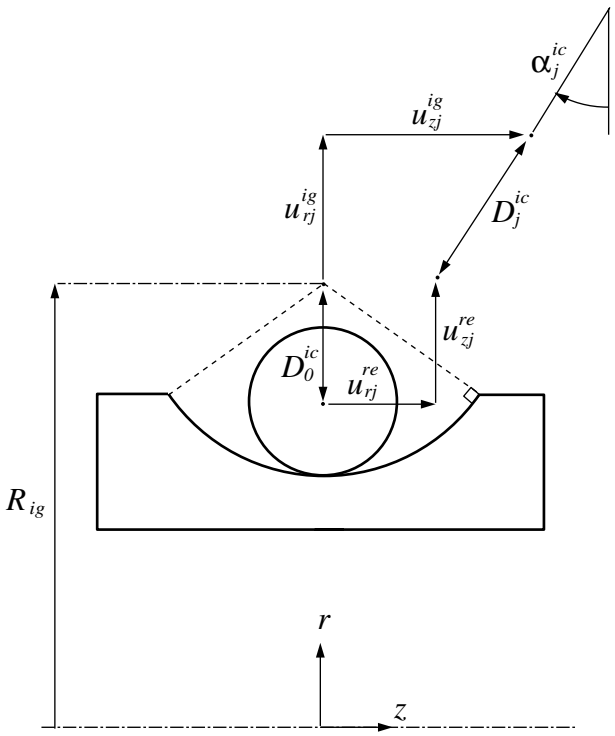

Figure D.1: *Contact between the raceway of the inner ring and the j^{th} rolling element.*

The parameter R_{ig} denotes the radius of the centre of curvature of the inner raceway groove. It can be derived from the main geometrical properties of the bearing presented in Appendix C (see also Figure C):

$$R_{ig} = R_p - R_{re} - \tfrac{1}{4}C_d + R_i \tag{D.6}$$

The displacements of the centre of curvature of the inner raceway can be expressed in terms of the inner ring DOF defined in Section 5.1.1. When it is assumed that the displacements and rotations of the inner ring are small, the following expressions apply:

$$u_{rj}^{ig} = u_x^{ir}\cos(\theta_j) + u_y^{ir}\sin(\theta_j) \tag{D.7}$$

$$u_{zj}^{ig} = u_z^{ir} + R_{ig}\left(\phi^{ir}\sin(\theta_j) - \psi^{ir}\cos(\theta_j)\right) \tag{D.8}$$

where θ_j denotes the circumferential position of the j^{th} rolling element (see

also Figure 5.7). The inner contact angles α_j^{ic} are defined by

$$\alpha_j^{ic} = \arctan\left(\frac{D_{zj}^{ic}}{D_{rj}^{ic}}\right) \tag{D.9}$$

The contact angle is bounded because of the finite width of the raceway. For most ball bearings it approximately follows that $-\frac{\pi}{3} < \alpha_j^{ic} < \frac{\pi}{3}$.

D.2 The outer contacts

In Figure D.2, the contact is depicted between the j^{th} rolling element and the flexible outer ring.

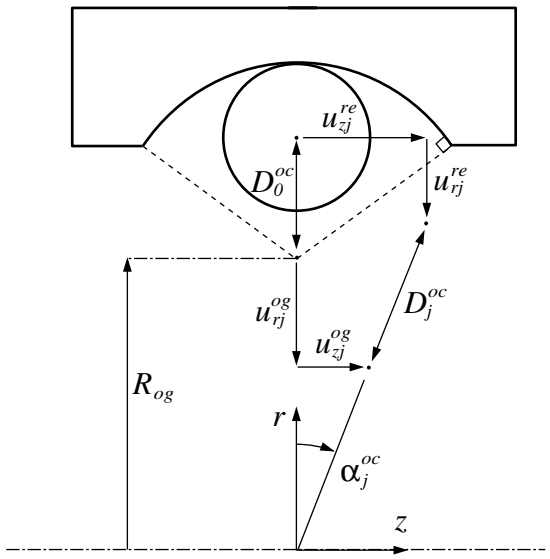

Figure D.2: *Contact between the raceway of the outer ring and the j^{th} rolling element.*

For the mutual approach between the centre of curvature of the outer raceway groove and the ball centre it follows:

$$\delta_j^{oc} = D_j^{oc} - D_0^{oc} \tag{D.10}$$

The initial mutual approach reads:

$$D_0^{oc} = R_o - R_b \tag{D.11}$$

The instantaneous mutual approach is given by:

$$D_j^{oc} = \text{sign}(D_{rj}^{oc})\sqrt{(D_{rj}^{oc})^2 + (D_{zj}^{oc})^2} \tag{D.12}$$

where

$$D_{rj}^{oc} = R_p + u_{rj}^{re} - R_{og} - u_{rj}^{og} \tag{D.13}$$
$$D_{zj}^{oc} = u_{zj}^{re} - u_{zj}^{og} \tag{D.14}$$

The definition for the outer contact is different compared to the definition for the inner contact. This is done to get an equal sign for the contact angle in both contacts. The parameter R_{og} denotes the radius of the centre of curvature of the outer raceway groove. The following relation applies (see also Figure C):

$$R_{og} = R_p + R_{re} + \tfrac{1}{4}C_d - R_o \tag{D.15}$$

The displacements of the raceway are described by the analytical series of equation 4.11 and 4.12. The series are evaluated in the centre of curvature of the outer raceway. It follows:

$$\begin{aligned} u_{rj}^{og} = &\sum_{n=0}^{N_r}\sum_{m=0}^{M_r}\sum_{l=0}^{L_r} a_r(t)\cos(n\theta_j)\cos(m\frac{\pi}{2})\cos(l\arccos(\frac{R_{og}}{R_{or}})) + \\ &+\sum_{n=1}^{N_r}\sum_{m=0}^{M_r}\sum_{l=0}^{L_r} b_r(t)\sin(n\theta_j)\cos(m\frac{\pi}{2})\cos(l\arccos(\frac{R_{og}}{R_{or}})) \end{aligned} \tag{D.16}$$

$$\begin{aligned} u_{zj}^{og} = &\sum_{n=0}^{N_z}\sum_{m=0}^{M_z}\sum_{l=0}^{L_z} a_z(t)\cos(n\theta_j)\cos(m\frac{\pi}{2})\cos(l\arccos(\frac{R_{og}}{R_{or}})) + \\ &+\sum_{n=1}^{N}\sum_{m=0}^{M_z}\sum_{l=0}^{L_z} b_z(t)\sin(n\theta_j)\cos(m\frac{\pi}{2})\cos(l\arccos(\frac{R_{og}}{R_{or}})) \end{aligned} \tag{D.17}$$

Finally, the outer contact angles read

$$\alpha_j^{oc} = \arctan\left(\frac{D_{zj}^{oc}}{D_{rj}^{oc}}\right) \tag{D.18}$$

As already mentioned, for most ball bearings it approximately follows that $-\frac{\pi}{3} < \alpha_j^{oc} < \frac{\pi}{3}$.

Appendix E

The partial derivatives

The partial derivatives of the mutual approach with respect to the generalised degrees of freedom of the unit consisting of the housing and the outer ring read:

$$\frac{\partial \delta_j^{oc}}{\partial \{a_r\}} = -\cos(\alpha_j^{oc})\cos(n\theta_j)\cos(m\tfrac{\pi}{2})\cos(l\arccos(\tfrac{R_{og}}{R_{or}})) \tag{E.1}$$

$$\frac{\partial \delta_j^{oc}}{\partial \{b_r\}} = -\cos(\alpha_j^{oc})\sin(n\theta_j)\cos(m\tfrac{\pi}{2})\cos(l\arccos(\tfrac{R_{og}}{R_{or}})) \tag{E.2}$$

$$\frac{\partial \delta_j^{oc}}{\partial \{a_z\}} = -\sin(\alpha_j^{oc})\cos(n\theta_j)\cos(m\tfrac{\pi}{2})\cos(l\arccos(\tfrac{R_{og}}{R_{or}})) \tag{E.3}$$

$$\frac{\partial \delta_j^{oc}}{\partial \{b_z\}} = -\sin(\alpha_j^{oc})\sin(n\theta_j)\cos(m\tfrac{\pi}{2})\cos(l\arccos(\tfrac{R_{og}}{R_{or}})) \tag{E.4}$$

$$\frac{\partial \tau_j^{oc}}{\partial \{a_r\}} = \sin(\alpha_j^{oc})\cos(n\theta_j)\cos(m\tfrac{\pi}{2})\cos(l\arccos(\tfrac{R_{og}}{R_{or}})) \tag{E.5}$$

$$\frac{\partial \tau_j^{oc}}{\partial \{b_r\}} = \sin(\alpha_j^{oc})\sin(n\theta_j)\cos(m\tfrac{\pi}{2})\cos(l\arccos(\tfrac{R_{og}}{R_{or}})) \tag{E.6}$$

$$\frac{\partial \tau_j^{oc}}{\partial \{a_z\}} = -\cos(\alpha_j^{oc})\cos(n\theta_j)\cos(m\tfrac{\pi}{2})\cos(l\arccos(\tfrac{R_{og}}{R_{or}})) \tag{E.7}$$

$$\frac{\partial \tau_j^{oc}}{\partial \{b_z\}} = -\cos(\alpha_j^{oc})\sin(n\theta_j)\cos(m\tfrac{\pi}{2})\cos(l\arccos(\tfrac{R_{og}}{R_{or}})) \tag{E.8}$$

The partial derivatives of the mutual approach with respect to the degrees of freedom of the rolling elements read:

$$\frac{\partial \delta_j^{oc}}{\partial u_{rj}^{re}} = \cos(\alpha_j^{oc}) \quad \frac{\partial \delta_j^{oc}}{\partial u_{zj}^{re}} = \sin(\alpha_j^{oc}) \tag{E.9}$$

$$\frac{\partial \delta_j^{ic}}{\partial u_{rj}^{re}} = -\cos(\alpha_j^{oc}) \quad \frac{\partial \delta_j^{ic}}{\partial u_{zj}^{re}} = -\sin(\alpha_j^{oc}) \tag{E.10}$$

$$\frac{\partial \tau_j^{oc}}{\partial u_{rj}^{re}} = -\sin(\alpha_j^{oc}) \quad \frac{\partial \tau_j^{oc}}{\partial u_{zj}^{re}} = \cos(\alpha_j^{oc}) \tag{E.11}$$

$$\frac{\partial \tau_j^{ic}}{\partial u_{rj}^{re}} = \sin(\alpha_j^{oc}) \quad \frac{\partial \tau_j^{ic}}{\partial u_{zj}^{re}} = -\cos(\alpha_j^{oc}) \tag{E.12}$$

The partial derivatives of the mutual approach with respect to the generalised degrees of freedom of the shaft read:

$$\frac{\partial \delta_j^{ic}}{\partial p_x} = \cos(\alpha_j^{ic})\cos(\theta_j) \tag{E.13}$$

$$\frac{\partial \delta_j^{ic}}{\partial p_y} = \cos(\alpha_j^{ic})\sin(\theta_j) \tag{E.14}$$

$$\frac{\partial \delta_j^{ic}}{\partial p_z} = \sin(\alpha_j^{ic}) \tag{E.15}$$

$$\frac{\partial \delta_j^{ic}}{\partial p_\phi} = R_{ig}\sin(\alpha_j^{ic})\sin(\theta_j) \tag{E.16}$$

$$\frac{\partial \delta_j^{ic}}{\partial p_\psi} = -R_{ig}\sin(\alpha_j^{ic})\cos(\theta_j) \tag{E.17}$$

$$\frac{\partial \tau_j^{ic}}{\partial p_x} = -\sin(\alpha_j^{ic})\cos(\theta_j) \tag{E.18}$$

$$\frac{\partial \tau_j^{ic}}{\partial p_y} = -\sin(\alpha_j^{ic})\sin(\theta_j) \tag{E.19}$$

$$\frac{\partial \tau_j^{ic}}{\partial p_z} = \cos(\alpha_j^{ic}) \tag{E.20}$$

$$\frac{\partial \tau_j^{ic}}{\partial p_\phi} = R_{ig}\cos(\alpha_j^{ic})\sin(\theta_j) \tag{E.21}$$

$$\frac{\partial \tau_j^{ic}}{\partial p_\psi} = -R_{ig}\cos(\alpha_j^{ic})\cos(\theta_j) \tag{E.22}$$

Because the partial derivatives can be calculated analytically, the the non-linear equations converge relatively fast.

Appendix F

Newmark time integration

The nonlinear equations of motion are integrated with the Newmark method (see Bathe, 1982). The method is based on a constant-average acceleration scheme and is also referred to as the trapezoidal rule. The following assumptions are employed:

$$\{p\}^{t+\Delta t} = \{p\}^t + \tfrac{\Delta t}{2}\left(\{\dot{p}\}^t + \{\dot{p}\}^{t+\Delta t}\right) \tag{F.1}$$

$$\{\dot{p}\}^{t+\Delta t} = \{\dot{p}\}^t + \tfrac{\Delta t}{2}\left(\{\ddot{p}\}^t + \{\ddot{p}\}^{t+\Delta t}\right) \tag{F.2}$$

The constant-average-acceleration method is unconditionally stable for linear problems. For most nonlinear problems in structural dynamics this also applies. An accuracy analysis shows that the method does not suffer from amplitude decay. With respect to the choice of the time step Δt one must be aware that the method may suffer from period elongation. When the characteristic time period of the solution is denoted by T then a time step $\Delta t = T/20$ is sufficient to keep the error below 1%.

Nonlinear dynamic analysis requires also an iterative procedure. Due to the effect of inertia the response of the system is generally smooth. As a result only a few iterations are sufficient to satisfy the convergence criteria. Convergence is always achieved, provided the time step Δt is small enough. Due to the fact that in a nonlinear analysis the response is highly path-dependent, the allowed convergence error must be very small. In the present study, use is made of the modified Newton-Raphson iteration, for which the following equations are valid:

$$[m]\{\ddot{p}\}_k^{t+\Delta t} + [\tilde{c}]^t\{\Delta\dot{p}\}_k + [\tilde{k}]^t\{\Delta p\}_k = \{R\}^{t+\Delta t} - \{F\}_{k-1}^{t+\Delta t} \tag{F.3}$$

$$\{p\}_k^{t+\Delta t} = \{p\}_{k-1}^{t+\Delta t} + \{\Delta p\}_k \tag{F.4}$$

$$\{\dot{p}\}_k^{t+\Delta t} = \{\dot{p}\}_{k-1}^{t+\Delta t} + \{\Delta\dot{p}\}_k \tag{F.5}$$

The vector $\{R\}$ denotes the externally applied forces and the vector $\{\mathrm{F}\}$ denotes the nonlinear contact forces, which are a function of both $\{p\}$ and $\{\dot{p}\}$. The stiffness matrix $[\tilde{k}]^t$ and the damping matrix $[\tilde{c}]^t$ are used as appraisers, which are defined as:

$$[\tilde{k}]^t = \frac{\partial\{F^t\}}{\partial\{p\}} \qquad [\tilde{c}]^t = \frac{\partial\{F^t\}}{\partial\{\dot{p}\}} \tag{F.6}$$

Both matrices can be calculated analytically from the expressions for the contact forces in the equations of motion. The contributions of the restoring forces if the inner and outer contacts to the approximated stiffness matrix read

$$\begin{aligned}[\tilde{k}]^t = &\frac{\partial F_i^e}{\partial \delta_i^{oc}} \frac{\partial \delta_i^{oc}}{\partial\{p\}} \frac{\partial \delta_i^{oc}}{\partial\{p\}^T} + F_i^e \frac{\partial^2 \delta_i^{oc}}{\partial\{p\}\partial\{p\}} + \\ &+ \frac{\partial F_i^e}{\partial \delta_i^{ic}} \frac{\partial \delta_i^{ic}}{\partial\{p\}} \frac{\partial \delta_i^{ic}}{\partial\{p\}^T} + F_i^e \frac{\partial^2 \delta_i^{ic}}{\partial\{p\}\partial\{p\}}\end{aligned} \tag{F.7}$$

Due to the geometrically nonlinear nature of the contact problem in ball bearings, the second order derivatives in equation F.7 do not vanish. In fact, they provide the tangential stiffness in the contact.

The contributions of the dissipative contact forces to the approximated damping matrix yield:

$$\begin{aligned}[\tilde{c}]^t = &c^{oc} \frac{\partial \delta_i^{oc}}{\partial\{p\}} \frac{\partial \delta_i^{oc}}{\partial\{p\}^T} + \mu c^{oc} \frac{\partial \tau_i^{oc}}{\partial\{p\}} \frac{\partial \tau_i^{oc}}{\partial\{p\}^T} + \\ &+ c^{ic} \frac{\partial \delta_i^{ic}}{\partial\{p\}} \frac{\partial \delta_i^{ic}}{\partial\{p\}^T} + \mu c^{ic} \frac{\partial \tau_i^{ic}}{\partial\{p\}} \frac{\partial \tau_i^{ic}}{\partial\{p\}^T}\end{aligned} \tag{F.8}$$

As already mentioned in Section 5.2, the dissipative forces also contribute to the approximated stiffness matrix because the time rate of change of the mutual approach is not only a function of $\{\dot{p}\}$, but also of $\{p\}$. The contribution leads to skew-symmetric terms. Since the stiffness matrix is merely used as an appraiser these terms can be omitted in order to maintain symmetric system matrices which is favourable from a computational point of view.

After substitution of equation F.1 in equation F.3, a linear set of equations is obtained:

$$[\hat{k}]\{\Delta p\}_k = \{\hat{R}\}_{k-1} \tag{F.9}$$

with

$$[\hat{k}] = [\tilde{k}] + \frac{2}{\Delta t}[\tilde{c}] + \frac{4}{\Delta t^2}[m] \tag{F.10}$$

and where $\{\hat{R}\}$ is the residual of the dynamic force balance from the previous iteration. To solve $\{\Delta p\}_k$, the full matrix $[\hat{k}]$ must be decomposed. Both the evaluation of $[\tilde{k}]$ and $[\tilde{c}]$ and the decomposition of the matrix $[\hat{k}]$ are very time consuming operations. Hence, the calculation of $[\hat{k}]$ must be avoided as much as possible. Usually the same appraisers can be used for several time steps, which considerably improves the efficiency of the computations.

Bibliography

Aini, R., Rahnejat, R., and Gohar, R. (1990). A five degree of freedom analysis of vibrations in precision spindles. *Int. J. Mach. Tools Manufact.*, 30(1):1–18.

Barus, H. (1973). Inlet shear heating in elastohydrodynamic lubrication. *ASME Journal of Lubrication Technology*, 95(4):417–426.

Bathe, K. J. (1982). *Finite element procedures in engineering analysis.* Prentice-Hall, New Jersey.

Bos, C. H. (1995). *Frictional heating of tribological contacts.* PhD thesis, University of Twente, the Netherlands, ISBN 90-9008920-9.

Childs, D. (1993). *Turbomachinery rotordynamics, phenomena, modelling and analysis.* Wiley & Sons, New York.

Craig, R. R. (1981). *An introduction to computer methods.* John Wiley & Sons Inc, New York.

Craig, R. R. and Bampton, M. C. C. (1968). Coupling of substructures for dynamic analysis. *AIAA Journal*, 6(7):1313–1319.

Craig, R. R. and Chang, C. J. (1976). A review of substructuring coupling methods for dynamic analysis. *13th annual meeting*, 6(7):1313–1319.

Dietl, P. (1997). *Damping and stiffness characteristics of rolling element bearings.* PhD thesis, Technical University of Vienna, Austria.

Glasgow, D. A. and Nelson, H. D. (1980). Stability analysis of rotor-bearing systems using component mode synthesis. *Trans. of the ASME, Journal of Mechanical Design*, 102:352–359.

Greenwood, J. A. and Kauzlarich, J. J. (1973). Inlet shear heating in elastohydrodynamic lubrication. *ASME Journal of Lubrication Technology*, 95(4):417–426.

Gupta, P. K. (1979). Dynamics of rolling element bearings part III: Ball bearing analysis & part IV: Ball bearing results. *ASME Journal of Lubrication Technology*, 101:312–326.

Hamrock, B. J. and Dowson, D. (1977). Isothermal elastohydrodynamic lubrication of point contact - part iii. *ASME Journal of Lubrication Technology*, 99(2):264–276.

Harris, T. (1993). *Rolling bearing analysis*. Wiley & Sons, New York.

Hendrikx, R. T. W. M., Nijen, G. C. v., and Dietl, P. (1998). Vibrations in household appliances with rolling element bearings. *Proc. ISMA23 Noise and Vibration Engineering*, 3:1537–1544.

Hertz, H. (1881). Über die Berührung fester elastischen Körper. *Journal für die reine und angewandte Mathematik*, 92:156–171.

Hinz, R. M. (1975). Analytical methods in component modal synthesis. *AIAA Journal*, 13(8):1007–1016.

Hou, S. (1969). Review of modal analysis and a new approach. *Shock and Vibration Bulletin*, 40(4):25–39.

Hurty, W. C. (1965). Dynamic analysis of structural systems using component modes. *AIAA Journal*, 3(4):678–685.

Kraker, H. d. (1992). *Numeriek-experimentele analyse van dynamische systemen*. University of Technology, Eindhoven.

Lim, T. C. and Singh, R. (1990). Vibration transmission through rolling element bearings, part I: Bearing stiffness formulation. *Journal of Sound and Vibration*, 139(2):179–199.

Lubrecht, A. A. (1987). *The numerical solution of the elastohydrodynamically lubricated line- and point contact problem using multigrid techniques*. PhD thesis, University of Twente, the Netherlands, ISBN 90-9001583-3.

MacNeal, R. H. (1971). A hybrid method of component mode synthesis. *Computers & Structures*, 1(4):581–601.

Meeks, C. R. and Tran, L. (1996). Ball bearing dynamic analysis using computer methods-part I: Analysis. *ASME Journal of Trobology*, 118:52–58.

Meldau, E. (1951). Die Bewechung der Achse von Wälzlagern bei geringen Drehzahlen. *Werkstatt und Betrieb*, 84(C5):308–313.

Mevel, B. and Guyader, J. L. (1993). Routes to chaos in ball bearings. *Journal of Sound and Vibration*, 162(3):471–487.

Meyer, L. D., Ahlgren, F. F., and Weichbrodt, B. (1980). An analytical model for ball bearing vibrations to predict vibration response due to distributed defects. *Journal of Mechanical Design*, 102:205–210.

Moes, H. (1992). Optimum similarity analysis with application to elastohydrodynamic lubrication. *Wear*, 159:57–66.

Mul, J. M. d., Vree, J. M., and Maas, D. A. (1989a). Equilibrium and associated load distribution in ball and roller bearings loaded in five degrees of freedom while neglecting friction- part I: General theory and application to ball bearings. *Journal of Tribology*, 111:142–148.

Mul, J. M. d., Vree, J. M., and Maas, D. A. (1989b). Equilibrium and associated load distribution in ball and roller bearings loaded in five degrees of freedom while neglecting friction- part II: Application to roller bearings and experimental verification. *Journal of Tribology*, 111:149–155.

Nayfeh, A. H. and Mook, D. T. (1979). *Nonlinear oscillations*. John Wiley & Sons Inc, New York.

Nielsen, J. C. O. and Igeland, A. (1995). Vertical dynamic interaction between train and track-influence of wheel and track imperfections. *Journal of Sound and Vibration*, 187(5):825–839.

Nijen, G. C. v. and Wensing, J. A. (1998). On the dynamic behaviour of a single shaft supported by rolling element bearings. *VDI-Fachtagung Gleit- und Wälzlagerungen: Gestaltung, Berechnung, Einsatz, Veithöchheim, Germany*.

Perret, H. (1950). Elastischen Spielschwingungen konstant belaster Wälzlager. *Werkstatt und Betrieb*, 83(C5):354–358.

Reusner, H. (1977). *Druckflachenbelastung und Oberflachenverschiebung im Walzkontakt von Rotationskorpern*. PhD thesis, University of Karlsruhe, Germany.

Rieker, J. R., Lin, Y. H., and Trethewey, M. W. (1996). Discretization considerations in moving load finite element beam models. *Finite Elements in Analysis and Design*, 21:129–144.

Rothschild, V. and Logothetis, N. (1986). *Probability distributions*. Wiley & Sons, New York.

Rubin, S. (1975). Improved component-mode representation for structural dynamic analysis. *AIAA Journal*, 13(8):995–1006.

SKF, editor (1992). *SKF General Catalogue*. Carl Gerber GmbH, Germany.

Su, Y. T., Lin, M. H., and Lee, M. S. (1993). The effects of surface irregularities on roller bearing vibrations. *Journal of Sound and Vibration*, 165(3):455–466.

Sunnersjo, C. S. (1978). Varying compliance vibrations of rolling bearings. *Journal of Sound and Vibration*, 58(3):363–373.

Tallian, T. and Gustafsson, O. (1958). The mechanics of rolling element vibration. *ASME paper*, 58-A-292.

Tijdeman, H. (1990). *Voortgezette dynamica - mechanische trillingen, inleiding modaal analyse en experimenteel trillingsonderzoek*. University of Twente.

Timoshenko, G. (1955). *Strength of materials, Part I*. Van Nostrand, Princeton, New York, third edition.

Timoshenko, G. (1993). *Theory of elasticity*. Wiley & Sons, New York.

Venner, C. H. (1991). *Multilevel solution of the EHL line and point contact*. PhD thesis, University of Twente, the Netherlands, ISBN 90-9003974-0.

Walford, T. L. H. and Stone, B. J. (1983). The sources of damping in rolling element bearings under oscillating conditions. *Proc. Inst. Mech. Eng.*

Wang, Z. W. (1981). Accuracy of constraint mode methods in component mode synthesis. Master's thesis, Institute of Sound and Vibration Research, Southampton.

Wardle, F. P. (1988). Vibration forces produced by waviness of the rolling surfaces of thrust loaded ball bearings, part 1: Theory. *Proc. Inst. Mech. Eng.*, 202(C5):305–312.

Wensing, J. A. (1998). Dynamic behaviour of ball bearings on vibration test spindles. 16^{th} *International Modal Analysis Conference, Santa Barbara, USA*.

Wensing, J. A. and Nijen, G. C. v. (1996). 2d computational model for vibration analysis of waviness in rolling bearing applications. *Inst. Mech. Eng.,* 6^{th} *int. Conference on Vibrations in Rotating Machinery*, pages 371–382.

Wijnant, Y. H. (1998). *Contact dynamics in the field of elastohydrodynamic lubrication*. PhD thesis, University of Twente, the Netherlands, ISBN 90-36512239.

Yhland, E. (1992). A linear theory of vibrations caused by ball bearings with form errors operating at moderate speed. *ASME Journal of Tribology*, 114:348–359.